Muh Fadhil Albab

# Development of $C_{60}$ Transport Layer and Optical Analysis of Perovskite Absorber Material

## For Semi-transparent Perovskite Solar Cells Applications

TU Delft

# Development of $C_{60}$ Transport Layer and Optical Analysis of Perovskite Absorber Material

For Semi-transparent Perovskite Solar Cells Application

By

Muh Fadhil Albab B

in partial fulfillment of the requirements for the degree of

**Master of Science**
in Materials Science and Engineering

at the Delft University of Technology,
to be defended publicly on Monday, November 22, 2021

Student number: 5001781
Project duration: November 17, 2020 – November 22, 2021
Supervisors: Dr. Amarante Bottger
Dr. Luana Mazzarella
Prof. dr. Olindo Isabella
Dr. Tom Savenije

**Graduate**

Muh Fadhil Albab B

MSc Materials Science and Engineering (MSE)

Specialization in Materials for Sustainable Development

Faculty of Mechanical, Maritime and Materials (3ME), TU Delft

*Fadhil.albab@gmail.com*

**MSc Thesis Committee**

Dr. Amarante Bottger – Department of Materials Science and Engineering, TU Delft

Dr. Luana Mazzarella – PVMD, Department of Electrical Sustainable Energy, TU Delft

Prof. dr. Olindo Isabella – PVMD, Department of Electrical Sustainable Energy, TU Delft

Dr. Tom Savenije – Department of Chemical Engineering, TU Delft

**Delft University of Technology**

Department of Electrical Sustainable Energy – Photovoltaics Materials and Devices (PVMD)

# Abstract

Perovskite materials gain a huge interest in the photovoltaic (PV) community due to its unique characteristics, including long carrier diffusion length, widely tunable bandgap, light absorption potential, and low processing cost. Nowadays, most perovskite fabrication methods employ a solution-based process due to its simplicity and production speed. However, this deposition method provides a non-uniform structure and uses highly toxic solvents, posing the risk of contamination and adverse effects on the environment. On the other hand, a solvent-free method like thermal evaporation can produce a uniform and conformal layer. This method can be used to produce not only the perovskite absorber layer but also the contact layers and transport layers. Depending on the deposition parameters, the resulting morphological properties also change. Therefore, it becomes interesting to understand the detailed knowledge of the film growth and the effects of the deposition parameters on the exact kinetics and the optical properties. Hence, the first objective of this study focuses on developing $C_{60}$ electron transport layers (ETL) for application in all-evaporated perovskite solar cells (PSCs). The $C_{60}$ thin film was deposited with different thicknesses of 20, 30, 40 nm and deposition rates 0.3, 0.5, and 1 Å/s on top of the silicon wafer substrate. The resulting surface morphology is obtained from scanning electron microscopy (SEM) and atomic force microscopy (AFM). It indicates that $C_{60}$ with 40 nm thickness and 0.3 Å/s deposition rate shows a pinhole-free layer with an average surface roughness of 1.05 nm and thickness uniformity of more than 94%. The X-ray diffraction (XRD) measurement shows that decrease of peak intensity as the thickness is reduced from 40 to 20 nm. Moreover, with different deposition rates, 1 Å/s of deposition rate exhibits an asymmetric broadening peak which attributes to the small grain size and the presence of a planar defect in the structure of $C_{60}$.

The optical analysis has also been performed to get the complex refractive index $C_{60}$ and identify the effect of deposition rates and layer thicknesses on optical constants. A procedure to extract optical constant for the perovskite absorber layer has been developed during this thesis project using a combination approach of b-spline and Tauc-Lorentz dispersion model. The obtained results were found to be in excellent agreement with experimental work and literature data.

Furthermore, the complete solar cells with p-i-n configuration and semi-transparent perovskite solar cells (ST-PSCs) were optically simulated using GenPro4 software. This simulation aims to identify both the photocurrent density of the perovskite absorber layer and the optical losses caused by parasitic absorption in the supporting layers. In the p-i-n structure, ITO and $MoO_x$ layer located on the illuminated side contribute to the main portion of optical loss. Simulations suggest that 40-nm-thick ITO and 10-nm-thick MoOx is an ideal layer stack to deliver high implied photocurrent (22.14 $mA/cm^2$). On the other hand, the optical loss in semi-transparent perovskite solar cells is investigated in two different wavelength regions (i) 300 – 800 nm and (ii) 800 – 1200 nm. In this investigation, the metal back contact is replaced with ITO and cells illuminated from the ETL side. The results show that, in the first wavelength range, the main optical losses are due to reflection, parasitic absorption in the $C_{60}$ and top ITO layer. These losses are reduced by applying 120-nm-thick anti-reflective coating $MgF_2$ and decreasing the thickness of $C_{60}$ to 10 nm. Moreover, in the wavelength region of 800 – 1200 nm, the optical losses are mainly affected by the top and bottom ITO, $MoO_x$ layer, and reflected light. After optimizing top ITO and $MgF_2$ thickness to 50 and 120 nm, respectively, a 17.07 $mA/cm^2$ of photocurrent transmitted through the cells can be achieved. The light transmittance is ~88%, indicating the potential of semi-transparent perovskite solar cells to be applied in perovskite/silicon tandem devices.

Keywords: $C_{60}$; Perovskite; Thermal evaporation; Thin-film; Transport layer.

# Contents

# List of Figures

# List of Tables

# Nomenclature

| *Nomenclature* | *Definition* | *Unit* |
|---|---|---|
| α | Absorption coefficient | [-] |
| A | Absorbance | [-] |
| AFM | Atomic force microscopy | [-] |
| AM | Air mass | [-] |
| BCP | Bathocuproine | [-] |
| $C_{60}$ | Buckminsterfullerene | [-] |
| CL | Classical oscillator | [-] |
| DMF | Dimethylformamide | [-] |
| $E_B$ | Binding energy | [meV] |
| $E_f$ | Electric field | [V/m] |
| $E_g$ | Bandgap | [eV] |
| EMA | Effective medium approximation (model) | [-] |
| ETL | Electron Transport Layer | [-] |
| FA | Formamidinium | [-] |
| FB | Fouruhi and Bloomer | [-] |
| FCC | Face center cubic | [-] |
| FF | Fill factor | [%] |
| FTO | Fluorine-doped tin oxide | [-] |
| HOMO | Highest Occupied Molecular Orbital | [-] |
| HTL | Hole Transport Layer | [-] |
| $l_D$ | Diffusion length | [nm] |
| ITO | Indium tin oxide | [-] |
| $J_{ph}$ | Implied photocurrent density | [mA/cm$^2$] |
| $J_{sc}$ | Short circuit current density | [mA/cm$^2$] |
| $J_T$ | Transmittance current density | [mA/cm$^2$] |
| k | Extinction coefficient/attenuation coefficient | [-] |
| KK | Kramers-Kronig | [-] |
| t | Thickness | [nm] |
| LUMO | Lowest Unoccupied Molecular Orbital | [-] |
| $MAPbI_3$ | Methylammonium lead iodide | [-] |
| MoOx | Molybdenum oxide | [-] |
| MSE | Mean squared error | [-] |
| n | Refractive index | [-] |
| NIR | Near infra-red | [-] |
| PCBM | Phenyl-$C_{61}$-butyric acid methyl ester | [-] |
| PCE | Power Conversion Efficiency | [%] |
| PSCs | Perovskite Solar Cells | [-] |
| QCM | Quartz crystal microbalance | [-] |
| R | Reflectance | [-] |
| RMS | Root mean squared | [nm] |
| SE | Spectroscopic Ellipsometry | [-] |
| SEM | Scanning electron microscopy | [-] |
| SRH | Shockley-Read-Hall recombination | [-] |
| STDEV | Standard deviation | [-] |

| *Nomenclature* | *Definition* | *Unit* |
|---|---|---|
| ST-PSCs | Semi-transparent perovskite solar cells | [-] |
| T | Transmittance | [%] |
| TL | Tauc-Lorentz | [-] |
| UV-Vis | Ultraviolet-visible | [-] |
| $V_{oc}$ | Open circuit voltage | [V] |
| XRD | X-ray diffraction | [-] |
| σ | Uniformity | [%] |
| ψ | p- and s-polarized light amplitude ratio | [-] |
| Δ | p- and s-polarized light phase difference | [-] |
| τ | Goldschmidt tolerance factor | [-] |
| λ | Wavelength | [nm] |

# 1 Introduction

*'We are like tenant farmers chopping down the fence around our house for fuel when we should be using nature's inexhaustible sources of energy – sun, wind, and tide. I'd put my money on the sun and solar energy. What a source of power! I hope we don't have to wait until oil and coal run out before we tackle that.'*

*-Thomas Edison*

## 1.1 Solar energy

One of the significant issues humankind is confronting nowadays is the growing demand for energy. Although the worldwide energy consumption is estimated at approximately 16 TW-yr annually [1], it is expected to follow an upward trend in the coming years due to the increase of the global population and industrialization of developing countries. According to International Energy Agency (IEA), in their report in 2019 stated that global energy demand rises by 1% per year to 2040 [2].

Up to now, the majority of humanity's energy needs are covered by fossils fuel. However, this energy source has been linked to a soaring concentration of greenhouse gasses. In 2019, the growth in total global greenhouse gas emissions at a rate of 1.1% reached 52.4 gigatonnes of equivalent ($GtCO_2$ eq) [3]. As a consequence of devastating environmental effects on the planet, a legally binding international treaty on climate change has been signed by 196 countries in the Paris Climate Agreement of 2015 to reduce the amounts of carbon dioxide released into the atmosphere. In this agreement, countries are urged to replace conventional energy generation methods with renewable sources with the goal of limiting global warming to well below 2, preferably to 1.5 degrees Celcius, compared to the pre-industrial level [4].

Solar energy could contribute to providing the answer to globally increasing energy demand in an environmentally and friendly way. The total solar energy potential is 23.000 TW-yr, and it is orders of magnitude higher than the potential of any renewable energy source and/or the world energy consumption of 16 TW-yr [1]. As reported by The Renewables 2019 Global Status Report (GSR 2019), the capacity addition of power generation in the next 20 years will be dominated by solar cells [5]. These technologies have the potential to supply electricity against very low or zero greenhouse gas emissions. However, the question remains if the technology of the solar cell can be efficient, cost-effective, and reliable enough to meet these expectations.

## 1.2 Solar cells: current status

Solar cells development has been widely studied over the past few years. There are a few aspects of consideration in developing materials for solar cells, e.g., power conversion efficiency (PCE), stability, scalability, the availability of raw materials, and processing cost.

As shown in Figure 1.1, there are mainly three categories of solar cell materials which are at a different level of development that has been reported so far; a) Si-based solar cells, b) non-silicon solar cells, and c) thin-film solar cells. Among all the photovoltaics (PV) technologies, currently, Si-based panels (mono and poly-crystalline) hold 95% share of the worldwide photovoltaics materials production [6]. Another Si-based with advanced solar architecture was introduced as PERC (Passivated Emitter and Rear Cell). This provides a back-surface passivation layer, reduces electron recombination, increases absorption of light, provides higher internal reflectivity, and increases 0.8 to 1% efficiency of PV panels. The abundant source of Si raw materials and device stability have assured its place as the most widely used solar cells materials. However, manufacturing crystalline silicon is highly energy consuming and extremely requires precise processing control. Moreover, due to silicon's indirect bandgap, thick crystalline silicon layers are needed to sufficiently absorb the appropriate range of the solar spectrum. The panels also require thick, expensive glass supports that limit their areas of application.

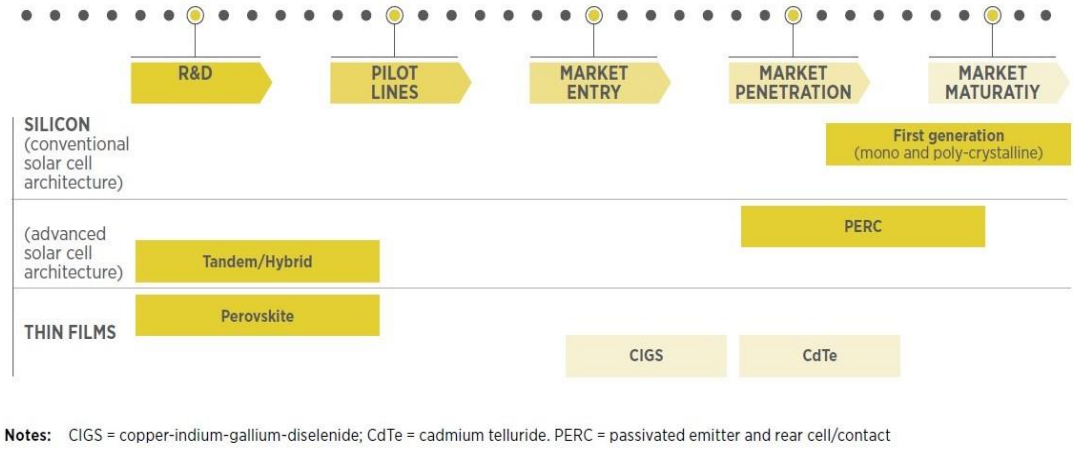


*Figure 1.1 Photovoltaics status of development [6]*

The tandem solar cells are stacks of individual cells that selectively absorb a specific band of light into electrical energy, leaving the remaining photon to be absorbed and converted to electricity in the cell below [6]. The world record efficiency for these tandem solar cells is shown by GaInP/InGaAs/InGaAs, which can achieve 47.1% solar conversion efficiency [7] operated under the direct spectrum at 143 suns concentration. When tuned to the global spectrum, this structure generates a 1-Sun global efficiency of 39.2% [8]. However, since it uses costly materials and a high price of fabrication cost, these tandem/hybrid stacks still cannot penetrate through the market level, particularly for households and large-scale applications. The main application of this type of solar cell is space use and concentrator photovoltaic [9]. Perovskite/Si tandem solar cells also have been proposed as a promising candidate to overcome the theoretical efficiency limit of Si-based solar cells in a single-junction configuration, which is 29.4% [10]. Their optical characteristic allows both subcells to achieve current matching through bandgap optimization [11]. The contribution of perovskite can enhance the absorption of the low wavelength range of the solar spectrum. Theoretical efficiency for this tandem configuration has been reported to be 45.1% [12].

Thin-film technologies (often referred to as second-generation PV) are composed of micron-thick photon-absorbing layers. The CIGS (Copper Indium Gallium Selenide) and cadmium telluride (CdTe) are the most well-known thin-film solar cells that have already entered the

market level. Those materials provide an efficiency level of up to 22.1% [7]. The CdTe can be produced at low temperatures; therefore, the processing becomes flexible and affordable. However, the fabrication is difficult due to indium's scarcity, complex stoichiometry, and multiple phases to produce them. Not to mention, gallium and cadmium are toxic and require special handling and disposal [6]. The expensive manufacturing process and costly raw materials are urging more researchers to develop a new solar cells material that combines high efficiency, high stability, use of abundant materials, and low processing cost.

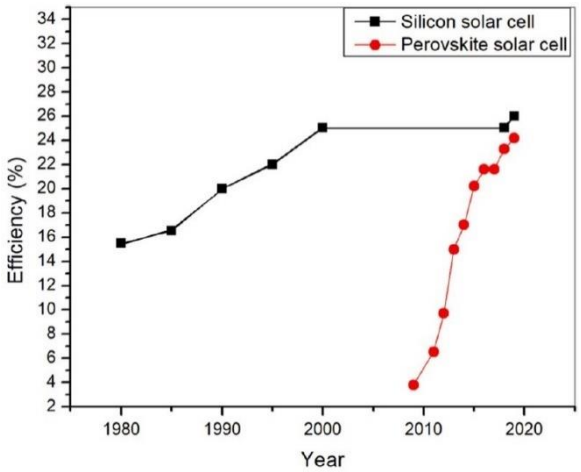


*Figure 1.2 Recorded power conversion efficiency (PCE) of the perovskite solar cells vs silicon solar cell in the progressive years [13]*

On the other hand, perovskite solar cell (PSC) is gaining huge interest among the PV community. The first perovskites solar cell was reported by Kojima et al. in 2009 with only a 3.8% conversion rate [14]. Figure 1.2 depicts the development of PSCs in a decade compared to silicon solar cells. Since perovskite structure is easily processed and manufactured, perovskite solar cell's improvement is remarkably increasing. Recently, the highest efficiency of single-junction PSCs has reached 25.5% reported by UNIST (South Korea) [7]. The development of perovskites material is widely accepted due to its unique properties. e.g., ambipolar charge transport behavior, high absorption coefficient (greater than $10^5$ $cm^{-1}$), high carrier diffusion length (100nm to 1μm), low exciton binding energy (less than 5 meV) [15], [16], tunable band-gap, low surface recombination velocity, and amiable grain boundary effect [15]. However, the complete replacement of the Si solar cells from the market cannot be done as silicon solar cells' lifetime is as high as 25-30 years. The major obstacle in the way of commercialization of perovskite solar cells is easy degradation (stability issue) [17], [18]. Thus, it requires more advanced research before it goes to market maturity.

While most of the current PSCs fabrication processes utilize solution-based methods due to its simplicity and low-cost processing, this technique has some drawbacks, especially concerning film quality and scalability. Also, the environmental impact of solvents required for a solution-based process cannot be overlooked. The limited solubility of lead halides in most solvents resulted in the almost ubiquitous use of highly toxic solvents. Therefore, another possible deposition method is vacuum based such as thermal evaporation has been demonstrated. Although this process requires an expensive vacuum setup and a relatively slow process, this production method provides an alternative way to produce a uniform structure, solvent-free, conformal, and large area of perovskite films.

## 1.3 Perovskite solar cells: planar architecture

A perovskite Solar Cells (PSCs) is typically made up of a perovskite absorber layer sandwiched between the hole transport layer (HTL) and an electron transport layer (ETL). When the perovskite absorber layer absorbs light, it will increase the free electron and holes concentration. Thus, these free charges diffuse through the transport layer, where electrons move towards ETL and holes towards HTL. It was found that metal halide perovskite (MHP) owns long charge carrier diffusion lengths and has ambipolar behavior, indicating that the materials can transport both electrons and holes between the cell terminals [19]. All of these promising results have indicated that two possibilities of the planar structure are feasible. Figure 1.3 shows two different planar device architectures where the light is coming from the bottom side. In planar device structure, the diffusion length of the charge carriers is greater than the thickness of the perovskite absorber layer [20].

The first inverted planar p-i-n structure adopted a similar structure as in the organic solar cells [15], [21], [22]. The structure is referred to as inverted planar because the planar p-i-n has an opposite order of HTL and ETL than the regular n-i-p structure (shown in Figure 1.3b). Compared to the planar n-i-p structure (Figure 1.3a), the inverted planar p-i-n shows the potential to eliminate hysteresis during current-voltage *(i-V)* sweep experiments [22], [23]. In addition, the inverted configuration has the great advantage of electron-selective contacts that can be fabricated much thinner compared to commonly used HTL (Spiro-OMeTAD) in p-i-n structure, resulting in less parasitic absorption, higher transparency, and hence higher photocurrent density [11].

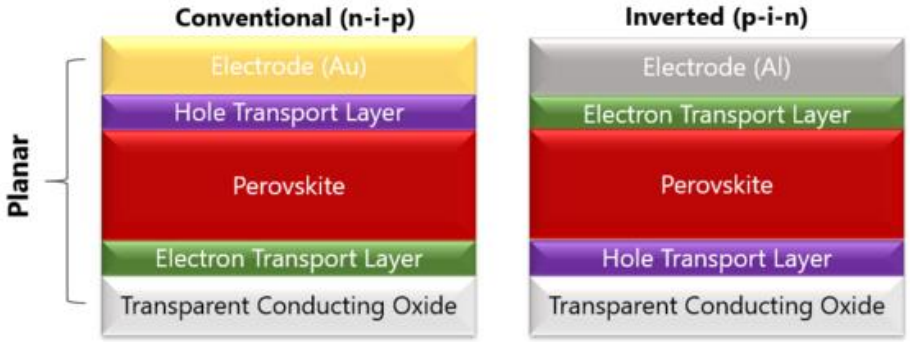


*Figure 1.3 Device architecture of (a) planar n-i-p and, (b) inverted planar p-i-n perovskite solar cells. Adapted from [24]*

In planar architecture, the main function of the hole transport layer (HTL) is to collect holes from perovskite absorber layer, carry it towards the cathode, and block electrons from recombination. The hole transport material should have HOMO (highest occupied molecular orbital) slightly higher or nearly match the perovskite absorber layer [25]. Other general requirements include (1) high mobility for efficient hole transport (possibly $>10^{-3}$ $cm^2V^{-1}s^{-1}$) in order to conduct the hole and prevent recombination; (2) Smooth and pinhole-free layer of HTM to avoid direct contact between the perovskite absorber layer or metal electrode; (3) high optical, thermal, chemical, air, and water stability [26], [27]. On the other hand, the electron transport materials (ETM) must collect electrons from the absorber layer and transport them to the anode and block holes. The LUMO (lowest unoccupied molecular orbital) of ETM must be less than the perovskite layer's conduction band. The ETMs should acquire high transmittance in the UV–Vis region, so all the photons pass through it. Also,

transport layers must exhibit the properties, such as good thermal stability, and must be resistive towards external degrading factors [15]. The perovskite solar cells with high performance usually adopt the planar n-i-p architecture and commonly apply $TiO_2$ as an ETL. However, the serious hysteresis behavior due to the deep charge traps in the $TiO_2$ layer and UV light-induced oxygen vacancies has prevented the correct evaluation of their device performance [28]. As an alternative, organic materials have been used to fabricate the transport layer of perovskite solar cells. The most commonly used organic ETL is fullerene derivatives such as phenyl-$C_{61}$-butyric acid methyl ester (PCBM) and buckminsterfullerene ($C_{60}$).

## 1.4 Electron transport layer: $C_{60}$ fullerene

Fullerene was firstly introduced by Kroto in 1985, which later won the Nobel Prize in 1996 for this discovery [29]. Fullerene takes the spherical shape of graphene and has a pyramidalization angle depending on the number of carbon atoms. This pyramidalization can force the geometry of fullerene to form a spherical shape [30]. Among other fullerene materials, the most commonly known and most stable structure is $C_{60}$, which has a pyramidalization angle of 11.6°, meaning that a 101.6 angle was formed between $\sigma$ and $\pi$ orbitals. Fullerene $C_{60}$ is an allotrope of carbon that has a closed-cage structure, and it is icosahedrally shaped with 60 $sp^2$ hybridized carbons. It is majorly utilized in the development of novel materials for a wide range of energy-based applications. The electronic and optical properties of $C_{60}$ thin film show the crystallization of $C_{60}$ was face-center cubic (FCC) structure [31].

There has been an increasing interest in the application of $C_{60}$ fullerene as ETL in perovskite solar cells due to their superior abilities in transporting electron and hysteresis suppression [32]–[35]. However, since $C_{60}$ is a non-polar molecule, which has low solubility in organic solvents, and the hydrophobic nature of $C_{60}$ molecules results in the discontinuous $C_{60}$ thin film on the hydrophilic substrate when using the solution-based process, e.g., spin coating [36]. Thus the carrier mobility in the spin-coated $C_{60}$ thin film is low due to randomly distributed and $C_{60}$ molecules [35], which limits device performance. To overcome this problem, $C_{60}$ is usually used in inverted structures and fabricated via the thermal evaporation process. Thus, the hydrophobic nature then can also contribute to the prevention of moisture penetration in the perovskite layer [11], [34].

It also has been reported by Yoon et al. that fullerenes can act as grain boundaries passivation and reduce the trap states [28]. Thus, less hysteresis and low SRH recombination can be obtained. They showed that using $C_{60}$ as ETL with planar-type architecture exhibited a power conversion efficiency (PCE) of 19.1% due to high electron mobility of 1.6 $cm^2/Vs$. They combined the thermal evaporation process with an ultra-high vacuum to minimize the kinetic energy loss of evaporated particles. Another study from Liu et al. presented a novel inverted PSCs with room temperature vacuum-deposited $C_{60}$ ETL. They observed that the thickness of $C_{60}$ significantly influences the device's performance. By varying the thickness of $C_{60}$ thin films to 12, 18, and 24 nm, the champion PCE of 16.78% was obtained at the thickness of 18 nm, with $V_{oc}$ = 1.075V, $J_{sc}$ = 20.63 $mA/cm^2$, and FF = 75.4% [34]. A study from Kun-mu Lee indicated that less than 10 nm-thick $C_{60}$ film in regular-type perovskite solar cells resulting power conversion efficiency less than 9% due to small fill factor as the effect of small coverage of $C_{60}$ on the transparent conductive oxide [35].

While all of the aforementioned studies have demonstrated the potential of $C_{60}$ as an electron transport layer and the effect of thickness on the PSCs performance, but the optimum thickness of the $C_{60}$ layer is still debatable, there is still a lack of data regarding the

optimum thickness of $C_{60}$, the exact deposition kinetics, and the effect of deposition rate on the interface and surface morphology, particularly in the thermal evaporation process. Thus, further study is required to fulfill these knowledge gaps.

Therefore, the detailed knowledge of the $C_{60}$ film growth mechanism and the resulting morphological properties from the thermal evaporation process is essential both from fundamental and technological perspectives. On top of that, the exact deposition kinetics and the effect of deposition parameters on optoelectrical properties require further investigations to understand the physical characteristics of the film.

## 1.5 Challenges in perovskite optical characterization

Nowadays, empirical research shows that the emergence of perovskite materials and device performances have thrived significantly, with studies of optimization of fabrication techniques leading the progress [15]. As perovskite solar cells are still on the way to reaching the theoretical efficiency limit for a single junction, which is 31% [10],[37], fine-tuning of the device structure is required for further optimization. The optimization can be feasible with the assistance of optical simulations, which require precise knowledge of the optical properties of device layers [38]. Furthermore, one of the most promising applications to surpass the theoretical efficiency limit is tandem solar cells, where the design also requires extensive optical modeling [38], [39].

The stereotypical material for studying the properties of perovskite material is $CH_3NH_3PbI_3$ ($MAPbI_3$), which has been characterized intensively, revealing remarkable optical and electrical properties. While the potential of $MAPbI_3$ perovskite and optical constant has been pointed out in many literature [40]–[42], the refractive index spectra for perovskite with mixed-cation lead mixed-halide, particularly for $Cs_xFA_{1-x}PbI_{3-x}Br_x$ perovskite, were not comprehensively observed. This material's stoichiometry has significantly improved the stability issues and tuned to a wide-bandgap perovskite compared to classical PSCs like $MAPbI_3$. As such, they hold great potential for single-junction solar cells, and especially for semi-transparent top cells in perovskite/silicon tandem cells. Therefore, for a thorough optical design of multilayer photonic devices, accurate knowledge of the complex refractive index or, equivalently, the complex dielectric constant and optical bandgap with cesium mixed-cation lead mixed-halide is of great importance [38], [41], [43].

## 1.6 Thesis objectives and research questions

This thesis activity focuses firstly on developing a high-quality electron transport layer fabricated via the thermal evaporation process and extraction of its optical constants. In particular, the project covers the following objective:

- Develop $C_{60}$ electron transport layers via thermal evaporation to optimize the deposition processes, uniformity, and optical properties.

The second objective is to construct the model for extracting the optical constants and understanding the optical behavior of $Cs_xFA_{1-x}PbI_{3-x}Br_x$ perovskite material. Note that the fabrication and optimization of the $Cs_xFA_{1-x}PbI_{3-x}Br_x$ perovskite absorber layer using thermal evaporation were performed by another member of our group. However, the author was actively involved in the characterization process and checked the perovskite for the modeling purpose was in good condition, mainly by observing the crystallinity phase from the X-ray diffraction pattern. Nevertheless, the fact that the optical constant of this type of material was not comprehensively studied in our laboratory, thus the second main scientific goal is:

- Investigate the optical constant of $Cs_xFA_{1-x}PbI_{3-x}Br_x$ perovskite using dispersion models and validating the obtained results with experimental data

Once the extraction of optical constants for all layers is ready, the optical simulation is performed at the device level, where the main research goal is:

- Identify both the photocurrent density of the perovskite absorber layer and the losses caused by parasitic absorption in the supporting layers through optical simulation

Therefore, there are three main research questions that will be answered by the end of this project :

1. How to develop the selected transport layers of perovskite solar cells using the thermal evaporation method to optimize the film quality?
2. How to optically model the transport layers and perovskite absorber layer in order to extract the optical constant of each material?
3. How to identify the optical losses and contribution of supporting layers on parasitic absorption on perovskite solar cells optical simulation?

The main research questions then could be elaborated and divided into several sub-questions (SQ):

- **SQ-1a:** What are the optimum parameters for the $C_{60}$ deposition process using the thermal evaporation process?
- **SQ-1b:** What is the effect of layer thickness of the electron transport layer to provide the best overall surface uniformity and crystallinity?
- **SQ-1c:** What is the effect of the deposition rate on the surface morphology and optical constant of $C_{60}$?
- **SQ-2a:** What is the most suitable model to extract the complex refractive index and dielectric function for the $C_{60}$ transport layer and $Cs_xFA_{1-x}PbI_{3-x}Br_x$ perovskite?

- **SQ-2b:** How to accurately determine the optical transition energy in $Cs_xFA_{1-x}PbI_{3-x}Br_x$?
- **SQ-3a:** How to systematically find the supporting layers' contribution to the parasitic absorption and optical losses in an optical simulation?
- **SQ-3b:** What is the effect of $C_{60}$, with the different thickness and deposition rate on the optical losses on p-i-n perovskite solar cells and semi-transparent perovskite solar cells?

## 1.7 Thesis structure

This report comprises seven chapters which are organized as follows:

**Chapter 1:** highlights the current development of solar cells and the knowledge gap in developing perovskite solar cells. This chapter also emphasizes the scope of this study, including the research questions, objectives, and sub-goals, which show the state of the art of this study.

**Chapter 2**: the theoretical framework is provided to give a general overview of perovskite material and the basic working principle of solar cells in general. It starts from the generation of charge carriers, transport mechanism, and recombination losses. Moreover, a review of $C_{60}$ material as a candidate for ETL in semi-transparent perovskite solar cells is also thoroughly explained and supported by a literature study of involved parameters for a high-quality $C_{60}$ layer. The last section in Chapter 2 is devoted to a basic theory and explanation of some optical models for transparent and absorbing materials.

**Chapter 3:** represents the research methodology to cope with the thermal evaporation process for the selected electron transport, the required characterization technique for validation and confirmation of the resulting experiment.

**Chapter 4:** elaborates the results from processing parts to materials morphology and optical properties of $C_{60}$ transport layer with different deposition rates and layer thickness. The comprehensive analysis is performed and supported by the discussion from the previous literature.

**Chapter 5:** extensively elaborates step-by-step procedure for obtaining the complex refractive index of $Cs_xFA_{1-x}PbI_{3-x}Br_x$ perovskite. The validation step for the model is also presented.

**Chapter 6:** applies the complex refractive index from each layer and optically simulates the performance of the perovskite solar cells by identifying the amount of reflected light, parasitic absorption, and implied photocurrent density of perovskite solar cells in both p-i-n structure and semi-transparent perovskite solar cells.

**Chapter 7:** concludes the main findings of this study and shows the position of this project to become a stepping stone for the research on the $C_{60}$ transport layer and identification of complex refractive index of wide band-gap $Cs_xFA_{1-x}PbI_{3-x}Br_x$ perovskite materials processed via thermal evaporation method. Furthermore, the outlooks are given for future research related to electron transport layer studies and optical simulation of perovskite solar cells.

# 2
# Theoretical Framework

## 2.1 Perovskite

Perovskite is a mineral of calcium titanium oxide ($CaTiO_3$) and was found by Gustav Rose in Russia's Ural Mountains in 1939. Then, a Russian mineralogist, Count Lev Alekseevich Perovski, further carried the research. Thus, the material was named after him as 'Perovskite.' In the 1990s, Mitzi et al. observed the optoelectronic properties of the organic-inorganic perovskites showed that the material provided strong exciton features, and further reported that it could be utilized in the field of light emitting diodes (LDEs), transistors, and solar cells [44].

### 2.1.1 **Structure**

The term perovskite nowadays indicates a wider range of materials, including metal halide perovskite with the $ABX_3$ crystal structure, where A is the monovalent cation (organic/inorganic), B is a smaller bivalent dication, and X is the halide anion. Figure 2.1a shows the crystal structure of the perovskite material and the position of each atom. The ideal perovskite structure has the highest symmetry of the cubic structure, where the small anions X together with the cations B build octahedral network occupies the corner of the structure while larger A cation occupies the interstices [13], [45].

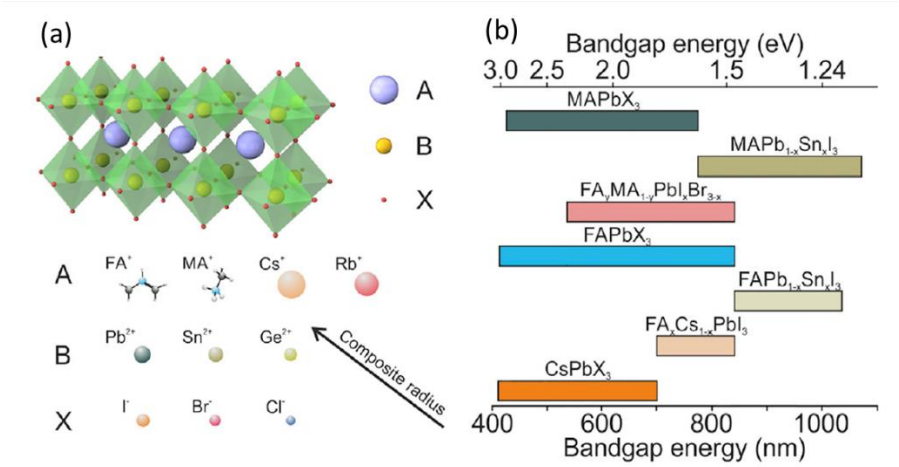


*Figure 2.1 Schematic representation of (a) crystal structure of perovskite and (b) bandgap tunability of $ABX_3$ perovskites. Adapted from* [46]

One of the most interesting features offered by $ABX_3$ perovskite is the possibility to tune their bandgap (absorption onset) by one or two atom site substitution. Figure 2.1b shows some of the examples of typical A, B, and X elements occupying different positions in the perovskite structure and bandgap changes with the different combinations of elements in a perovskite structure.

These different compounds must be tuned wisely to maximize solar photon absorption and achieve structural stability. For example, if the ionic radius of A is too small, it cannot separate two B atoms effectively, which leads to an edge-sharing octahedron. In contrast, high ionic radii of A would lower the dimensional face-sharing octahedral structures, which reduces the effectiveness of solar photon harvesting due to reasons such as wider bandgap [18].

### 2.1.2 **Structural stability**

The structural stability of perovskite structure can be determined by the Goldschmidt tolerance factor (*t)* with the simple expression of [47]:

$$t = \frac{R_A + R_X}{\sqrt{2}\,(R_A + R_X)} \tag{2.1}$$

where $R_A, R_B$ and $R_x$ are the ionic radii of the A, B, and X ions, respectively. Ideally, $t > 1$ results in hexagonal or tetragonal structures and $1 > t > 0.9$ exhibits cubic structure, $0.9 > t > 0.71$ produces an orthorhombic or rhombohedral structure, and $t < 0.71$ shows no perovskite crystal structure [18]. The additional consideration for perovskite formation is the octahedral factor (μ) (Eq. 2), which is used to determine the distortion and stability of the perovskite structure.

$$\mu = \frac{R_B}{R_x} \tag{2.2}$$

Where the perovskite is stabilized for an octahedral factor ranging from 0.45 to 0.89 [13], [48].

One of the most commonly investigated perovskite absorber materials is methylammonium lead halide ($MAPbI_3$) with tolerance factor of $t = 1.02$ and it forms a tetragonal structure at room temperature. However, the aspherical shape and larger size of methylammonium (MA) leads to distortion in the structural network, causing a phase transition with the temperature changing. For instance, at $T < 160\ K$, it forms an orthorhombic structure, for $162.2 < T < 327.4\ K$ is a tetragonal structure, and for $T > 327.4K$ the cubic structure is observed [49]. The phase transition changes the electronic band structure and the resulting optoelectronic properties of material.

The $MA^+$ cation in $MAPbI_3$ perovskite has also been substituted with formamidinium ($CH(NH_2)_2^+$, $FA^+$) cation (shown in Figure 2.1b), resulting in a comparatively narrower bandgap of 1.48 eV, indicating larger current extraction when employed as the absorber layer [50]. Replacing one or more elements or molecules in the perovskite structure might also lead to other effects, such as material stability. For example, replacing $MA^+$ with $FA^+$ results in lower intrinsic stability of the resulting perovskite material. The reason can be found in the larger size of $FA^+$ (2.79 Å) compared to $MA^+$ (2.70 Å), which tilts the metal-halide octahedra structural stability with slightly increasing the tolerance factor to 1.04 [46]. At room temperature, the yellow-δ-phase with hexagonal is the stable crystal structure for $FAPbI_3$ [51]. It has been proposed in literature that introducing cesium ions ($Cs^+$) can compromise

the large size of $FA^+$ and improve the stability by reducing the tolerance factor [51]. Hence, mixing cations is a valuable approach to control the perovskite structure toward more stable and efficient PSCs [52].

## 2.2 Physics in perovskite material

### 2.2.1 **Excitons**

When the atom of semiconductor materials absorbs the incident light, an electron in the conduction band and a hole in the valence band are created. The electron and hole attract each other due to Coulomb forces forming a quasiparticle, namely exciton, which was first predicted by Yakov Franel. The electron-hole pairs' energy binding dictates the behavior of charge carriers in a crystalline material. It is categorized into two types (Frenkel and Wannier-Mott excitons), as shown in Figure 2.2. The Frenkel excitons are observed mostly in organic semiconductor materials or molecular crystals. In the Frenkel exciton, the Bohr radius is approximately limited to a single unit cell. On the other hand, the quasiparticles formed due to Coulomb forces and are typically observed in the inorganic semiconductor are called Wannier-Mott excitons. The distance between the electron and hole is significantly larger than the crystal lattice constant. The equation for Wannier-Mott can be described as follows:

$$r = n^2 a^* \tag{2.3}$$

where $a^* = \hbar^2 \varepsilon_r / \mu e^2$ is the effective Bohr radius to represent the distance between the hole and electron in the ground state $(n = 1)$

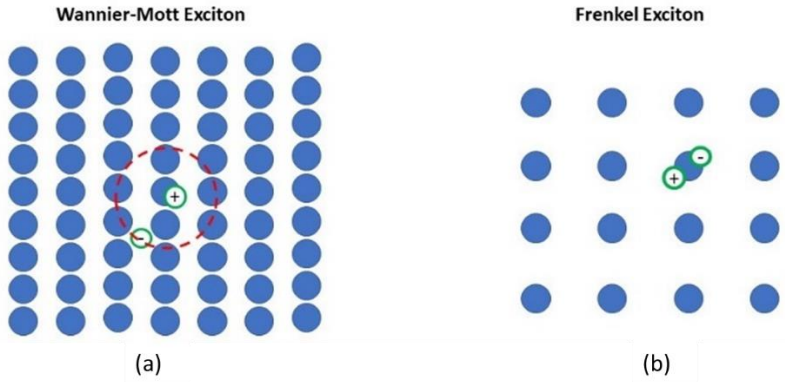


*Figure 2.2 Illustration of (a) Wannier-Mott and (b) Frenkel excitons overlayed on lattice structures* [53].

The exciton binding energy dictates the nature of charge generation in photoactive materials. If the exciton binding energy is high, then the exciton must diffuse through the photoactive material [54] to an interface where an electron can be fully dissociated and extracted from the material. Thus, the diffusion length before recombination will be a problem in optoelectronic devices, particularly in the maximum thickness of the photon absorbing layer. When the exciton binding energy is low, the exciton can dissociate spontaneously due to the availability of free energy higher than exciton binding energy. At room temperature, the free energy term is approximately 25 meV [55].

The exciton binding energy of particular semiconductor material is a function of the dielectric constant of that material. The coulomb attraction force between electron-hole pairs will be low if the dielectric constant is low, as well as lowering the exciton binding energy. The common formula to measure the exciton binding energy in a material is shown below

$$E_B = \frac{\mu e^4}{2\hbar^2 \varepsilon^2} \tag{2.4}$$

Where $E_B$ is the exciton binding energy, $\mu$ is the effective mass of the electron, ε is the dielectric constant [56].

### 2.2.2 **Absorption of incident photons**

The absorbed photon can excite an electron from a lower energy state to a higher energy state. Thus, to absorb the photon energy, at least a two-level energy system is needed. A semiconductor material can utilize the photon energy if the lifetime of the carrier at the excited state must be greater than the time required for a carrier transfer from a lower energy state (valence band) to a higher energy state (conduction band) [56]. The difference between these energy levels is called the "band-gap" of the materials.

The valence and conduction bands' energy varies depending on the momentum of the charge carriers, as in Figure 2.3. In direct semiconductors, the conduction band's minimum energy occurs at the same momentum as the maximum energy of the valence band. In indirect semiconductors, the maxima and minima do not coincide. This means that for an electron to be promoted to the conduction band, a phonon must also be created to conserve momentum.

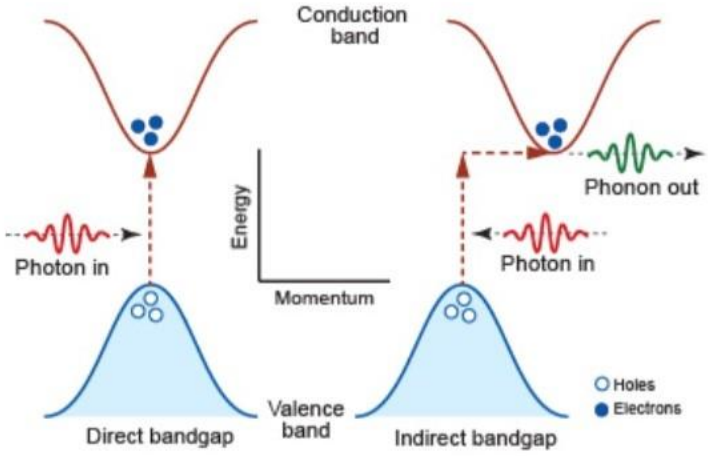


*Figure 2.3 Promotion of an electron in (left) direct and (right) indirect bandgap* [57]

The ability of certain material in absorbing layer can be defined by absorption coefficient, which is a function of wavelength incident photon. For direct band-gap semiconductors, the absorption coefficient can be described by

$$\alpha = A\left(hv - E_g\right)^{\frac{1}{2}} \tag{2.5}$$

where A is the proportional constant (a function of effective electron and masses). Meanwhile, for the indirect band-gap, the absorption coefficient is given by

$$\alpha = \frac{A\left(hv - E_g + E_p\right)^2}{e^{\frac{E_p}{kT}} - 1} \tag{2.6}$$

where $E_p$ is the absorbed photon energy. The light intensity will go down exponentially as the light travels through the material. To express this statement, Eq. 5 can be used to determine how much light has been absorbed for a given thickness of a certain material.

$$I = I_0 e^{-\alpha x} \tag{2.7}$$

where $\alpha$ is the absorption coefficient, $I$ is the intensity at distance x, and $I_0$ is the intensity of light before any absorption.

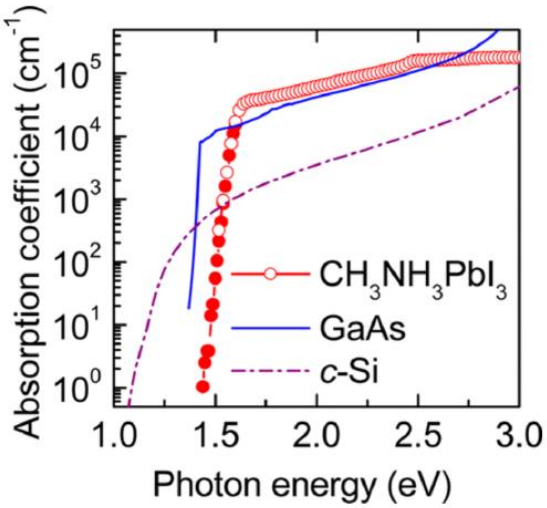


*Figure 2.4 The absorption coefficient of different semiconductor materials* [58]

The absorption coefficient is very important in photovoltaics applications as it defines how much light the semiconductor can absorb within a given thickness. A material with high absorption coefficient will absorb more light. As such, a semiconductor material with a higher absorption coefficient needs a thinner layer to absorb the same light fraction. Figure 2.4 represents several absorption coefficients of different semiconductor materials. In the visible light wavelength range, the absorption coefficient of perovskite $MAPbI_3$ is better (higher) than c-Si, which has an indirect band-gap and is comparable to those which have a direct band-gap (GaAs) [59].

## 2.3 Transport and loss mechanism of charge carriers

When light pulses illuminate the material, it leads to electron excitation from the valence band to the conduction band and, consequently, triggers the creation of holes in the valence band. This illumination will disturb the semiconductor from the state of thermal equilibrium. The excess holes concentration will be present in the valence band as well as the electron concentration in the conduction band, which are larger than the equilibrium concentration, i.e., $p > p_0$ and $n > n_0$, where $p_0$ and $n_0$ represent the holes and electrons equilibrium concentration, respectively [53].

The photo-generated electrons and holes interact with each other electrostatically, with a binding energy $E_B$ required to separate them into free carriers. The exciton binding energy to be lower than thermal energy (1/kT) is preferred, where k is Boltzmann constant, and T is temperature. For organometal trihalide perovskite, at room temperature, the $E_B$ has been approximated to be < 5 meV [16]. Since this $E_B$ value is much lower than the thermal energy at room temperature (25 meV), $MAPbI_3$ solar cells cannot be excitonic [16], [55]. Thus, the light absorption in $MAPbI_3$ creates free electrons and holes at room temperature. In contrast, if the exciton binding energy is higher than thermal energy, then photon absorption creates exciton, and it requires external energy to generate free electrons and holes.

The free charges are then transported to the selective charge transport layers, namely the Electron Transport Layer (ETL) and Hole Transport Layer (HTL), to transport only one type of carrier (and block the other) to the respective electrode for extraction. The schematic representation of typical PSCs and charge transport is shown in Figure 2.5

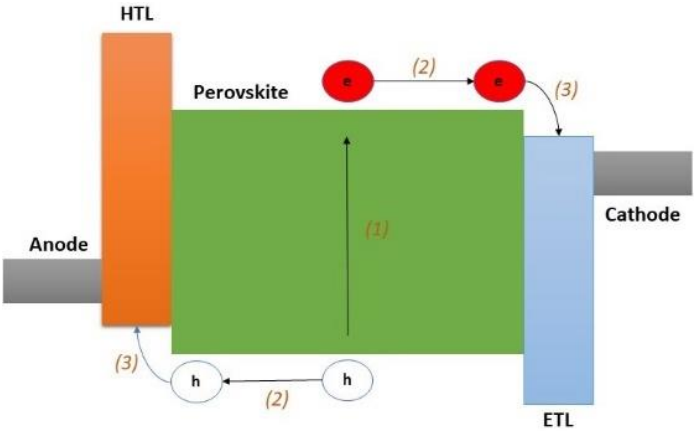


*Figure 2.5 The schematic of a perovskite solar cell model. Step (1): The perovskite absorber layer generates free electrons and holes upon light absorption. Step (2): Transport of charge carriers by drift and diffusion. Step (3): Charge carrier transfer to respective transport layers and eventually extraction at the electrodes*

### 2.3.1 **Charge recombination in perovskite solar cells**

After the illumination stops, these extra electrons will recombine again with holes until equilibrium is achieved. Generally speaking, the electron in the conduction band is in a meta-stable state and will eventually move to a lower energy position in the valence band [60]. When this happens, the hole in the valence band will move and recombine with the electron to form an electron-hole pair.

In perovskite solar cells, there occur a few different types of recombination. The rate of this recombination will strongly affect the performance of the solar cell. The more recombination, the higher the saturation of current density. The recombination also reduces the charge carriers that contribute to the photocurrent [53]. This will have an adverse effect on the solar cells' open-circuit voltage, limiting their power conversion efficiency. The illustration of different types of recombination is shown in Figure 2.6

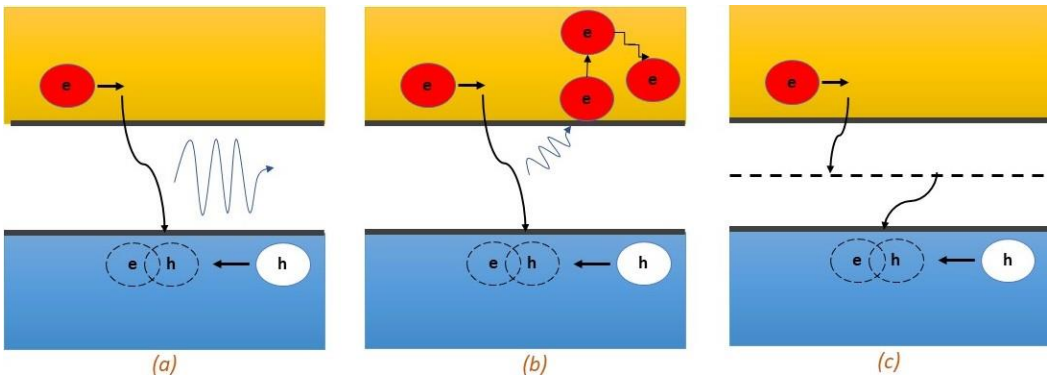


*Figure 2.6 Schematic representation of (a) radiative recombination, (b) Auger, and (c) Shockley-Read-Hall (SRH) recombination* [53].

In perovskite solar cells, the free charge carriers can recombine in two ways: radiative (bimolecular recombination) and non-radiative recombination (Auger and SRH recombination). Many researchers have shown that radiative recombination is weak [61]–[63] in perovskite solar cells compared to non-radiative recombination, which is the dominant recombination mechanism, particularly SRH recombination [64], [65].

### *Radiative recombination*

Radiative Recombination is a recombination mechanism that usually takes place in direct band-gap semiconductors [60]. In radiative or bimolecular recombination, there is direct recombination of an electron in the conduction band with a hole in the valence band and releases a photon (Figure 2.6a). This emitted photon has an energy equal to the band-gap ($E_{gap}$) of the material. The equation for bimolecular recombination rate $R_B$ is expressed as [25]

$$R_B = \gamma\left(np - n_i^2\right) \tag{2.8}$$

where $n$ is electron density and $p$ is hole intensity, $\gamma$ is the recombination coefficient, and $n_i$ is the intrinsic carrier concentration.

### *Auger Recombination*

Auger recombination is nonradiative recombination where the energy and momentum of a recombining electron-hole pair are transferred to another electron (or hole) in the conduction (or valence) band and not releasing a photon (Figure 2.6b). This occurs when three charge carriers are involved at high charge carrier densities [66]. In an indirect band-gap semiconductor, this recombination mechanism cannot be avoided. However, under very low light intensity (non-concentrated sunlight) for perovskite solar cells, Auger recombination is negligible [25].

The recombination equation can be written as follows:

$$R = \left(C_n^A + C_p^A\right)\left(np - n_i^2\right) \tag{2.9}$$

Where R is the recombination rate and concentration $C_n^A$, and $C_p^A$ are constants.

### *Shockey-Read-Hall recombination*

The perovskite material with a direct band-gap contains many intrinsic defects, including point defects within the perovskite crystals and impurities at grain boundaries and surface [67]. As a consequence of these defects, trap states for both electrons and holes can induce the non-radiative recombination, namely Shockley-Read-Hall (SRH) recombination. In the SRH recombination, the recombination of electrons and holes does not occur directly from band-gap to band-gap but through the trap defects (Figure 2.6c). The mechanism of this recombination consists of two steps, which are [60];

- Firstly, the electron or hole is trapped by an energy state in the forbidden region, so-called *trap states*, because of the defects in the perovskite crystal lattice. These defects might originate from impurities, grain boundaries, or additional doping material.
- Recombination then occurs if an electron (or hole) goes in the same energy state before the electron is thermally re-emitted into the conduction band. The heat created during the recombination is dissipated into the lattice in the form of vibrations (phonon).

The charge carriers' movement into the forbidden gap's energy level depends on the distance of the introduced energy level from either of the band edges. In crystalline semi-conductors (c-Si), the SRH recombination is predominantly due to the mid-gap trap state. In perovskite solar cells, with some degree of energetic disorder, tail states, defined as localized states energy levels inside the electronic gap near the conduction or valence band, increasing the SRH recombination by increasing the effective density of trap states [68]. Shockley-Read-Hall (SRH) theory describes the recombination through defects states as [22], [25].

$$R = \frac{\left(np - n_i^2\right)}{\tau_p(n + n_0) + \tau_n(p + p_0)} \tag{2.10}$$

with $\tau_{n,p}$ are the lifetimes for electrons and holes, respectively. The $n_1 = N_c exp(-\frac{E_C - E_T}{k_B T})$, $p_1 = N_V exp(-\frac{E_T - E_V}{k_B T})$ and $E_T$ is the energy of the trap.

The recombination which happens at the surface of the perovskite is called an 'interface' SRH recombination. The equation for surface recombination rate is described as follows:

$$R = \frac{J_{p,(cathode)} - J_{n,(anode)}}{qL} \tag{2.11}$$

Where $J_{p,(cathode)}$ and $J_{n,(anode)}$ are the hole and electron current densities at the cathode and anode, respectively, and q and L are the electronic charge and distance between the electrodes, respectively.

### 2.3.2 **Ion migration**

In 2015, Xiao et al. firstly revealed the influence of ion migration on the photoelectric behavior of perovskite devices [69]. The authors reported that the giant switchable photovoltaic effect in organometal trihalide perovskite solar cells with a planar heterojunction structure and symmetric electrode. The results provided strong and solid shreds of evidence for the presence of electric field-induced ion migration [22]. Furthermore, the effects of ion migration, together with trap states filling and unfilling, explain many intrinsic properties of perovskite solar cells, such as reversible degradation and hysteresis of device performance.

#### *Reversible Losses*

Gomez et al. reported that the combination of illumination and applied voltage results in non-reversible and reversible degradation in the perovskite layer [70]. Moreover, non-reversible performance losses in a perovskite film originate from degradation localized at the grain boundaries. Since ions and ion vacancies migrate through defects, a highly defects concentrated (small size of grain boundaries) will largely contribute to the ion migration pathway [52].

However, halide perovskite solar cells also exhibit reversible losses due to ion migration within the perovskite film. At the bulk of the perovskite grains, Gomez et al. found interesting fully reversible behaviors [70]. Thus the grain boundaries are detrimental to the device stability, and they need to be minimized or passivated to achieve more stable perovskite solar cells.

*Hysteresis*

Generally, solar cell devices' efficiency is evaluated by measuring the current while sweeping an applied voltage under standardized illumination conditions (AM 1.5, 100 mW $cm^2$ irradiation) [22]. However, in this measurement, i-V curves' shape changes with specific measurement conditions, e.g., the non-overlap of i-V curves under different scan directions (forward/reverse) and different scan/voltage speeds, which is also known as hysteresis. In order to explain the origins of the J-V hysteresis, Snaith et al. have reported 3 mechanisms, i.e., ferroelectricity, charge trapping, and Ion migration effect [71]. Hysteresis provides a serious issue on accurate determination of the perovskite solar cells efficiencies and stability [72].

Mitigation of this hysteresis would be achieved for an inverted planar architecture, where n-type fullerene layer was infiltrated in-between device layers [72]. The authors demonstrated that the presence of Phenyl-$C_{61}$-butyric acid methyl ester (PCBM)/$C_{60}$ double fullerene layer could completely remove the hysteresis after annealing the PCBM layer for 45 minutes. Thus, fullerene can effectively passivate the large density of charge traps in annealed $MAPbI_3$ films and increase efficiency and stability.

## 2.4 Spectroscopic ellipsometry

Spectrocopic ellipsometry (SE) is one crucial measurement technique for the extraction of optical constant and the study of thin-film characteristics, including film thickness and morphology. The extracted optical constants are not only important for the understanding of the optical energy transitions but are also an essential input parameter for numerical optical simulations of solar cells. This section will describe the fundamental of ellipsometry and the interpretation of ellipsometry data.

### 2.4.1 **Polarized light**

The basic principle of ellipsometry is shown in Figure 2.7. As known well, light is an electromagnetic wave and has electric and magnetic field components. In ellipsometry, however, only the electric field ($E_f$) component of the light wave is considered. When light waves are polarized, the electric fields are oriented in specific directions. For the light reflection on samples, depending on the oscillatory direction of the electric field, the light polarization is classified as p- and s-polarizations. The p-polarizations is parallel to the incident plane, while that of the s-polarization is perpendicular [73].

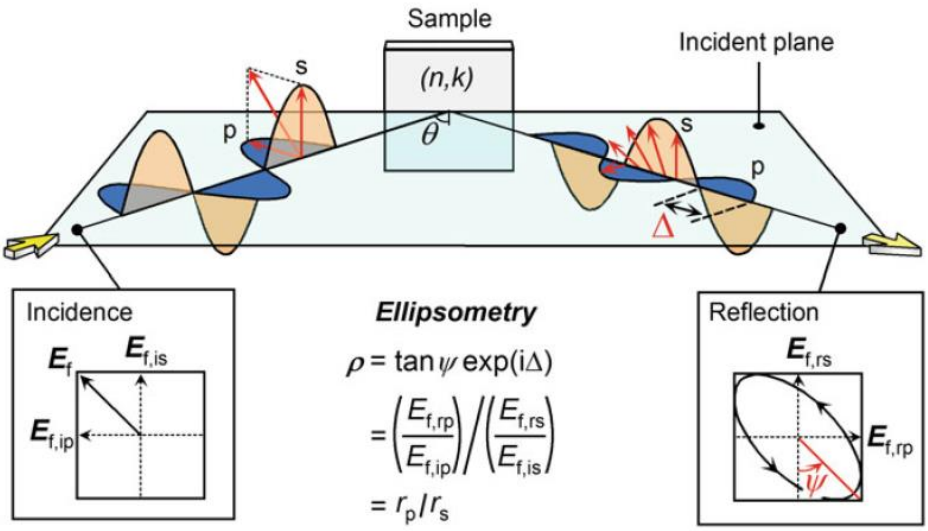


*Figure 2.7 Basic principle of ellipsometry* [74]. *The electric field (Ef) vector and the subscripts "i","r","s",and "p" for Ef denote the incidence, reflection, s-polarizations, and p-polarizations, respectively. The synthesized vectors for p- and s-polarizations are shown by red arrows.*

Ellipsometry measures the amplitude ratio *ψ* and the phase difference *Δ* between the p- and s-polarizations. Due to the difference in the oscillatory direction between $E_{f,ip}$ and $E_{f,is}$ , each polarization shows different light reflections as well. The amplitude and the phase between the p- and s-polarized light change depending on the optical constant and film thickness [74].

The *ψ and Δ* from ellipsometry measurement are defined by

$$\rho = \tan\psi \exp(i\Delta) = \frac{(\frac{E_{f,rp}}{E_{f,ip}})}{(\frac{E_{f,rs}}{E_{f,is}})} \tag{2.12}$$

As we can observe in Figure 2.7, since $E_{f,ip} = E_{f,is}$, there is no phase difference between the polarization, and the amplitudes of p- and s-polarizations are same. Thus Eq. (2.12) above can be rewritten as $\tan\psi \exp(i\Delta) = E_{f,rp}/E_{f,rs}$.

Moreover, the amplitude reflection coefficients for the p- and s-polarizations are described as

$$r_p = \frac{E_{f,rp}}{E_{f,ip}} = |r_p| \exp(i\delta_p) \tag{2.13}$$

$$r_s = \frac{E_{f,rs}}{E_{f,is}} = |r_s| \exp(i\delta_p) \tag{2.14}$$

where $|r|$ and $\delta$ are amplitude ratio and phase difference between the incident and reflected waves, respectively. Combining the above relations, we obtain a simple equation:

$$\rho = \tan\psi \exp(i\Delta) = \frac{r_p}{r_s} \tag{2.15}$$

And from Eq. (2.12) – Eq. (2.15)

$$\tan \psi = \frac{|r_p|}{|r_s|}, \qquad \Delta = \delta_p - \delta_s \tag{2.16}$$

### 2.4.2 **Refractive index and dielectric function**

There are two common descriptions for the optical constants of material: the complex refractive index ($N = n - ik$) and the complex dielectric function ($\varepsilon = \varepsilon_1 - i\varepsilon_2$) [74]. Both are related by:

$$\varepsilon = \varepsilon_1 - i\varepsilon_2 = N^2 \tag{2.17}$$

with

$$\varepsilon = n^2 - k^2 \tag{2.18}$$

$$\varepsilon = 2nk \tag{2.19}$$

In a complex refractive index, the term "$n$" is the index of refraction, and "$k$" is the extinction coefficient. The index of refraction describes the phase velocity of light within a material ($v$) compared to the velocity in vacuum ($c$):

$$n = \frac{c}{v} \tag{2.20}$$

And the extinction coefficient, k, is related to light absorption as it travels through a material. Thus, the extinction coefficient is related to the absorption coefficient by:

$$\alpha = \frac{4\pi k}{\lambda} \tag{2.21}$$

Moreover, the complex refractive index itself is determined from the dielectric polarization generated in a medium. The dielectric polarization represents the phenomenon that external electric fields separate electric charges in a medium [73]. During the interaction between light and materials, the electric fields create oscillating charge dipoles within atoms or between atoms. Each dipole creates an electromagnetic field and will absorb some of the energy at certain oscillation frequencies. Each dipole field combines with the fields from other dipoles as well as the incident field, resulting in the total macroscopic field within the materials [74]. The dielectric function shows the relation between the displacement of total macroscopic field (D), the incident field (E), and electric polarization (P):

$$D = \varepsilon_0 E + P = \varepsilon\varepsilon_0 E \tag{2.22}$$

Where $\varepsilon_0$ is the permittivity of free space, and $\varepsilon$ is the dielectric constant. From the equation, $\varepsilon$ is a constant proportionality for D/E and describes the contribution from P, which is a function of the volume density and strength of the dipoles contained within the material. The dipole response, and therefore P, depends on how fast the electric field (E) oscillate. Thus $\varepsilon$ is a function of frequency $\varepsilon(\omega)$. The dipole response will also differ in both amplitude and phase from the oscillating electric fields of the incident light, making $\varepsilon(\omega)$ a complex value. Therefore the electric function contains a great deal of information about the material properties.

### 2.4.3 **Kramers-Kronig relation**

The Kramers-Kronig (KK) relations establish a physical connection between the real part ($\varepsilon_1$) and imaginary part ($\varepsilon_2$) as:

$$\varepsilon_1(E) = 1 + \frac{2}{\pi} P \int_0^{\infty} \frac{E' \varepsilon_2(E')}{E'^2 - (E^2)} dE' \tag{2.23}$$

$$\varepsilon_2(E) = -\frac{2E}{\pi} P \int_0^{\infty} \frac{\varepsilon_1(E')}{E'^2 - (E^2)} dE' \tag{2.24}$$

Where P is the principal part of the integral and E is the photon energy of the light.

Please note that these equations define the dielectric function as $\varepsilon = \varepsilon_1 + i\varepsilon_2$. These equations are the result of causality, where the response cannot precede the cause. As such, the material dipole response and absorption must occur after the electric field is applied. Kramers-Kronig (KK) consistency ensures that the compatibility of the measured and fitted data in a wide spectra range and provides physically consistent results [75]. The shapes of $\boldsymbol{\varepsilon_1}$ and $\boldsymbol{\varepsilon_2}$ are not independent. The KK relations provide the connection between their values. Thus, if one function can be described (either $\varepsilon_1$ *or* $i\varepsilon_2$), the second can be calculated. In addition to that, the KK relations also involve integration where the $\varepsilon_1$ the shape depends on the area under the $\varepsilon_2$ curve, and since the KK relations integrate over all photon energies, the $\boldsymbol{\varepsilon_1}$ at a given energy is affected by $\varepsilon_2$ at all energies.

The KK relations are very important during SE data analysis. They help limit the possible optical functions to only those that are physically plausible. It also greatly reduces the number of free parameters needed to describe complex optical functions.

### 2.4.4 **Dispersion model**

The choice of the structural model and the model dielectric function employed are critical to the extraction of reliable parameters from ellipsometry analysis [75]–[78]. The biggest challenge of ellipsometry is the fact that it is an indirect technique. In order to obtain any information characterizing the sample, the application of an appropriate model of dispersion is required. A dispersion model is a mathematical description of the optical constants as a function of wavelength. The dispersion function of a sample is required to evaluate the material's optical properties by adjusting specific fit parameters [79]. When the dispersion model of a sample is not known, then modeling the dielectric function is necessary. Below some of the models used in this study are briefly explained:

#### *Cauchy model*

The Cauchy dispersion model works best when the material has no optical absorption in the visible spectral range. The Cauchy model is written as:

$$n(\lambda) = A + \frac{B}{\lambda^2} + \frac{C}{\lambda^4} + \cdots \tag{2.25}$$

$$k(\lambda) = 0 \tag{2.26}$$

Where A is a dimensionless parameter, B sets the curvature and amplitude of the refractive index for medium wavelength, and C affects the curvature and amplitude for smaller wavelength [80]. Note that the Cauchy model is only accurate when $n(\lambda)$ follows normal dispersion, which means that the refractive index decreases with the increasing wavelength [80]. However, this model cannot be easily applied to semiconductor materials since the parameters do not have physical meaning, and therefore, the empirical relations are not Kramers-Kronig consistent. The Cauchy model is suitable for transparent materials like glasses.

## *Tauc-Lorentz*

The Tauc-Lorentz model provides a dispersion equation that only absorbs light above the material bandgap, and close to the band edge, the absorption of the Tauc-Lorentz equation follows the Tauc law formula:

$$\varepsilon_2(E) \propto \frac{(E - E_2)^2}{E^2} \tag{2.27}$$

Where *E* is the photon energy, and $E_g$ is the optical bandgap. In Tauc-Lorentz, the absorption is separated into two regions:

- $E > E_g$:

$$\varepsilon_2(E) = \frac{AE_0C\left(E - E_g\right)^2}{(E^2 - E_0^2)^2 + C^2E^2} \cdot \frac{1}{E} \tag{2.28}$$

- $E \leq E_g$:

$$\varepsilon_2(E) = 0 \tag{2.29}$$

Where A is the strength of the $\varepsilon_2$ peak, C is the broadening term of the peak, $E_o$ is the peak central energy.

While the value for the real part $\varepsilon_1$ of the dielectric function is derived from the expression of $\varepsilon_2$ using the Kramers-Kronig integration:

$$\varepsilon_1(E) = \varepsilon_1(\infty) + \frac{2}{\pi} P \int_{E_g}^{\infty} \frac{E'\varepsilon_2(E')}{E'^2 - E^2} dE' \tag{2.30}$$

Since the Tauc-Lorentz model requires the imaginary part $\varepsilon_2$ to be zero for energies less than bandgap, this model does not take into account intra-band absorption. This means that any defect or intra-band absorption increases the imaginary part below the bandgap and generates bad fits in that region [79].

## *B-spline model*

This model sums the individual basis function of the multiple polynomials to construct the final curve. The equation for a single basis function or “spline components” can be written as [73], [74]:

$$B_i^0(x) = \begin{cases} 1 & t_{i+1} \leq x < t_{i+1} \\ 0 & otherwise \end{cases} \tag{2.31}$$

$$B_i^k(x) = \left(\frac{x - t_i}{t_{i+k} - t_{i+1}}\right) B_i^{k-1}(x) + \left(\frac{t_{i+k+1} - x}{t_{i+k+1} - t_{i+1}}\right) B_{i+1}^{k-1}(x) \tag{2.32}$$

Where k is the degree of the b-spline. The common degrees such as 1, 2, 3, 4 correspond with linear, quadratic, cubic, and quartic equations, respectively. The most widely encountered spline is cubic (polynomial degree = 3) because this allows continuity of the function.

The summation of the overall shape of basis-spline function can be expressed as:

$$S(x) = \sum_{i=1}^{n} c_i B_i^k(x) \tag{2.33}$$

Where coefficient, c, is a parameter to adjust each spline component's amplitude. Figure 2.8 shows an example of a single 3rd-degree basis function from multiple polynomials, with the overall amplitude controlled by the coefficient of the basis function. The figure exhibits the individual spline components summed together to describe the imaginary part $\varepsilon_2$ of a material.

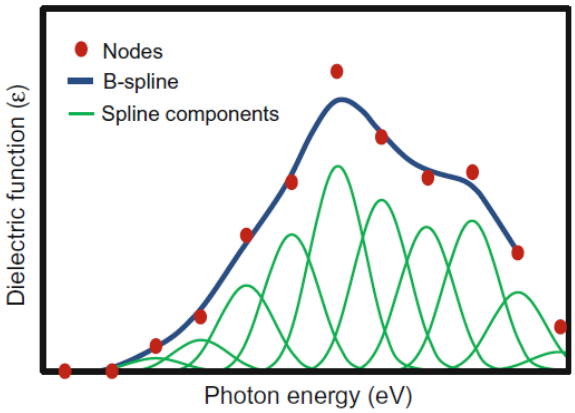


*Figure 2.8 Example of a b-spline curve of photon energy vs. dielectric function with a summation of basis functions controlled by their node amplitude* [74].

The specific shape is controlled by the associated "*c*" coefficient, shown here as nodes. In this project, the spacing between nodes is reduced to increase control over the shape of the final b-spline curve.

# 3
# Research Methodology

*The methodologies used on this project, including the materials, fabrication process, and characterization, are elaborated in detail below*

## 3.1 Materials

$C_{60}$ powders (Buckminsterfullerene) from Sigma Aldrich were used for the electron transport layer with 98% of purity. Formamidinium, lead iodide, and cesium bromide (99.99%) were used as perovskite precursors purchased from Dyesol Greatcell solar and Sigma Aldrich. Moreover, for the electrical conductivity measurement, silver granulate (99.99%) from Umicore was thermally evaporated on top of the $C_{60}$ layer.

## 3.2 Fabrication process

Fabrication of transport layers and perovskite cesium mixed-cation lead mixed halide ($Cs_xFA_{1-x}PbI_{3-x}Br_x$) was done by the thermal evaporation process. Note that the fabrication and optimization of the perovskite layer were done by another member of our group. In this project, the optimization of the deposition process was mainly performed for $C_{60}$ deposition.

### 3.2.1 Thermal evaporation process

The technique applies a high vacuum, which lowers the sublimation temperature of the precursors used. By then heating the precursors to this sublimation temperature, the precursor can be evaporated and deposited onto the substrate. During the process, the current, voltage, ramp-up time, and substrate rotation will be carefully controlled during the deposition. The specific recipe for $C_{60}$ deposition was developed during this project according to the deposition profile of the $C_{60}$. The schematic representation of the $C_{60}$ thermal deposition process is shown in Figure 3.1

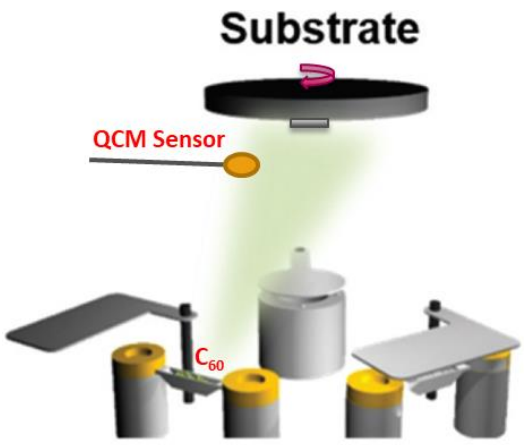


*Figure 3.1 Schematic illustration of thermal evaporation process for C60 ETL. Adapted from* [81]

To have precise control of the deposited film, the deposition rate and, consequently the thickness is continuously measured with the quartz crystal microbalance (QCM) sensor inside the evaporator. This sensor works based on the piezoelectric effect that occurs in crystalline materials of certain crystallography known as "acentric" materials.

Figure 3.2 shows the design of QCM with electrodes and how the amplitude varies over the range from the center location of the sensor. The QCM measures a mass variation per unit area by measuring the change in frequency of a quartz crystal resonator. The frequency change $(\Delta f)$ could be linearly related to its mass change $(\Delta m)$, as expressed by Sauerbrey [82]

$$\Delta m = -C * \frac{1}{n} * \Delta f \tag{3.1}$$

Where $n$ is the overtone number, and $C$ is a constant that depends on the property of the crystal used.

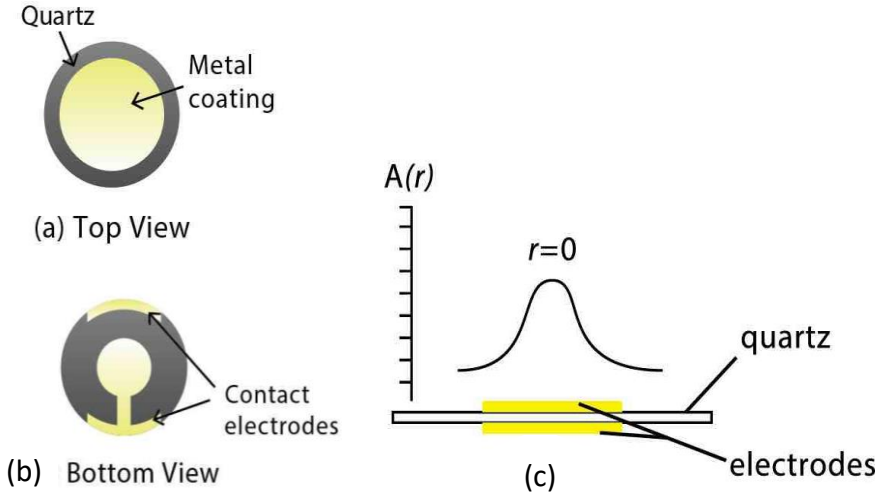


*Figure 3.2 Design of QCM with electrodes (yellow) and quartz crystal (grey); (a) top view (b) bottom view. (c) Schematic illustration of how the amplitude of vibration (A(r)) varies with the distance (r) from the center of the sensor* [82].

## 3.3

## 3.3 Material characterization

### 3.3.1 Structure and morphology characterization

#### *Atomic force microscopy*

Atomic force microscopy (AFM) is a non-interfering and non-contaminating scanning probe microscopy technique for surface topography characterization. In the AFM instrument, a tiny stylus (TESPA-V2) is moved up and down over a surface and measured as the deflection of a cantilever. The motion of the tip during a scan in each direction is monitored through a reflected laser beam.

The measurement of the samples was operated using tapping mode (non-contact mode). In this mode, the tip vibrates closely to the surface sample with a distance of a few nm. Furthermore, in the tapping mode, the feedback gain (integral gain) and the cantilever force (amplitude setpoint) need to be carefully adjusted to obtain an optimum figure. Too high feedback gain will increase the noise of the figure, but too low feedback gain also can show

parachuting effect, where the forward and reverse scan are not aligned. In addition, the amplitude setpoint indicates how big the force applied to the material also was adjusted to keep the distance between the surface and the tip. The data analysis and figure interpretation were then performed using NanoScope Analysis v1.90 software from Bruker.

## *Profilometry*

This project used a Veeco-Bruker Dektak 8 Stylus Profilometer with a stylus diameter of 12.5 µm to measure the layer thickness. The thin film samples were scratched away using a toothpick at three distinct locations (middle, left side, right side), revealing the quartz substrate underneath. The profilometry operates by applying a user-specified stylus force of 1 mg (specific force for an organic layer) in a straight line. The stylus's path is set to move over a portion of the sample containing both the exposed quartz and the thin film and the measured height difference and sample roughness. The measurement is taken a total of 3 times on each sample and averaged to provide a value of film thickness across the full surface. This measurement was conducted to get an initial thickness of the initial layer and validation of ellipsometry measurement thickness measurement.

## *Scanning electron microscopy*

To observe the microstructure of the thin films, scanning electron microscopy (SEM) was employed. A SEM uses a focused beam of electrons to create a magnified image of a sample (Figure 3.3). The electron beam is scanned in a regular pattern across the surface of the sample and detected to create the image on the screen.

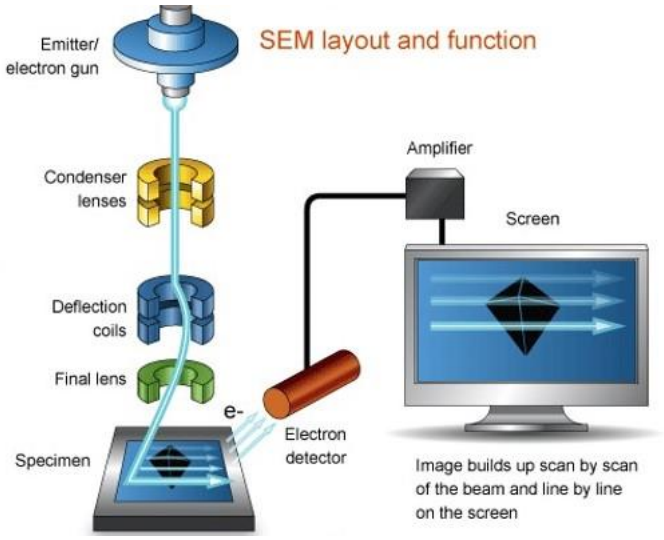


*Figure 3.3 Schematic illustration of Scanning Electron Microscopy* [83]

## *X-ray diffraction (XRD)*

The specific diffraction patterns of crystalline and semi-crystalline materials generate specific diffraction patterns and are scattered at various angles [84]. Bragg's law represents the scattering phenomena, where $n$ is an integer, $\lambda$ is the wavelength of the x-rays, $d$ is the spacing between planes in the atomic lattice of the sample, and $\theta$ is the diffraction angle in degrees.

$$n\lambda = 2d \sin\theta \tag{3.2}$$

Note that Bragg's Law covers two important things: (1) The smaller the distance d, the larger the diffraction of angle $\theta$, and (2) the bigger the wavelength $\lambda$, the larger the diffraction angle $\theta$.

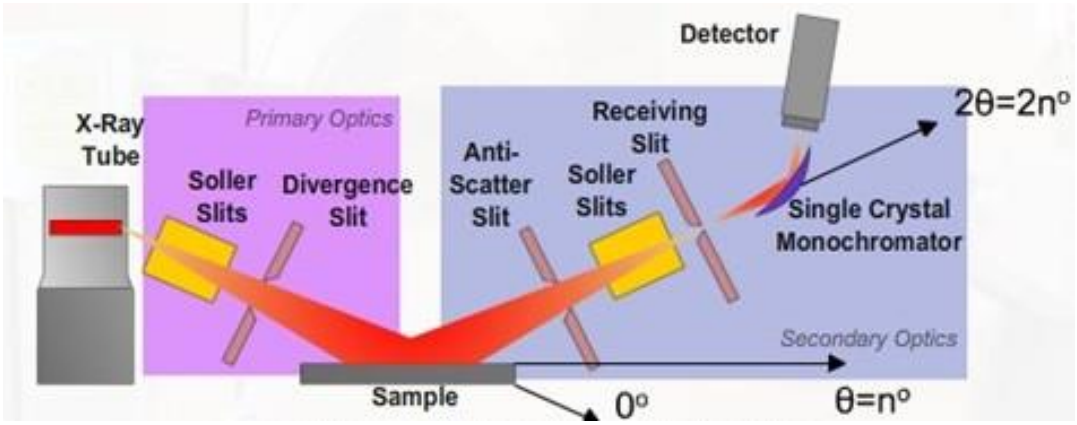


*Figure 3.4 Typical scheme of an XRD machine and its parts* [83]

By observing the angles where diffraction patterns occur, the distance d between the planes can be obtained. Then, the d-spacing is compared to the d-spacing of other known materials (database references), or the peaks are indexed and placed into a model to find the crystal structure of the materials [85]. The schematic of XRD is represented in Figure 3.4.

The grain size is also determined using the Scherrer equation:

$$D = \frac{K\lambda}{\beta \cos\theta} \tag{3.3}$$

Where $D$ is the crystallites size (nm), $K$ is a Scherrer constant (0.9), $\beta$ is full-width at half maximum (radian), and $\theta$ is peak position (radian)

### 3.3.2 **Optical characterization**

#### *Spectroscopic ellipsometry*

The schematic of the measurement procedure is shown in Figure 3.5. The first step is the measurement of the polarization change associated with a specific amplitude ratio (Psi, $\psi$) and phase difference (Delta, $\delta$). The measurement was performed using J.A. Woollam M-2000 DI Ellipsometer in the reflectance mode. Simultaneous fitting of the ellipsometry was done with J.A. Woollam CompleteEASE software to arrive at an optical constant for perovskite. An essential criterion for the created model is that it may not result in any unphysical shapes of the optical constants. Thus, it should follow the Kramers-Kronig relation, where the real part and imaginary part are interconnected, as it has been elaborated in Chapter 2. In this study, besides information on the thickness, ellipsometry was used to get an insight into the optical constants (n and k) of the transport layers ($MoO_x$ and $C_{60}$) and perovskite. The model was validated by comparing the thickness and roughness value of the model with the thickness and roughness calculated from the Dektak Profilometry measurement and AFM, respectively. In addition, the n and k data were further analyzed (step 4) in the modeling framework to obtain and compare the optical constant from experimental work and simulation.

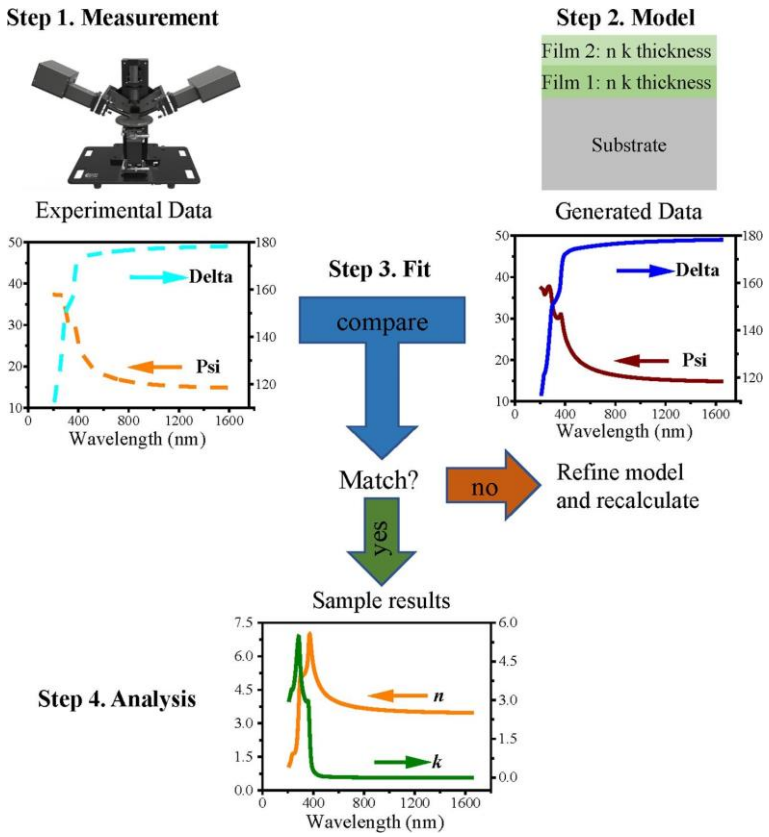


*Figure 3.5 Schematic procedure for ellipsometry data interpretation. Adapted from* [74]

## *UV-Vis-NIR Spectroscopy*

The measurements of absorbance and transmittance were observed using PerkinElmer LAMBDA 1050 UV/Vis/NIR Spectrophotometer with integrating sphere, deuterium, and tungsten-halogen lamps, and Peltier-cooled PbS and InGaAs detectors. The detector is located at the bottom of the integrating sphere, which collects light that enters the sphere. The schematic representation of the instrument is represented in Figure 3.6.

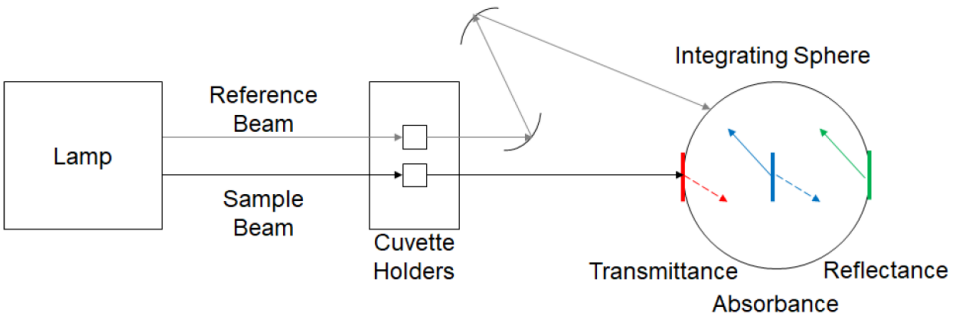


*Figure 3.6 A schematic illustration of UV-Vis-NIR Spectrophotometer. The solid and dashed arrows indicate reflected or transmitted light* [86].

The difference between the illumination intensity measured as a function of wavelength $I_0(\lambda)$ with the intensity measured by the spectrometer $I(\lambda)$ used to calculate the sample transmission:

$$T(\lambda) = \frac{I(\lambda)}{I_0(\lambda)} \tag{3.4}$$

and the absorbance of the film can be measured using the following equation

$$A(\lambda) = -\log\big(T(\lambda)\big) = -log_{10}\left(\frac{I(\lambda)}{I_0(\lambda)}\right) \tag{3.5}$$

Moreover, the Beer-Lambert law can also be utilized to determine the attenuation coefficient if the absorbance and thickness of the film $(x)$ are known.

$$\alpha.x = A \ln 10 \tag{3.6}$$

The attenuation coefficient allows for the creation of Tauc Plot, which helps to determine the type of electrical transition occurring, either it is direct or indirect, allowed or forbidden.

The Tauc plot describes $(\alpha(\lambda) * E_{photon}(\lambda))1/r$ on the ordinate and $E_{photon}(\lambda)$ on the abscissa, where the exponent $1/r$ determines the type of electronic transition occurring. On the Tauc plot with the correct exponent, there should be a linear regime, which can be extrapolated to the x-axis to get the band-gap of the material.

## 3.4 Optical GenPro4 simulation software

Optical simulations were performed using GenPro4 software developed by the PVMD group at TU Delft. GenPro4 is an optical model programmed in Matlab for solar cells that combines wave and ray-optics. GenPro4 represents the solar cell as a multilayer structure and calculates the fraction of incident light absorbed in each layer, taking into account the scattering and trapping of light at the interfaces [87]. From the process, the implied photocurrent is calculated from the area below the generated profile. Please note that the software is a purely optical model and does not put into consideration the electrical properties of the solar cells.

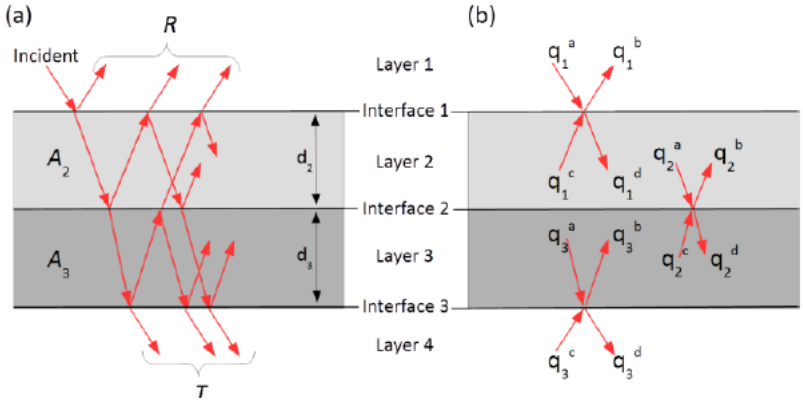


*Figure 3.7 Schematic representation of a multilayer structure with the numbering of the convention for layers and interfaces. a) optical paths contribute to R, T, A, and b) Net-radiation fluxes* [88].

Figure 3.7a shows the net-radiation method used in this software, where the solar cells are represented as a multilayer structure. The aim of the simulation is to determine the overall reflectance *R*, the transmittance *T,* and the absorptance of each layer *A*. Each layer is characterized by thickness ($d_i$) and complex refractive index ($N_i(\lambda)$), where λ is the wavelength (subscript *I* is used to indicate layer and interface numbers). When all interfaces are optically flat, the interface reflectances $r_i$ can be calculated from the Fresnel equation, and the corresponding interface transmittances are given by $t_i$ = 1- $r_i$. The *layer* transmittance $\tau_i$ can be calculated from the Beer-Lambert law. As indicated in Figure 3.7a, an incident photon can bounce between the interfaces multiple times and travel a complicated path. Therefore, to calculate *R*, *T* and *A from each layer, all* possible reflections

have to be taken into account. There are different mathematically equivalent methods to do this. The fluxes from each interface can be defined as $q_i^x$, where subscript *i* is the interface number and the superscript *x* ( = *a*, *b*, *c* or *d*) indicates whether the light is approaching/leaving the interface from the top/bottom. Each flux represents the net-radiation (in W/m$^2$) due to all possible photon paths

$$\begin{cases} q_i^a = \tau_i \,.\, q_i^d - 1 \\ q_i^b = r_i \,.\, q_i^a + t_i \,.\, q_i^c \\ q_i^c = t_{i+1} \,.\, q_{1+1}^b \\ q_i^d = t_i \,.\, q_i^a + r_i \,.\, q_i^c \end{cases} \tag{3.7}$$

From Eq. 44, the desired R, T, and $A_i$ can be obtained, which is represented in the equation below:

$$R = q_1^b \tag{3.8}$$

$$T = q_I^d \tag{3.9}$$

$$A = q_{i-1}^d - q_{i-1}^c + q_i^b - q_i^a \tag{3.10}$$

Note that GenPro4 automatically integrates R, T, and $A_i$ over the AM1.5 spectrum to calculate the corresponding implied photocurrents (in mA/cm$^2$).

# 4

# High-Quality $C_{60}$ Thin-Film

*This chapter gives a detailed illustration of processing, including the thermally evaporated $C_{60}$ thin layer results, deposition rate, and parameters control. In addition, the in-depth analysis on how to control the surface and obtain a high-quality $C_{60}$ single layer with different thickness and deposition rates is also thoroughly presented and discussed.*

## 4.1 Optimization of the deposition process

### 4.1.1 Deposition parameters

The consistency and stability of the deposition process are among the important factors to get a reliable and reproducible film. Thus, this project started by identifying the effect of the deposition parameters on the $C_{60}$ production method. The deposition profile was firstly investigated by creating the recipe and then converted into some procedures to establish a new program for the machine. This recipe consists of the applied current, substrate rotation, material density, applied voltage, and ramp-up time. In this process, the tooling factor and substrate rotation were kept constant at 120% and 10 revolutions per minute (RPM), respectively. Table 4.1 shows the summary of the optimal recipe corresponding to the targeted deposition rates. These parameters are used for the entire deposition process, i.e., thin-film characterization in the next subsection. It is worth noting that the pressure was kept at ultra-vacuum condition (< 2E-06 mbar) to reduce the probability of an evaporant atom colliding with gas molecule before reaching the substrate, i.e., to increase the mean free path.

*Table 4.1 Parameters of $C_{60}$ deposition with the different deposition rates*

| Deposition rate-target (Å/s) | Current (A) | Ramp-up time (s) | Vacuum pressure condition (mbar) |
|---|---|---|---|
| 1.0 | 33.0 – 33.5 | 480 | < 2E-06 |
| 0.5 | 31.5 - 32.0 | 420 | < 2E-06 |
| 0.3 | 30.0 - 31.0 | 360 | < 2E-06 |

The deposition process starts by putting the $C_{60}$ powder on the nitride boron crucible inside the evaporator chamber. The vacuum process takes around 15 - 25 minutes, and then the program is executed by ramping up the current to a specific value. Once the sublimation has started, the shutter will be manually opened. Once the desired thickness is achieved, the shutter is closed, and the ramp-down process begins automatically.

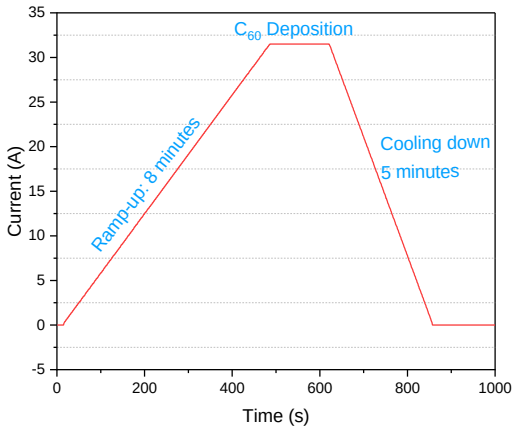


*Figure 4.1 Deposition process of $C_{60}$ with the deposition rate of 1 Å/s*

Based on the results of the detailed deposition data, the optimized deposition process and recipe were formulated. The schematic representation of the deposition process is illustrated in Figure 4.1, showing the typical diagram for the current variation as a function of the processing time for the deposition of $C_{60}$ (1 Å/s) for each individual step. Since the deposition rate will slightly decrease over time, the control of current is essential during the deposition process.

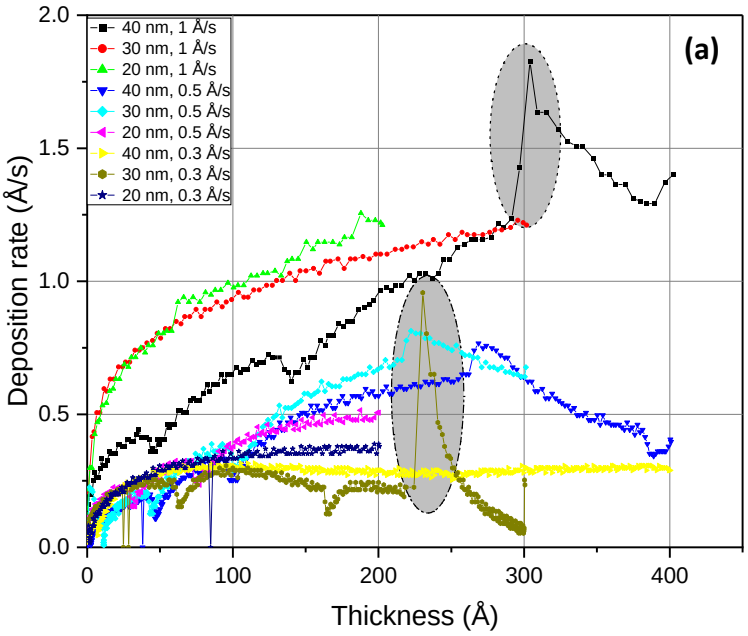

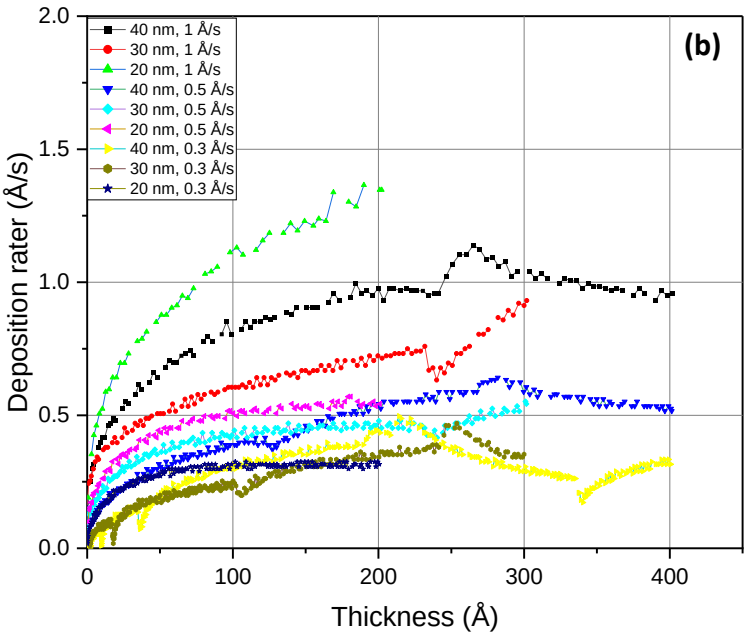


*Figure 4.2 The deposition rate profile vs. thickness (a) before optimization and (b) after optimization.*

Figure 4.2 indicates the deposition rate profile with the different thicknesses. It can be seen that there are a few deposition rates that are not steady during the deposition process, particularly at high deposition. Figure 4.2a exhibits that there are a few sudden peaks observed after attempting to change, increase/decrease the current. This fluctuation of deposition rate depends mainly on, type of boat, the current rate-driven to the boat, and the evaporated materials. Since the type of boat is similar for all the deposition processes, a possible reason for the sudden peak is that $C_{60}$ powders are organic molecules and have a low density; as such $C_{60}$ powders tend to spread quickly when excessive external thermal energy is applied during the deposition process. This phenomenon will contribute to the agglomeration of $C_{60}$ (Figure 4.3) on the surface and affects the non-uniformity of the thin film.

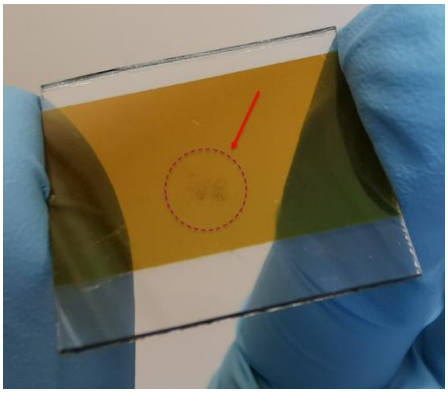

*Figure 4.3 Particles agglomeration due to rapid changes in deposition rate*

Figure 4.2b shows that the sudden peak of deposition rate is reduced significantly when the current is increased/reduced at a very slow rate (in the decimal value range). Therefore, the observable phenomenon is then being improved by the well-established recipe to get the high-quality $C_{60}$ thin film.

### 4.1.2 **Thickness and surface uniformity (geometrical aspect)**

Thickness is one of the crucial thin-film parameters since it largely determines the properties of a film [89]. Furthermore, it is also known that the non-uniformity of thickness can have a strong influence on the properties of the thin film. Areas that have non-uniformity can deliver misinterpretable data during the characterization of the thin film [90]. Thus, uniformity measurement is indispensable to be studied. In order to define the "good" or "bad" uniformity, there are two important parameters that were used in this study. One of the parameters is the standard deviation, which explains how to spread out a number is and it is mathematically expressed as:

$$STDEV = \sqrt{\frac{1}{N}\sum_{i=1}^{N}(x_i - \bar{x})^2} \tag{4.1}$$

where N is the total number of samples, $x_i$ is the value for each sample, and $\bar{x}$ is the mean value.

The next parameter is non-uniformity, which can be mathematically defined as:

$$Non - uniformity = \frac{(h_{max} - h_{min})}{2h_{avg}} \times 100\% \tag{4.2}$$

With $h_{max}$ and $h_{min}$ are the maximum and minimum measured thickness, respectively. $h_{avg}$ is the average thickness. This study aims to get the non-uniformity as low as possible and set the threshold to a maximum 10%, and the standard deviation is less than 2 nm.

In this specific part, the uniformity of the layer will be looked at from only the geometrical aspect and also the effect of the deposition rate toward the uniformity. The first investigation was done by checking the uniformity with respect to the position of the substrate inside the chamber. It is found out that substrate position in the sample holder plays a significant role in determining the uniformity. Figure 4.4 schematically represents the resulted thickness non-uniformity according to the sample position inside the chamber. The first measurement was performed with the series order from right to left, and it shows that there is a huge thickness difference in the middle part indicated by dark orange-ish. The thickness measurement was done using profilometry and confirmed with ellipsometry with three different spots in the sample surface, as it is shown in Figure 4.4b, where L, M, and R represent left, middle, and right, respectively.

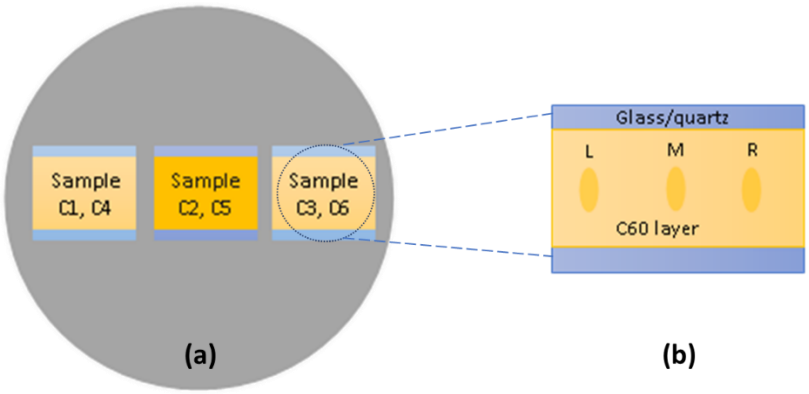


*Figure 4.4 The illustration of (a) thickness non-uniformity with respect to the sample positioning inside the chamber (b) different location of measurement.*

Table 4.2 shows the difference between targeted thickness and actual thickness, where the middle part shows a high number compared to other sample positions.

*Table 4.2 Thickness non-uniformity. The sample names refer to the substrate position shown in Fig.4.4a.*

| Sample | Target thickness (nm) | L (nm) | M (nm) | R (nm) | Average thickness (nm) |
|---|---|---|---|---|---|
| C1 | 80 | 78 | 72 | 71 | 73.67 |
| C2 | | 105 | 99 | 103 | 102.33 |
| C3 | | 84 | 75 | 78 | 79.00 |
| C4 | 25 | 25 | 25 | 30 | 26.67 |
| C5 | | 35 | 36 | 38 | 36.33 |
| C6 | | 25 | 26 | 22 | 24.33 |

The thickness distribution can be understood from the Langmuir-Knudsen relation that describes the mass deposition rate per unit area ($R_m$) of source surface as:

$$R_m = C\left(\frac{M}{T}\right)^{\frac{1}{2}} cos\theta\ cos\varphi\ \frac{1}{r^2}(P_e(T) - P) \tag{4.3}$$

where $C = 1.85\,x\,102$, $M$ is the evaporant molecular mass (g), $r$ is the source-substrate distance (cm), $T$ is source temperature (K), $P_e$ is evaporant vapor pressure (*Pa*), and $P$ is the chamber pressure (Pa). This relation can also be used to determine non-uniformity during film deposition. If we just assume that other parameters are kept constant, such as pressure ($P$), temperature ($T$), and mass of the evaporant ($M$), then the equation becomes angle- and distance-dependent. To give a clear illustration, Figure 4.5 schematically represents the parameters involved inside the thermal evaporation chamber, where $W/2$ is the total distance between two samples.

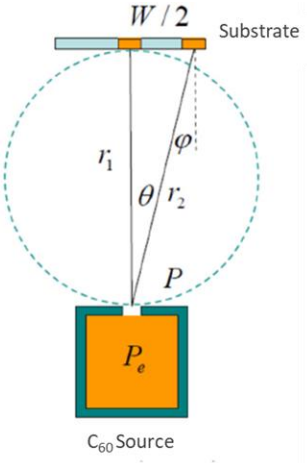


*Figure 4.5 Schematic representation of deposition parameters with flat substrate inside the thermal evaporation chamber*

The deposition rate difference between the middle part and edge can be rewritten as:

$$R_1 \propto \frac{1}{{r_1}^2} \tag{4.4}$$

$$R_2 \propto \frac{1}{{r_2}^2} cos^2\theta = \frac{{r_1}^2}{{r_2}^4} \tag{4.5}$$

This difference in deposition rate affects the amount of $C_{60}$ deposited on top of the substrate and eventually produces non-uniformity in thickness. The relation between uniformity $\sigma$ and deposition rate can be derived as:

$$\sigma(\%) = \frac{R_1 - R_2}{R_1}(\%) \tag{4.6}$$

And from the illustration in Figure 4.5 combining with Eq. (4.4) – Eq. (4.6)

$$\sigma = 1 - \left(1 + \left(\frac{W}{2r_1}\right)^2\right)^{-2} \approx \frac{W^2}{2{r_1}^2} \quad or \quad \frac{W}{r_1} = \sqrt{2\sigma} \tag{4.7}$$

The source-substrate distance requires $r > \frac{W}{\sqrt{2\sigma}}$ to get optimum uniformity [91]. In practice, it is typical to double the number to give some process margin. However, large *r* means a bigger chamber is required, higher capacity of vacuum pump, lower deposition rate, and higher evaporant waste. Thus, besides increasing *r*, there are also a few simple methods for improving uniformity, such as increase substrate rotation, use smaller substrate, a circular or spherical sample holder, or positioning the specimen around the circle. In this project, the samples are positioned with a 4-fold symmetrical position to ensure the source-substrate distance is similar and thus a steady deposition rate.
In addition, thickness uniformity for each substrate with a different deposition rate was also performed. Spectroscopy ellipsometry was used to measure the thickness from 15 different spots of the layer.

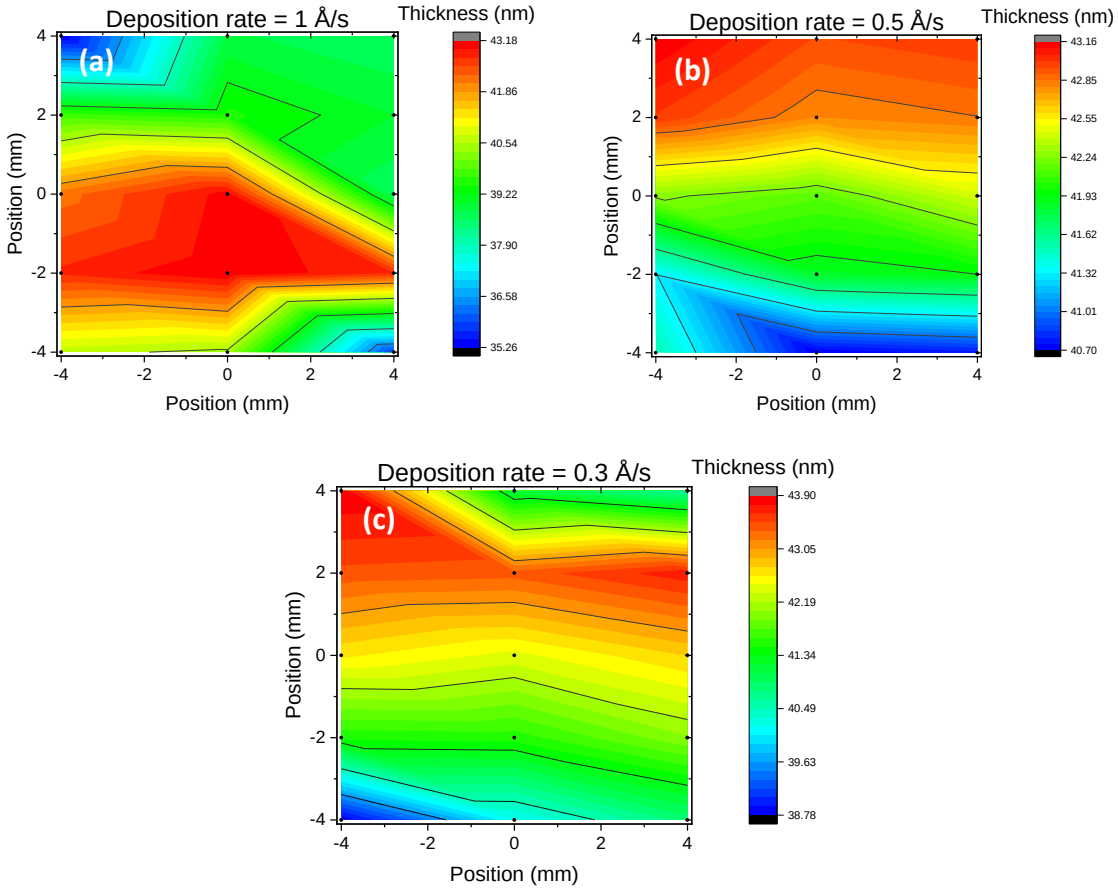


*Figure 4.6 Thickness uniformity of each layer with the different deposition rate, a) 1 Å/s, b) 0.5 Å/s, and c) 0.3 Å/s.*

The measured thicknesses are transferred to deposition rate and two-dimensional (2D) contour plots (Figure 4.6) to give a more detailed view of the uniformity of the layer. Black dots represent the measured points.

Non-uniformity shows very good results where all the samples with different deposition rates reveal non-uniformity less than 10%. From the figure, it can be seen that at the edge part of the substrate, the layer is thinner than the middle part. Most likely, the so-called 'edge effect' plays a role here, where there is a shadowing during the deposition process. However, these differences are still acceptable since the deviation is very low, less than 2 nm. This part will not affect that much in the device fabrication since the active areas for the final design are concentrated in the middle part, as indicated in our masks in Appendix A.1. Table 4.3 summarizes the resulted average thickness, standard deviation, and non-uniformity with the different deposition rates.

*Table 4.3 Layer uniformity with the different deposition rates*

| | 0.3 Å/s | 0.5 Å/s | 1 Å/s |
|---|---|---|---|
| Average thickness (nm) | 41.93 | 42.18 | 40.03 |
| STDEV (nm) | 1.41 | 0.79 | 2.40 |
| Non-uniformity (%) | 5.87 | 2.92 | 9.87 |

To sum up this subsection, the deposition process and parameters in the thermal evaporation method have been optimized. The resulted recipes can produce very good surface uniformity and homogeneity.

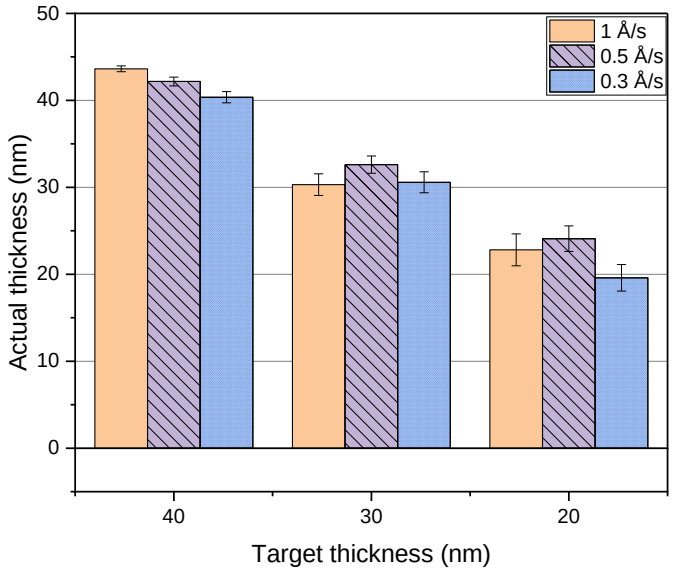


*Figure 4.7 Comparison of target thickness vs. actual thickness with the different deposition rates.*

Figure 4.7 shows the comparison between targeted thickness and actual thickness with the different deposition rates. The resulted thickness is in good agreement with the target thickness, with a margin of error < 2 nm. After obtaining this homogeneous thin film, the following sections focus on an in-depth analysis of thin-film quality from optical properties, crystallinity, electrical behavior, and surface morphology.

## 4.2 Study of thin-film quality: effect of thickness and deposition rate

It is well known that device performance depends crucially on the structure and morphology of the structure [52]. Thus, having deep knowledge of morphology and growth dynamics is essential from a technological and fundamental perspective. This section focuses on discussing the effect of the deposition rate and thickness towards the quality of the $C_{60}$ thin film based on morphological, crystal structure, electrical properties measurement, and optical properties observation.

### 4.2.1 Surface roughness and morphology

In order to study the effect of the deposition rate towards the optical and electrical properties of the $C_{60}$ single layer, the crystal growth and morphology of the samples are first examined by means of the AFM and SEM techniques.

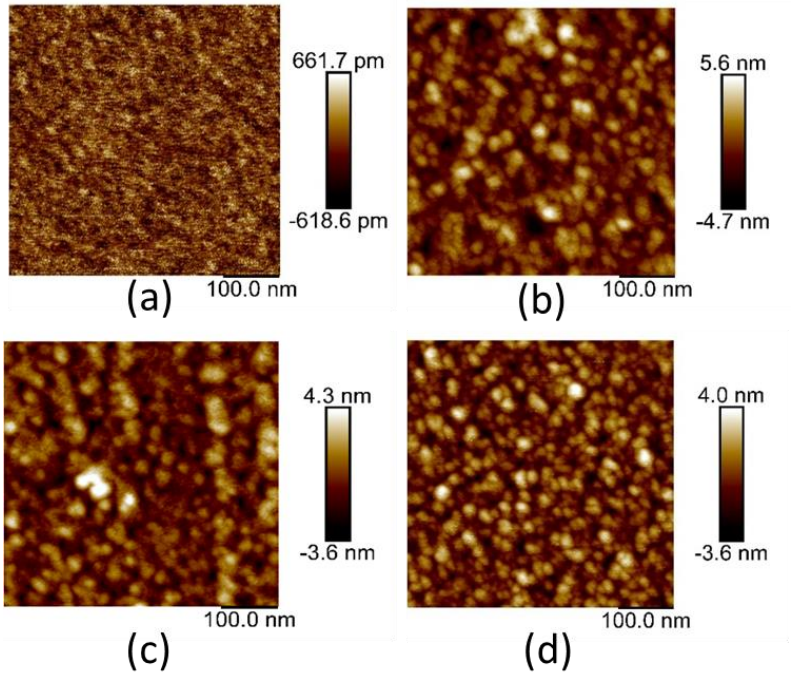


*Figure 4.8 AFM images of (a) bare silicon wafer (crystallographic orientation (100)) substrate and C60 layer with 0.5 Å/s of deposition rate with the thickness of (b) 20 nm, (c) 30 nm, and (d) 40 nm.*

Figure 4.8 represents the AFM images of Si wafer substrate and $C_{60}$ layers with different thicknesses. Note that the substrate primarily influences the deposited layer's crystalline orientation, grain growth, and surface morphology. Thus, a Si wafer (100) was used as a substrate in this experiment. Figure 4.8a indicates the morphology of Si wafer substrate is exceptionally smooth with roughness RMS of 0.187 nm. In addition, Figure 4.8b and c show the AFM images of deposited 20 and 30 nm thick $C_{60}$, respectively. The surfaces exhibit a rough morphology, with crescent grain and even formation of a large particle clustering. On the other hand, Figure 4.8d represents 40 nm thick $C_{60}$ with a uniform than that made at thinner layer. For photovoltaic applications, this uniform and conformal coverage are useful to prevent the direct contact between the perovskite absorber layer and the metal contact. The effect of deposition rate in accordance with the surface morphology was also observed. Figure 4.9 shows the 2D and 3D morphology of the 40 nm thick $C_{60}$ layer with different deposition rates.

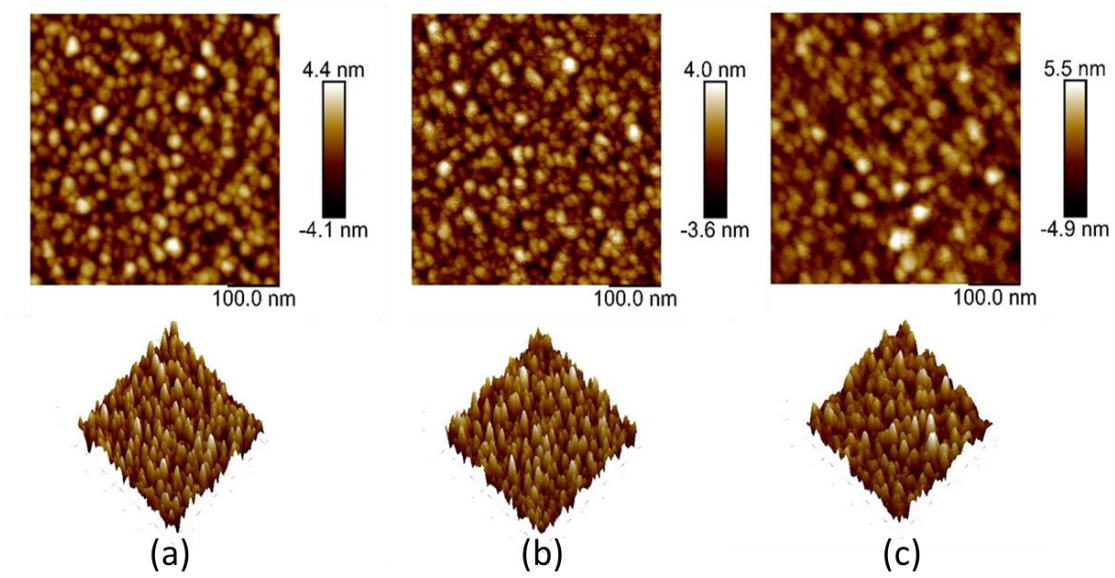


*Figure 4.9 AFM images of 40 nm $C_{60}$ layer with (a) 0.3 Å/s, (b) 0.5 Å/s, and (c) 1 Å/s of deposition rate*

Figure 4.9a and b show the $C_{60}$ film deposited with 0.3 and 0.5 Å/s, respectively. Both figures indicate relatively similar morphology, with maximum roughness indicated by ~ 4 nm. On the other hand, the 1 Å/s deposition rate (see Figure 4.9c) shows some non-uniform of grain size and rougher surface, and the maximum roughness is ~ 5.5 nm. The variation of deposition rate indicates an increase of roughness with deposition rate. The detailed data of the effect of thickness and deposition rate are summarized in Table 4.4. The data are averaged from three different points measured on each sample.

*Table 4.4 AFM roughness measurement of $C_{60}$ for different thicknesses and deposition rates with a scan length of 500 nm.*

| Deposition rate (Å/s) | Thickness (nm) | RMS (nm) | Average roughness (nm) | Roughness maximum (nm) | Standard deviation | Surface area difference (%) |
|---|---|---|---|---|---|---|
| **1** | 40 | 2.26 | 1.81 | 14.90 | 2.26 | 4.21 |
| | 30 | 1.39 | 1.11 | 10.80 | 1.39 | 3.06 |
| | 20 | 1.26 | 0.99 | 10.70 | 1.26 | 2.98 |
| **0.5** | 40 | 1.59 | 1.27 | 12 | 1.59 | 3.01 |
| | 30 | 1.13 | 0.89 | 9.11 | 1.13 | 2.44 |
| | 20 | 1.42 | 1.11 | 10.41 | 1.42 | 1.42 |
| **0.3** | 40 | 1.33 | 1.05 | 9.90 | 1.33 | 3.04 |
| | 30 | 1.33 | 1.03 | 11.11 | 1.33 | 3.12 |
| | 20 | 1.27 | 0.99 | 11.43 | 1.27 | 2.25 |

SEM observations were also performed to check the morphology of $C_{60}$ film with different deposition rates. Figure 4.10 indicates that the results concurrent with the AFM images where 0.3 and 0.5 Å/s show smooth surface and regular grains, but 1 Å/s shows particles agglomeration, $C_{60}$ clustering, and non-uniform grain size, indicated by the red arrows in Figure 4.10c. This can be understood because, in the low deposition rate or long deposition time, some adsorptions atoms have enough time to migrate to sites where the surface energy is low enough to be covered by the coming atom. As a result, the atoms can conformally cover the entire surface. In contrast, the diffusion of atoms to the lowest surface energy will be hampered at a high deposition rate due to high kinetic energy.

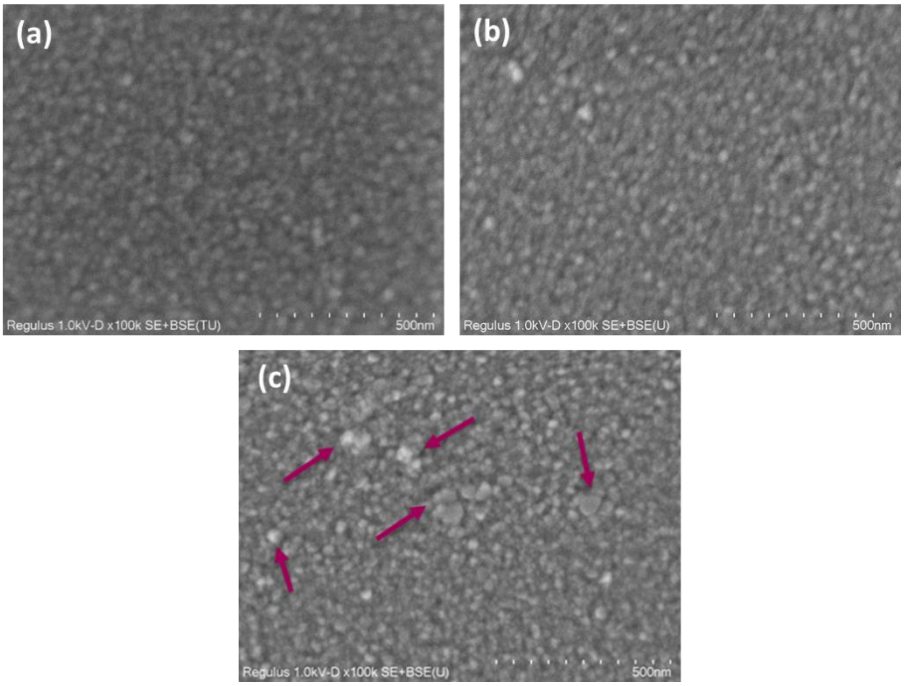


*Figure 4.10 SEM images of $C_{60}$ films fabricated with, a) 0.3, b) 0.5, and c) 1 Å/s*

Also, compared to the morphological properties of $C_{60}$ thin films produced by thermal evaporation under argon gas, reported previously by Zhang et al. [92], this study shows SEM images provide relatively smooth and flat for the thin film grown in vacuum conditions.

### 4.2.2 **Layer crystallinity**

Small molecule organic semiconductors like $C_{60}$ constitute versatile building blocks that allow the controlled growth of pure films using the thermal evaporation method, which then enables us to derive a detailed understanding of the structure-properties relationship. It has been reported that the degree of crystallinity and the domain size of organic semiconductors typically increases with processing temperature [93]. In particular, the crystalline films of $C_{60}$ are only formed upon growth at elevated temperatures. Here, however, the effect of thickness and deposition rate towards the crystallinity layer are investigated. This study uses the XRD technique to justify the selected thickness and deposition rate further and observe the crystallinity of each layer. For this purpose, n-doped Si wafers (100) were used as a substrate to avoid the large amorphous background scattering in the XRD pattern.

It has been reported that for the photovoltaics application where a large area is required, obtaining coverage of a crystalline film can prove to be difficult but has been shown to have considerable benefits with regard to the exciton diffusion length, charge carrier mobility, and further increase the charge collection [94] [95]. Moreover, the grain boundaries need to be minimized and uniform as they can be sources of non-radiative recombination and are detrimental to the device's performance.

The X-ray diffraction pattern was firstly investigated for $C_{60}$ powder used for the thermal evaporation to get reference peaks before the thermal deposition process Figure 4.11. It shows that $C_{60}$ in powder form is crystalline, where the peaks are shown by (111), (220), (311), (222), (331), and (420). The low angle asymmetric broadening of the $2\theta = 12.5^{o}$ is most probably due to the existence of planar defects [76].

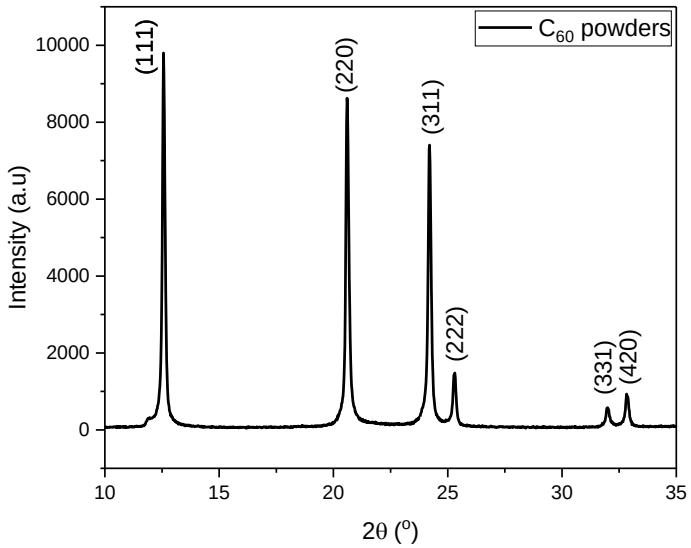


*Figure 4.11 XRD pattern of $C_{60}$ powder in Co-$K_\alpha$ radiation.*

Note that XRD peaks are the signature of the material. However, the structure of powders can be different from the thin film due to several reasons such as (i) unique direction of film deposition, (ii) adhesion of the film to the substrate, and (iii) thermodynamically unstable deposition conditions [96]. Since $C_{60}$ film is deposited on an extremely flat silicon substrate, the growth will be perpendicular to the substrate surface with the mutual competition of neighboring grains. The growing grains are fixed to the substrate, and after cooling the system to room temperature, residual stresses are created due to different thermal contractions of the film and the substrate. Additionally, intrinsic stresses can occur as a consequence of structure defects introduced into the film during its growth. Taken together, one can expect the structure of polycrystalline thin films will be strongly distorted with preferential grain orientation in the growth direction [96]. Figure 4.12 exhibits the XRD pattern for the $C_{60}$ films with different thicknesses deposited at a rate of 0.5 Å/s.

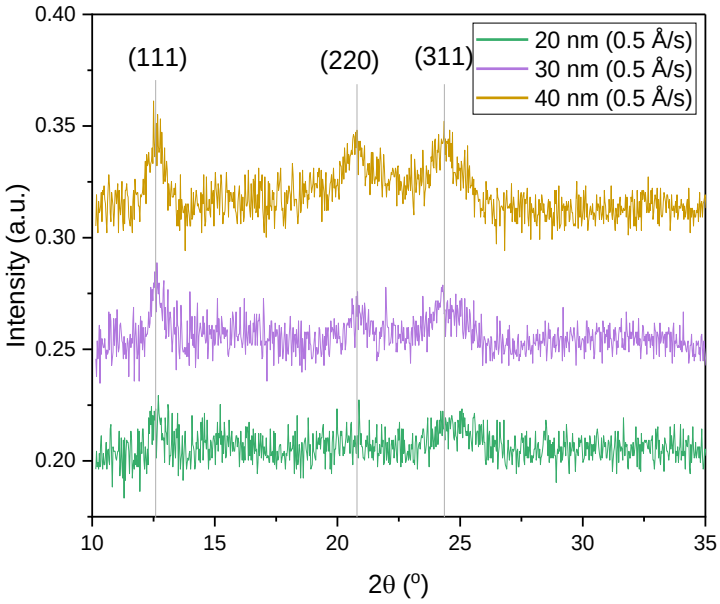


*Figure 4.12 XRD pattern of C60 layer with different thickness at 0.5 Å/s deposition rate.*

Although X-ray peaks for $C_{60}$ film are significantly low than $C_{60}$ powder (see Figure 4.11), we can still observe a few peaks at 12.5, 20.8, 24.1 degrees ($2\theta$ angle) which are respectively indexed as the (111), (220), and (311). These diffraction peaks and miller indices are associated with the FCC crystal structure [76]. It is known that the primary intermolecular interaction between $C_{60}$ molecules is van der Waals force [97]. Due to the quasi-spherical shape of individual $C_{60}$ molecules, the $C_{60}$ crystal is orientationally disordered. Each molecule can rotate freely around its equilibrium position. Therefore, the growth of $C_{60}$ crystal is dependent on the intermolecular interactions of $C_{60}$ molecules. When crystals grow bigger and meet each other, the neighboring crystal's orientation will be affected since the interaction between the nucleated crystal and the substrate is much weaker than that between the crystals themselves [97]. As we can see in the XRD pattern of $C_{60}$ (Figure 4.12), the (111) plane shows the strongest peak. This is because a shorter $C_{60}$-$C_{60}$ distance in the (111) plane (closed packed) allows stronger van der Walls interactions, resulting in a greater growth rate in (111) orientation [98]. The thicker $C_{60}$ layer (40 nm) shows a high and sharp peak of the crystalline phase. The purple line corresponding to the 30-nm-thick layer shows a weak crystalline phase. On the other hand, at 20 nm thick, $C_{60}$ with a similar deposition rate shows very low crystalline peaks, and the peak of (220) is missing. The missing peak indicates that 20 nm of $C_{60}$ crystal growth is probably too thin to accommodate the crystal growth by $C_{60}$-$C_{60}$ interaction in the preferred orientation. Therefore, molecules do not reside in an energetically stable position (state).

Figure 4.13 shows the XRD pattern of 40 nm $C_{60}$ thickness with different deposition rates, namely 0.3, 0.5, and 1 Å/s. The results show a similar peak position for different deposition rates. However, their peaks broaden with increasing the deposition rate up to 1 Å/s, especially for the peaks with a $2\theta$ angle in the range of 20 – 25 degrees. This observation indicates the presence of lattice defects inside the crystal structure, small grain size, and non-uniformity of grain size that it might be due to some $C_{60}$ clusters observed on the surface (see Figure 4.10).

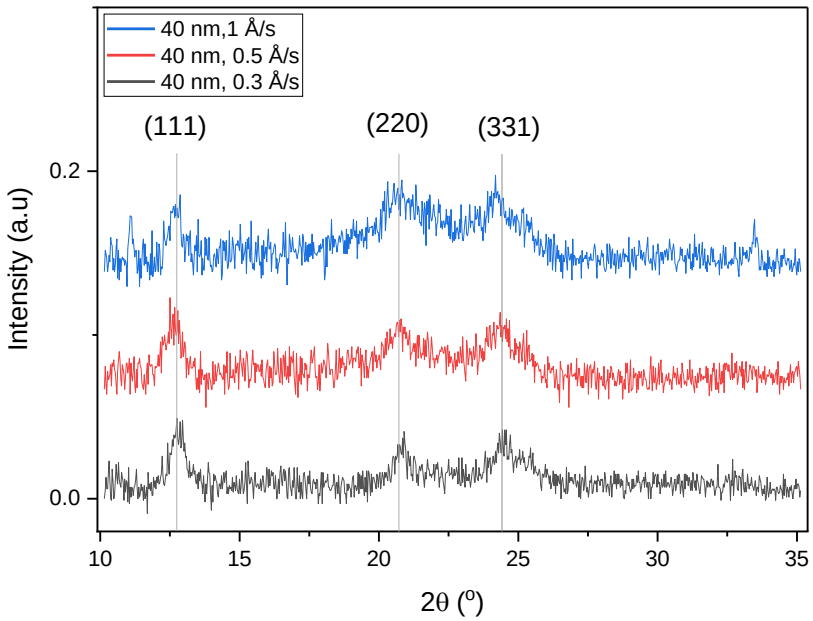


*Figure 4.13 XRD pattern of C60 layer with (a) different thickness at 0.5 Å/s deposition rate and (b) 40nm thickness with a different deposition rate.*

From XRD measurement, it is fair to say that increasing the thickness from 20 nm to 40 nm increases the peak and crystallinity phase. Furthermore, the deposition rate shows no significant effect on the crystallinity of $C_{60}$ except for 1 Å/s of deposition rate exhibit broadening effect that might indicate small grain size and the presence of a defect in the structure of $C_{60}$.

## 4.3 Analysis of optical properties

### 4.3.1 Optical constant

For the optical constants (n and k) identification of $C_{60}$ layer, there are few oscillator models that have been previously introduced in literature [76], [99]. In many ellipsometry studies, a classical oscillator (CL), Fouruhi and Bloomer (FB), and Tauc Lorentz (TL) have been successfully applied for modeling $C_{60}$ thin films and extracting the optical energy transitions [73], [76], [78], [80]. The summary of these three different approaches is well-summarized in by Datta et al. in Figure 4.14.

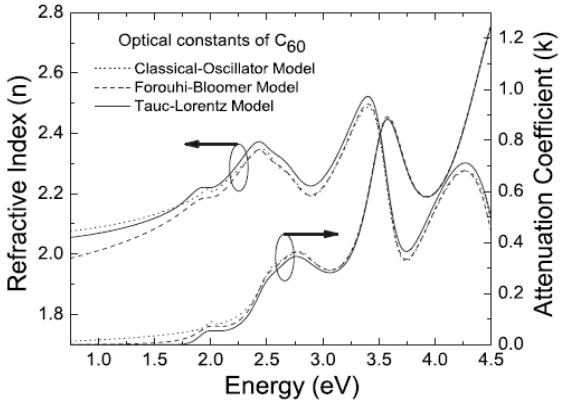


*Figure 4.14 Optical constants of $C_{60}$ from three different dielectric functions* [76].

As it is shown in Figure 4.14, both CL and FB models show limitations where nonzero absorption below the band edge and fundamental inconsistencies in satisfying the Kramers-Kronig relation [76]. In contrast, the TL dielectric model can perfectly capture the band edge, exhibit optical bandgap and low excitation energy extraction from direct ellipsometry measurement. In addition, as it has been addressed in Chapter 2, this dispersion relation follows Kramers-Kronig consistency and is derived using the Tauc joint density of states above the band edge.

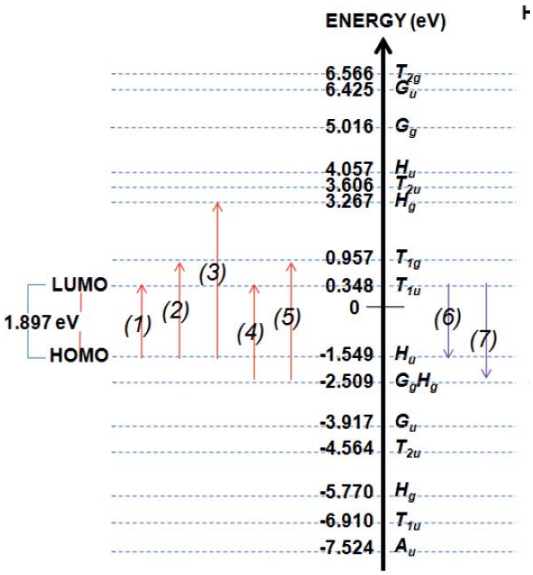


*Figure 4.15 Schematic of the electronic structure of $C_{60}$ molecule calculated by the Huckel model* [100].

Since all oscillator models require prior knowledge about the film or its interaction with light, it is therefore not always possible to apply this model accurately and put the parameters without collecting this information beforehand. Particularly for $C_{60}$, it has been reported that the presence of three to six oscillators corresponds to the optical transitions [30], [76]. In some cases, it resulted in different energy gap values between experimental and theoretical. For example, according to the Huckel model and calculation of the electronic structure of $C_{60}$ molecule, five possible excitation transitions existed (Figure 4.15), where (1) to (5) represent electronic excitation of $H_u \rightarrow T_{1u}$, $H_u \rightarrow T_{1g}$, $H_u \rightarrow H_g$, $H_g \rightarrow T_{1u}$, and $H_g \rightarrow T_{1u}$ and (6) to (7) indicate emission transitions. The highest occupied molecular orbital (HOMO) and the lowest unoccupied molecular orbital (LUMO) are indicated by $H_u$ and $T_{1u}$. On the other hand, a study by Ren et al. reported that four oscillators are to obtain the optical constant of $C_{60}$ [99] and three oscillators reported by Zhang et al. [92]. The reported literature indicates that the oscillator for $C_{60}$ might depend on the processing method and the structure of $C_{60}$ (thin film, molecule, or bulky). We tried to follow the procedure from the literature by varying the Tauc-Lorentz model with 3 to 6 oscillators. However, perfect-fitting (measured $\psi$ and $\Delta$ vs. model) still shows high mean squared error (MSE) due to under-estimation in some parts, particularly in the low energy range. Therefore, the approach in this project is to obtain purely mathematical relations and perfect fitting by means of B-splines. This model sums the individual basis function of the multiple polynomials to construct the final curve. As such, the fitting will follow each pattern in the measured sample and produce a very smooth curve. The resulting fitting is then parameterized with the Tauc Lorentz dispersion model to obtain the Kramers-Kronig consistency of dielectric function and to arrive at a physics-based approach.

Figure 4.16 shows the ellipsometry fitting of measured ψ and Δ using a combination of B-spline model for a 40-nm-thick $C_{60}$ film. The plotted model (dashed line) follows the measured sample (solid lines) is in good agreement, with a mean squared error (MSE) of 6.27. In order to improve the accuracy of optical constants obtained from this least-squares procedure, the measurement varied the incident angle of 70, 65, 60, and 55 degrees and analyzed them in a similar method. The angles for $\psi$ are indicated by a solid red line and measured from top to bottom (70 - 55º). On the other hand, solid green lines represent $\Delta$, and the angles from top to bottom (55 - 70º).

Furthermore, the structural bilayer was used during the modeling, whereas the bottom part was the quartz substrate which the optical constant has been previously measured using the Cauchy model. Remember that Cauchy mode assumes that there is no absorption for the entire spectral wavelength, $k = 0$. To avoid backside reflection, the translucent scotch tape was attached to the rear side of quartz.

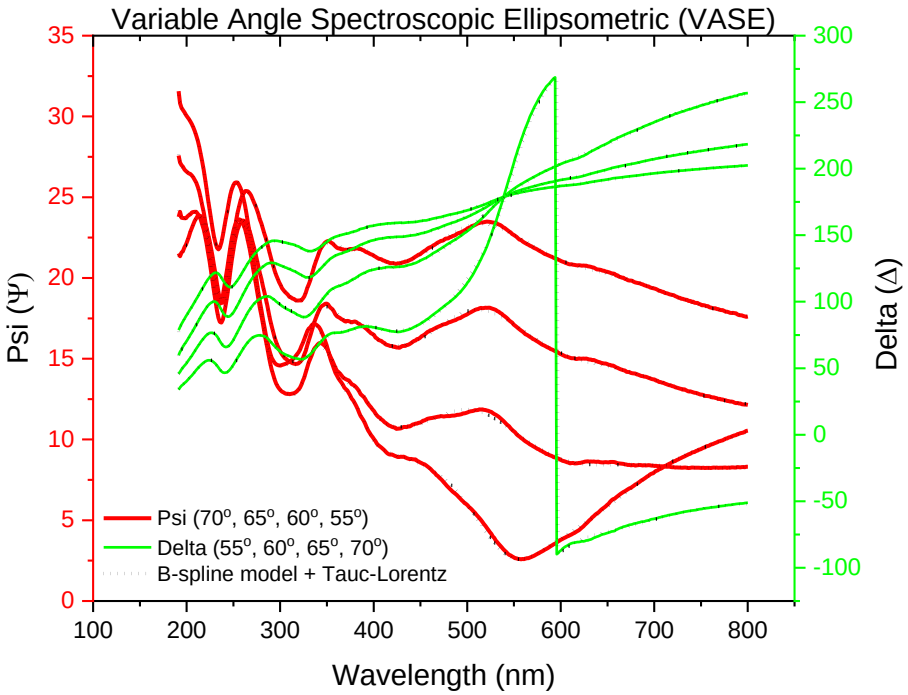


*Figure 4.16 Simulated (dashed line) and measured (line) of ψ and Δ from multi-angle spectroscopic ellipsometry.*

The fitting results of the imaginary part $\varepsilon_2$ of dielectric function are represented in Figure 4.17. The gray curves reveal the individual contribution from the Tauc-Lorentz oscillator to $\varepsilon_2$ model and the solid green line is the B-spline fitting of $C_{60}$.

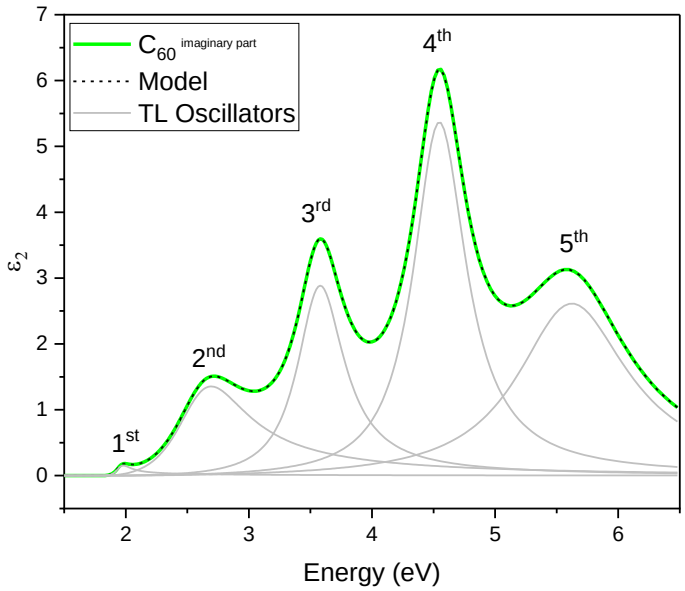


*Figure 4.17 Imaginary part of dielectric function and number of TL oscillators.*

It is important to recall the Tauc-Lorentz dispersion model in Eq. (2.28), with three fitting parameters; *A* is the strength of the $\varepsilon_2$ peak (amplitude), *C* is the broadening term of the peak, and *E* is the peak central energy. Table 4.5 collects the extracted fitting parameters related to the optical transitions from the Tauc-Lorentz model. This study found that five oscillators are required to minimize the MSE of the fit and reproduce the data accurately. Note that these parameters are extracted from a $C_{60}$ layer with a thickness of 40 nm and fabricated in 0.5 Å/s of deposition rate. These parameters will slightly change with different thicknesses and deposition rates. However, the number of TL oscillators for all layers observed in this study is the same.

*Table 4.5 Fitting parameters of the Tauc-Lorentz for the five oscillators*

| Oscillator | $A_i$ (eV) | C (eV) | Centre (eV) |
|---|---|---|---|
| $E_1$ | 3.157 ± 1.087 | 0.137 ± 0.008 | 1.953 ± 0.008 |
| $E_2$ | 9.452 ± 0.479 | 0.704 ± 0.007 | 2.617 ± 0.004 |
| $E_3$ | 5.460 ± 0.112 | 0.463 ± 0.006 | 3.572 ± 0.002 |
| $E_4$ | 7.691 ± 0.132 | 0.520 ± 0.006 | 4.545 ± 0.002 |
| $E_5$ | 6.213 ± 0.069 | 1.096 ± 0.008 | 5.625 ± 0.002 |

Moreover, it is also found that for the amplitude at lower energies, the accuracies of the parameters are lower compared to transitions at higher energies, due to the subdued feature of the low energy transitions, where the fitting attempts to neglect the low energy transitions and gives poor-fitting [76].

Figure 4.18 shows the optical constants (n and k) of $C_{60}$ extracted using the Tauc-Lorentz model. Comparing the extracted n,k data to literature, we observe similar peak positions to the one reported by Detta et al. in Figure 4.14 [76].

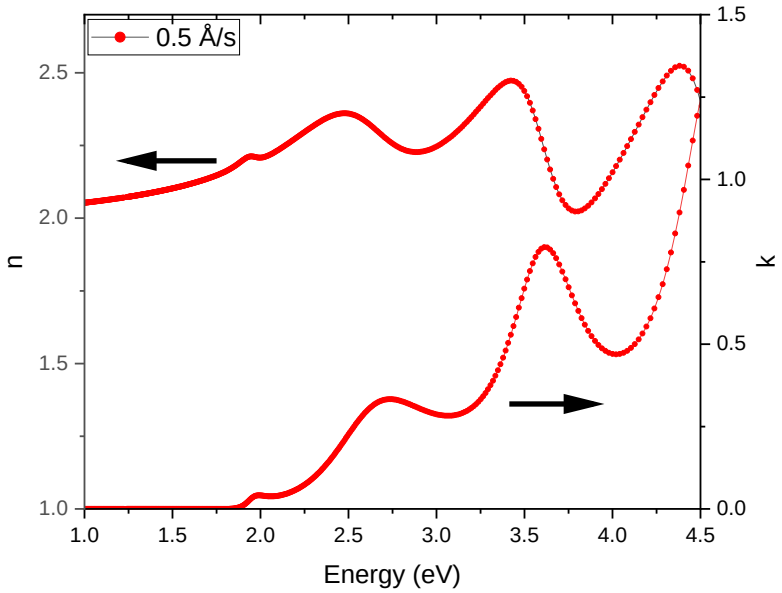


*Figure 4.18 Optical constant of $C_{60}$ extracted from ellipsometry using B-spline and Tauc-Lorentz oscillator model.*

The validation of the ellipsometry model is performed by comparing the absorptance value from UV Vis spectrophotometry measurement and the ellipsometry model. Both absorptance curves are plotted in Figure 4.19. Both figures show good matching and similar peak

positions at the given energy range. The identification of optical bandgap energy as an important parameter can be observed from attenuation coefficient (k) spectra below 2.0 eV. Generally, the optical bandgap can be determined by a linear extrapolation of the Tauc's plot obtained from absorption spectra (see Section 3.3.2). This calculation, however, can extract overestimated values [99]. Since the k value is related to the absorption coefficient of the layer, as it has been described in Eq. (2.21), by using a suitable dielectric model, the bandgap can also be directly obtained as the output of the fitting procedure in SE measurement. In this study, the bandgap from SE is calculated to be 1.81 eV. Meanwhile, the bandgap value from UV Vis spectrophotometry is 1.82 eV.

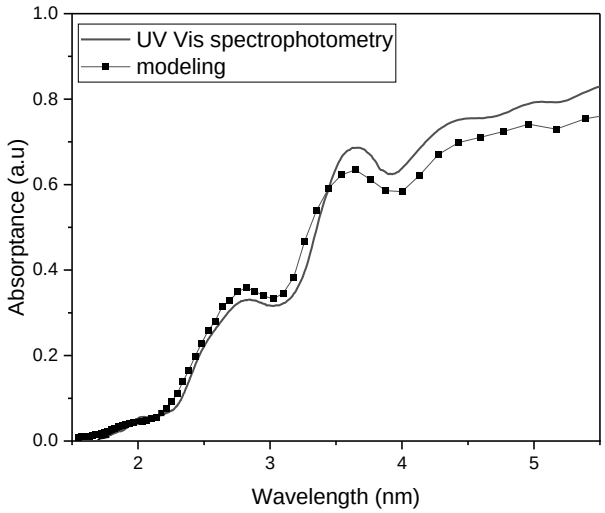


*Figure 4.19 Comparison of absorbance data from experimental (line) versus simulated (dashed line).*

These results indicate that a combination of B-spline and Tauc-Lorentz can provide reliable optical constant and dielectric function for accurately modeling $C_{60}$ film from the thermal evaporation process.

### 4.3.2 **Effect of thickness and deposition rate**

The effect of deposition rate and thickness toward the optical constant of $C_{60}$ is further examined. In Figure 4.20a, both refractive index (n) and extinction coefficient (k) curve for 1 Å/s show slightly high than other deposition rates. This difference might be ascribed to the lower non-uniform grain size and defects observed for the $C_{60}$ layer deposited at 1 Å/s, which is revealed in the SEM and XRD observations [101]. This non-uniformity can create irregular internal scattering and might be responsible for the increased absorption coefficient as well as the n and k value.

Figure 4.20b shows the spectral variation of the refractive index and extinction coefficient as a function of energy for different layer thicknesses. The refractive index decreases when the thickness is decreased. As the refractive index is determined by how much the path of light is bent or refracted when entering a material, different densities and surface morphology can contribute to the change in the refractive index [102]. This might suggest that the thinner $C_{60}$ film is less compact than thicker ones. In addition, the imaginary part k depends on the crystalline structure of the solid material. This is because the behavior of waves within the crystalline materials (solid matter) is scattered between the crystalline phase or particle size of the material [103]. Thus, the waves will be a random scattering inside the grain boundaries of the film. This might explain why the k value for 20 nm of thickness exhibits the

highest value. Previously, it has been indicated that the peak of 20 nm thick $C_{60}$ is low, and there is some crystalline phase that disappears (see Figure 4.12).

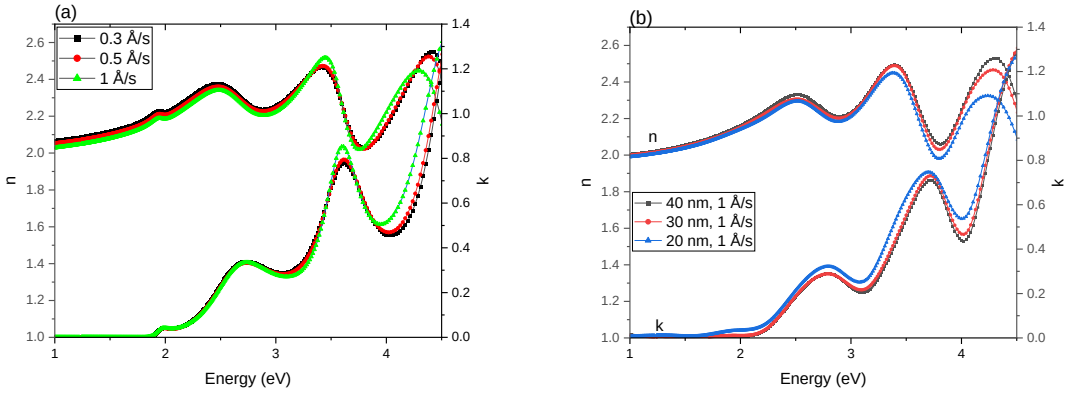


*Figure 4.20 Optical constant of $C_{60}$ films with different (a) deposition rate and (b) thickness.*

Further discussions on the comparison of the energy transitions with respect to the deposition rate and thickness are performed and summarized in Table 4.6 and compared to reference values from the Huckel calculation of the $C_{60}$ molecule [98].

*Table 4.6 The comparison of the observable absorption band of the $C_{60}$ film and *Huckel calculation* [100]

| Absorption electronic transitions | $C_{60}$ molecules* | 1 Å/s | 0.5 Å/s | 0.3 Å/s | 40 nm | 30 nm | 20 nm |
|---|---|---|---|---|---|---|---|
| | **(eV)** | **(eV)** | **(eV)** | **(eV)** | **(eV)** | **(eV)** | **(eV)** |
| $H_u \rightarrow T_{1u}$ | 1.90 | 1.95 | 1.95 | 1.95 | 1.95 | 1.96 | 1.97 |
| $H_u \rightarrow T_{1g}$ | 2.51 | 2.63 | 2.62 | 2.61 | 2.62 | 2.61 | 2.62 |
| $H_u \rightarrow H_g$ | 4.87 | 4.48 | 4.55 | 4.56 | 4.55 | 4.57 | 4.52 |
| $H_g \rightarrow T_{1u}$ | 2.86 | - | - | - | - | - | - |
| $H_g \rightarrow T_{1g}$ | 3.47 | 3.57 | 3.57 | 3.57 | 3.57 | 3.56 | 3.56 |

All three different deposition rates show the lowest energy transition of ~1.95 eV, corresponding to parity forbidden $H_u \rightarrow T_{1u}$ transition between the HOMO-LUMO due to electron vibration interaction resulting in a vibronic state. This indicates that the deposition rate shows a very small or almost no significant effect on the optical bandgap of the $C_{60}$ thin film. Moreover, with the different thicknesses, from 40 nm to 20 nm, the transitions $H_u \rightarrow T_{1u}$ increase from 1.95 eV to 1.97 eV, respectively. The energy transition at 2.857 eV related to the parity allowed $H_g \rightarrow T_{1u}$ transitions is not detectable in the optical constant, as this is mostly observed in optical studies and absorption spectra in solution form [76].

In addition, compared to the calculated optically allowed excitation for the $C_{60}$ molecule from literature, the transition peaks are not perfectly similar to the optical transition peaks for the $C_{60}$ thin film. This could be induced by changing the strength of the van der Walls intermolecular interaction between $C_{60}$ molecules after the evaporation process. This also has been reported in many literatures [76], [92], [99], [100].

The effect of deposition rate and thickness is also investigated by means of the UV Vis spectrophotometer method. Figure 4.21a shows that 0.3 Å/s of deposition rate exhibits lower absorption than other deposition rates, particularly at the 200 - 400 nm wavelength spectrum. The low absorption at 0.3 Å/s is most probably attributed to the grain size uniformity and the thin film's crystallinity, as observed in XRD images. On the other hand,

rougher surface morphology (1 Å/s) shows high absorption in the low wavelength range, which can potentially cause a parasitic absorption to the device of perovskite solar cells.

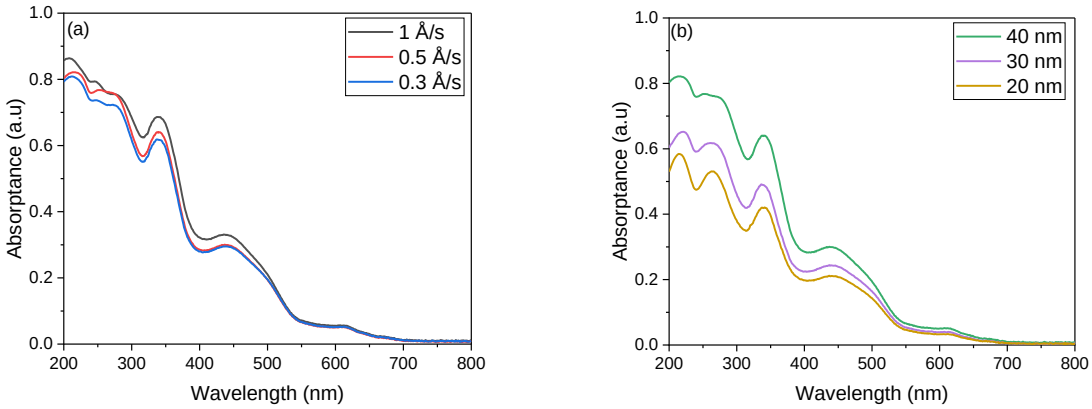


*Figure 4.21 Absorbtance profile of each layer at a specific wavelength with (a) different deposition rates, ~40 nm thick $C_{60}$ and (b)different thickness, 0.5 Å/s of deposition rate*

Furthermore, the thicker the film is, the higher the absorption (Figure 4.21b), which follows the Beer-Lambert law in Eq. (2.7). Therefore, from the optical properties, we know that increasing the thickness will increase the absorption and reduce the transmittance compared to the thicker one. In order to get the absorption value as low as possible and reduce the photon flux of the transport layer, thus increasing the thickness will also have a detrimental effect on the transport layer's optical quality. Further investigation on the effect of transport layer thickness on the perovskite/silicon tandem and perovskite solar cells (p-i-n) structure will be addressed in Chapter 6.

## 4.4 Summary

In order to obtain high-quality $C_{60}$ transport layer film in the thermal evaporation method, there are a few aspects that need to be taken into considerations, such as deposition process parameters, layer thickness, and rate of deposition. This Chapter successfully discusses and provide valuable insight into all of those aspects, which are summarized in the following bullet points:

- Firstly, control over deposition conditions and parameters provides a crucial indication of the film quality, particularly for thickness uniformity and regularity. Some approaches have been proposed, such as controlling the uniformity using Knudsen relation and slowly controlling the current to prevent particle clustering and agglomeration. In addition, the processing recipe has successfully been established to get reproducible in the processing and fabrication of $C_{60}$ using the thermal evaporation method.
- The resulting morphology and structural analysis indicate that 40 nm thickness with 0.3 Å/s represents the best characteristic. Conversely, a thinner layer indicates relatively high surface roughness and lower crystallinity.
- The identification of the optical constant for $C_{60}$ thin film has also been performed, and the proposed model works very well to extract the optical constant from $C_{60}$ thin film. It exhibits a good agreement with the existing literature. The optimized fitting procedure gives a reliable set of n,k data that can be used for simulation purposes.

# 5

# Optical Constants of $Cs_xFA_{1-x}PbI_{3-x}Br_x$ perovskite

This chapter will focus on extracting the optical constant of cesium mixed-cation lead mixed halide perovskite from ellipsometry measurement. The procedure of extracting the optical constant for perovskite film was not established in the PVMD group at the beginning of this thesis project.

A study from Tejada et al. [43] reported optical characterization and band-gap engineering of flat and wrinkle-textured $Cs_{0.17}FA_{0.83}PbI_{3-x}Br_x$ perovskite thin films with multiple compositions of halide (x) mixture. This study, however, used point-by-point analysis to observe the optical constant, by determining the $\tilde{n}$ for each individual wavelength. However, the method yields a high possibility for a noisy solution curve with several artifacts [42], such as diverging solution branches, discontinuities, and non-physical values. Furthermore, the perovskite materials were fabricated using a solution-based process, and no optical constants (n and k) data and/or figures were provided for further validation. Another study from Werner et al. also observed the complex refractive index of $Cs_yFA_{1-y}Pb(I_xBr_{1-x})_3$ but did not validated if the constants could reproduce perovskite cell results when used in optical simulation [104]. In addition, they used a sequential two-step hybrid deposition method, comprising a co-evaporation of $PbI_2$, followed by spin coating of the FA halide solution. Therefore, aside from understanding the process of extracting the optical constant from ellipsometry measurement, it is also needed to establish our own model to extract the optical constant of perovskite fabricated via thermal evaporation, which could be used for further optical simulation in our group.

Therefore, this chapter will provide a systematic study on the optical characterization of $Cs_xFA_{1-x}PbI_{3-x}Br_x$, followed by validation of the obtained model and optical constant. Note that the exact stochiometry for perovskite material that was used in this optical characterization is $Cs_{0.15}FA_{0.85}PbI_{2.85}Br_{0.15}$ processed via thermally evaporated in layer-by-layer with the order of *$PbI_2$ → FAI → CsBr* repeated 20 times to achieve the desired thickness. The final capping layer is 5 nm of $PbI_2$.

## 5.1 Extraction of the complex refractive index

### 5.1.1 Perovskite film crystallinity and surface roughness

Prior to any measurement, the sample was annealed at 100 °C for 30 minutes inside a nitrogen-filled glovebox. This specific annealing time and temperature have been observed and optimized in our group. It should be noted that during the transportation of one sample from one measurement to another, to minimize the exposure of perovskite samples to humid air, the samples were sealed in a plastic zipper bag inside the nitrogen-filled glove box. Also,

the box containing perovskites samples was fully covered by aluminum foil to prevent light degradation prior to measurement. For the first measurement, the average thickness was measured using profilometry with three different spots on the same substrate. The resulted average thickness was found to be ~151 nm. Since profilometry is a destructive measurement, this measurement used a different sample but at a similar batch of fabrication.

The $Cs_{0.15}FA_{0.85}PbI_{2.85}Br_{0.15}$ perovskite film was also characterized using XRD (Cu-$K\alpha_1$ radiation) to check the perovskite crystalline phase, i.e., black absorbing perovskite phase. Figure 5.1 indicates the X-ray diffraction pattern of the perovskite after annealing. It displays two main peaks of the high degree of crystallinity of cubic photoactive α-phase at 2θ of 14.03 and $28.19^0$, showing (001) and (002) crystal orientation, respectively. These peaks show an excellent agreement with the reported literature for perovskite fabricated via thermal vacuum deposition [105], [106]. In addition, the figure exhibits a small peak at $2\theta = 12.69^o$ that is associated with a small excess fraction of crystalline $PbI_2$.

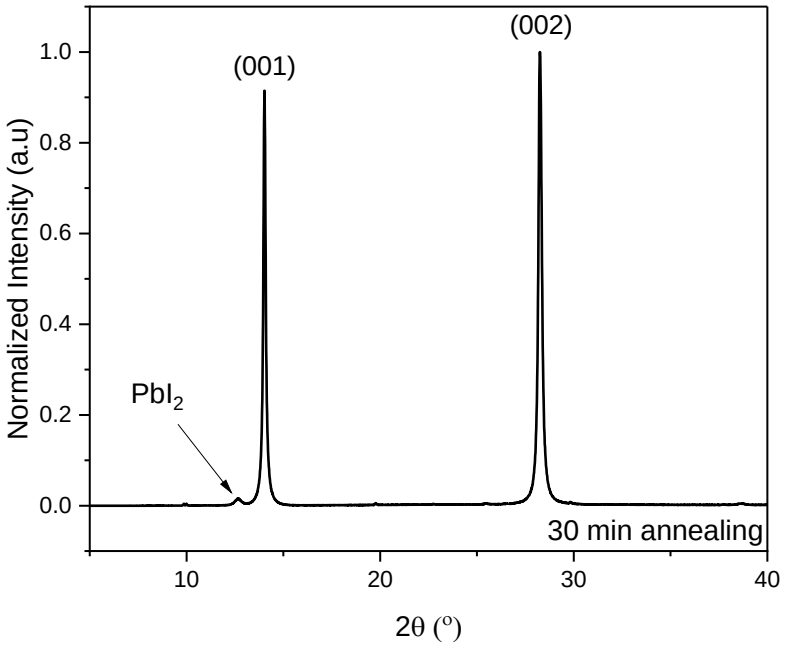


*Figure 5.1 X-ray diffraction pattern of $Cs_xFA_{1-x}PbI_{3-x}Br_x$ with 30 min annealing time at 100 $^0C$*

This small amount of residual $PbI_2$ is also in agreement with the literature [107]. Chiang et al. reported that this inclusion of small excess of $PbI_2$ could provide passivation and stabilization of the film by creating a protective layer at the grain boundaries [105].

Furthermore, the morphology observation was also conducted to check the surface roughness and morphology. The 3D surface morphology of perovskite film appears in Figure 5.2. The figure shows that the surface is uniform, and no pinhole was observed. The highest height difference in AFM measurement is found to be 30.2 nm. This highest difference is probably associated with the dust particles or excessive top layer of $PbI_2$, which do not react during deposition. This can be observed in the left corner of the AFM image.

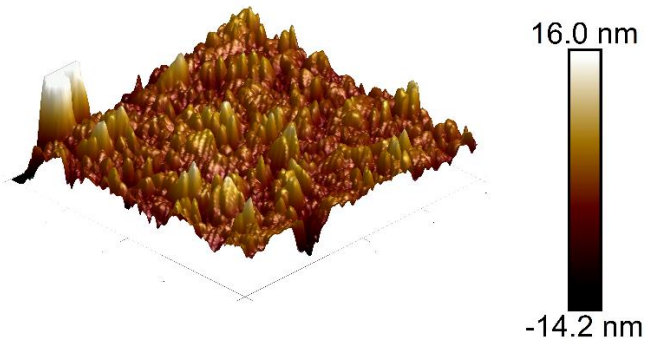


*Figure 5.2 The 3D AFM image for perovskite thin film*

Table 5.1 summarizes the detailed surface roughness observation for the perovskite material. Note that for one point AFM measurement, it takes roughly 30 to 45 minutes, thus to avoid long exposure time and degradation of our perovskite sample, the measurement was performed only in two different positions using tapping mode (non-contact mode) with the projected surface area was 4 $\mu m^2$.

*Table 5.1 AFM Roughness measurement of Perovskite*

| **Position** | **RMS (nm)** | **Average roughness (nm)** | **Maximum roughness (nm)** | **Standard deviation (nm)** | **Surface area difference (%)** |
|---|---|---|---|---|---|
| 1 | 4.24 | 2.80 | 30.20 | 4.24 | 1.18 |
| 2 | 3.57 | 2.26 | 36.50 | 3.57 | 0.84 |
| Average | 3.90 | 2.53 | 33.35 | 3.90 | 1.01 |

Figure 5.3 shows the SEM image of the sample where It shows a relatively uniform morphology. This is reasonable since the final top layer during the deposition was the PbI2 layer. The SEM image also confirms the presence of unreacted PbI2 which has been observed in XRD measurement, indicated by the white needle-like shape.

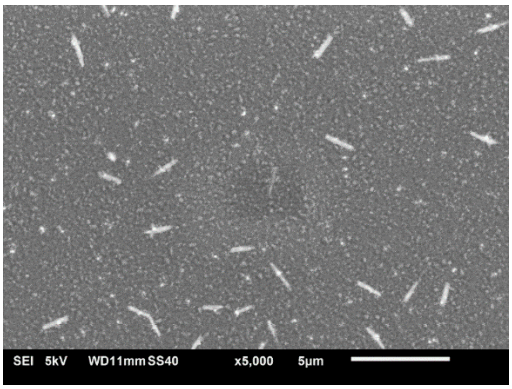


*Figure 5.3 The SEM image before spectroscopic ellipsometry measurement*

This small amount of excess $PbI_2$ is not detrimental in perovskite solar cells [108]. Instead, this composition could form a protective layer against moisture penetration, particularly when the $PbI_2$ composition is around 5% [105]. The black-ish square in the middle part in Figure 5.3 is the effect of the electron beam bombardment after a long time of measurement, and it is not related to the surface morphology of the material.

From the AFM and SEM observations, it has been investigated and confirmed that the perovskite was in perfect perovskite crystalline structure, uniform morphology, and no pinhole defect. Therefore, it is suitable to provide reliable data in extracting the optical constant from spectroscopic ellipsometry.

### 5.1.2 **Construction of the ellipsometry model**

The films were measured in air using reflectance mode in the wavelength range of 250 to 850 nm at angles of incidence of 55 - 70° with a 5° step. The thin-film perovskite layer was first modeled with a function of b-spline, with 0.1 eV resolution and 58 nodes. Figure 5.4 displays the measured psi "*ψ*" and delta "*Δ*" from the ellipsometry measurement and modeling using the b-spline method. The fitting achieves an MSE value of 3.04, indicating the excellent agreement between the model and the measured data.

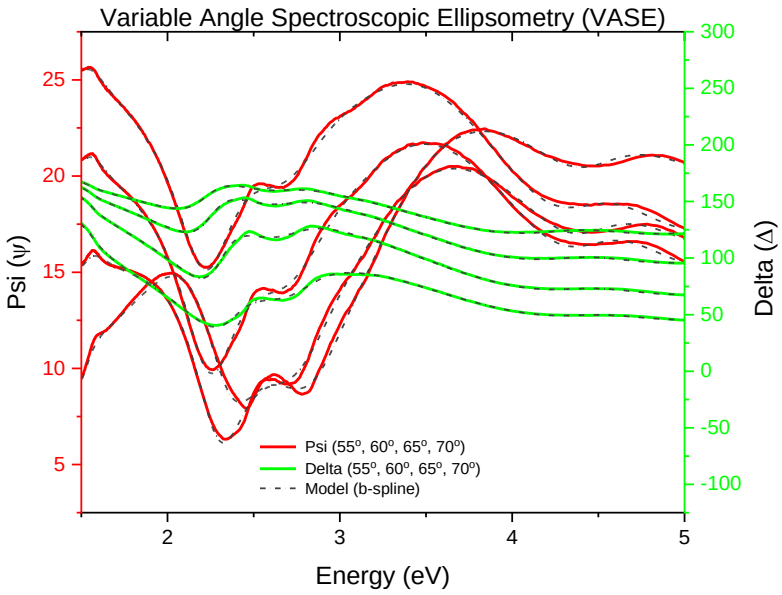


*Figure 5.4 Simulated (dashed line) and measured (solid line) ψ and Δ of $Cs_{0.15}FA_{0.85}PbI_{2.85}Br_{0.15}$ from multi-angle spectroscopic ellipsometry.*

The flexibility of b-spline curves allows to capture all of the essential details in the dielectric function and connect the transparent infrared region to the absorbing visible region [109]. After obtaining the psi and delta, the curves were then parameterized using a general oscillator approach with multiple Tauc-Lorentz oscillators. Remember that the complex refractive index ($N = n - ik$) and the complex dielectric function ($\varepsilon = \varepsilon_1 - i\varepsilon_2$) are related to each other by $\varepsilon = \varepsilon_1 - i\varepsilon_2 = N^2$. Thus, the optical constants (n and k) will be determined after obtaining the dielectric function. In addition, the corresponding real part of $\varepsilon_1$ can be obtained using the analytic solution of the Kramers-Kronig integration in Eq. (2.23).

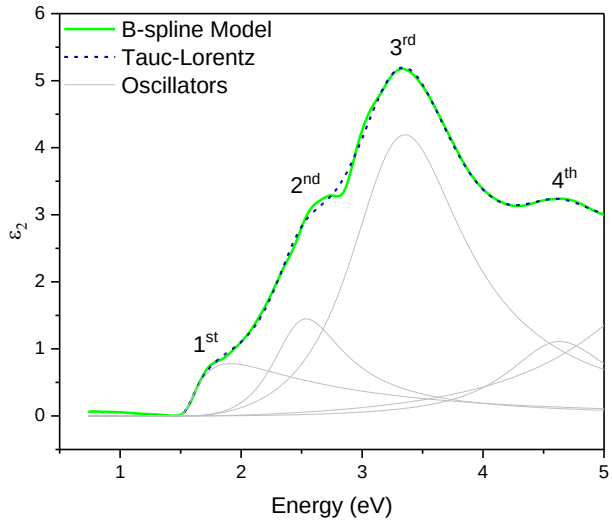


*Figure 5.5 Tauc-Lorentz oscillators (gray curves) used to model the imaginary part of $Cs_{0.15}FA_{0.85}PbI_{2.85}Br_{0.15}$ (green curve).*

Figure 5.5 shows the number of oscillators and the fitting curve of the b-spline model after being parameterized with the TL model. The Tauc-Lorentz can follow the B-spline model perfectly with the MSE of 0.104. While most of the studies on perovskite optical constant reported that three oscillators are sufficient and suitable at the range of 1.5 to 4.5 eV [40], [104], [109], adding more oscillators is necessary to capture a wider range of energy. In addition, since all of the oscillators are coupling each other, the additional oscillator can give a proper fitting shape with low MSE and thus a better optical constant representation.
Table 5.2 shows the fitting parameters and number of TL oscillators used in this study, with an MSE of 4.05, surface roughness of 2.32 $\pm$ 0.02 nm, and thickness of 140.87 $\pm$ 0.03 nm.

*Table 5.2 The fitting parameters of Tauc-Lorentz for the perovskite*

| Oscillator | $A_i$ (eV) | $C$ (eV) | Centre (eV) |
|---|---|---|---|
| $E_1$ | 3.16 $\pm$ 1.07 | 0.14 $\pm$ 0.01 | 1.95 $\pm$ 0.01 |
| $E_2$ | 9.45 $\pm$ 0.48 | 0.70 $\pm$ 0.01 | 2.62 $\pm$ 0.02 |
| $E_3$ | 5.46 $\pm$ 0.11 | 0.46 $\pm$ 0.01 | 3.57 $\pm$ 0.01 |
| $E_4$ | 7.69 $\pm$ 0.13 | 0.52 $\pm$ 0.01 | 4.52 $\pm$ 0.02 |

Figure 5.6 exhibits the comparison between the b-spline and Tauc-Lorentz oscillator model, particularly at the energy around the bandgap ($E_g$). The b-spline model is represented by the solid green line, and Tauc-Lorentz is the black dashed line.

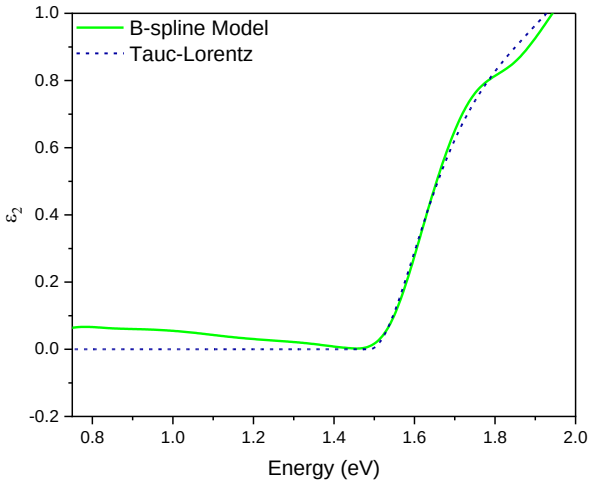


*Figure 5.6 B-spline (green line) after parameterized with Tauc Lorentz dispersion model*

The B-spline model shows that the extracted dielectric function is non-zero in the energy region even below $E_g$. This makes the model unphysical. Thus, with the TL oscillator, the curve can be more reliable and get zero absorptions at E < Eg. This result re-emphasizes that using b-spline only can create strong artifacts and non-representative data; therefore, combination with oscillator models, i.e., Tauc-Lorentz is required.

### 5.1.3 **Surface roughness considerations**

Since ellipsometry is a surface-sensitive analytical technique, larger roughness can influence the light scattering, a low refractive index in the visible region, and abnormal absorption below the bandgap [42]. In other words, this will generate inaccurate optical constants. Therefore the surface roughness model must be considered for the optical modeling using ellipsometry. In this study, the optical response of the surface roughness layer is represented by the Bruggeman EMA model, schematically indicated in Figure 5.7 [110]. This model considers the roughness as a layer consisting of variable fractions of the bulk perovskite material and void (air).

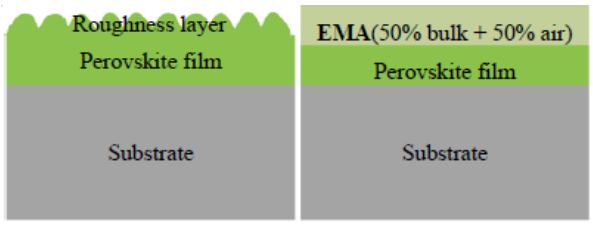


*Figure 5.7 Illustration of perovskite layer with (a) real roughness and (b) modeled with EMA* [41]

Fujiwara et al. demonstrated the increment of refractive index, and absorption coefficient spectra as the percentage of voids decreased [101]. Thus, the correct proportions for void and bulk are necessary for a proper optical model. In many reported SE studies of perovskite thin-film optical modeling, 50% bulk and 50% air (void) are most commonly used [38], [40]–[42], [109]–[111].

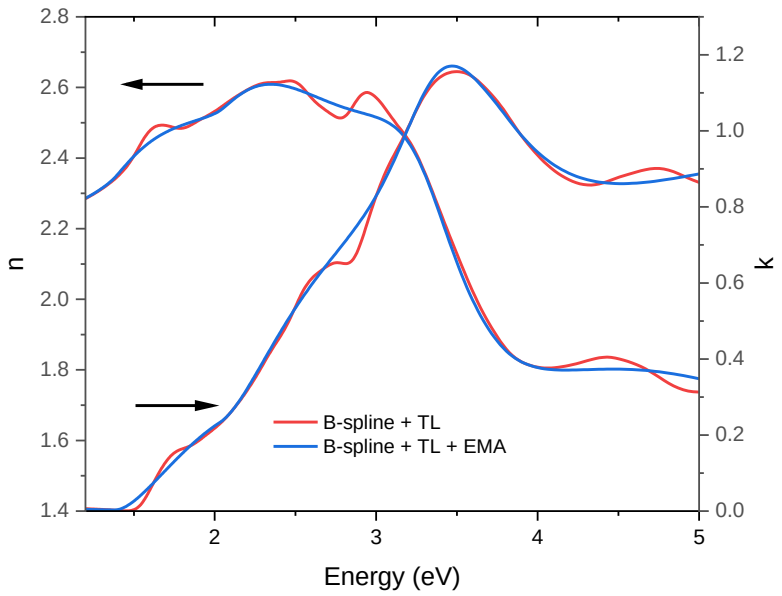


*Figure 5.8 The optical constant of perovskite using b-spline and Tauc Lorentz with Bruggeman EMA model (blue slide) and without EMA model (red line). The fraction of void is 50%, and bulk is 50%.*

Figure 5.8 demonstrates the optical constant of $Cs_{0.15}FA_{0.85}PbI_{2.85}Br_{0.15}$ with and without the addition of the Bruggeman EMA (50% air + 50% void) model for the roughness. It shows that the EMA model seems to oversimplify the curve, and some of the peaks are missing for both n and k values. In addition, the mean squared error is increased from 3.041 to 7.857. The roughness could be small enough to be effectively modeled with the Bruggeman EMA model [112]. Manzoor reported in their finding that even with 34 nm of RMS from perovskite film roughness, the roughness also could not be fitted effectively in SE measurement [109]. Also, a study from Tejada et al. demonstrated that the film with < 40 nm roughness can be considered as a flat sample, though still somewhat inhomogeneous topography. Thus in our measurement, the EMA model was not considered for the extraction of the optical constant since the surface roughness is relatively small (2.32 nm) and uniform. Most of the studies that employed the Bruggeman model were fabricated via the solution-based process where this fabrication technique tends to generate rougher surface morphology [38], [40], [42], [109]. On the other hand, our study uses the thermal evaporation method where the resulting RMS and roughness average are low, as shown in Table 5.1. The contribution of EMA even oversimplified the results where some of the oscillators' peaks are missing, i.e., at $E_1$ and $E_2$. In order to put the EMA model in optical modeling, it is recommended to check the roughness first, either using AFM or Tauc-Lorentz fitting, to get the preliminary data about the morphology of the sample. The EMA works very well when the roughness exceeds 40 nm or in textured/wrinkled substrate [43], [101].

### 5.1.4 **Optical constants**

The final optical constant obtained from this study is represented in Figure 5.9. The four oscillators are clearly visible as peaks in the extinction coefficient (k). The abrupt change in k between 1.5 to 2 eV represents the $Cs_xFA_{1-x}Pb(I_{1-x}Br_x)_3$ perovskite has sharper band edges and thus has a direct bandgap [42].

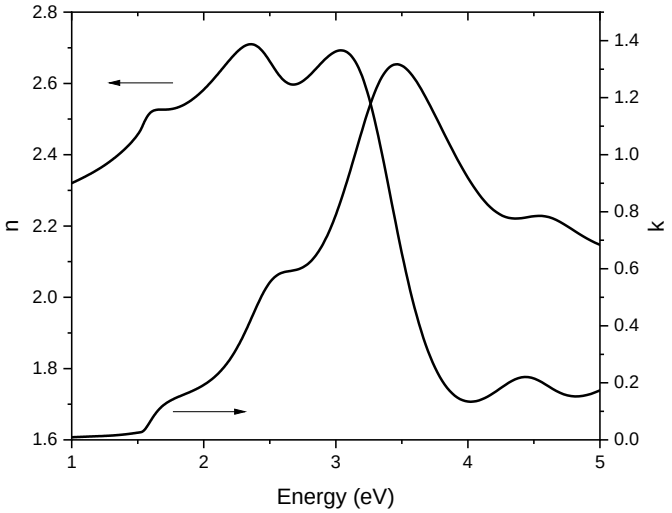


*Figure 5.9 Optical constant of $Cs_{0.15}FA_{0.85}PbI_{2.85}Br_{0.15}$*

Moreover, the real part of the refractive index (n) maximum at 2.36 eV is shown to be 2.70. This value matches closely with the maximum refractive index reported by Manzoor et al. [109]. However, the position of the peak slightly changed, which will be explained further in subsection 5.2.2. This refractive index also indicates that perovskite $Cs_{0.15}FA_{0.85}PbI_{2.85}Br_{0.15}$ is ideally suited as an anti-reflective coating for silicon solar cells, underlines the promise of $Cs_{0.15}FA_{0.85}PbI_{2.85}Br_{0.15}$/silicon tandem solar cells [60].

## 5.2 Validation of the model

The validation of the model was performed by comparing the resulting model with the experimental data and then to existing literature.

### 5.2.1 Comparison to experimental data

For the first validation step, the roughness from the ellipsometry measurement was compared to the roughness from the AFM measurement. During SE measurement, the surface roughness was set as a parameter and will be one of the outputs from the fitting results. The obtaining roughness from ellipsometry is compared to the surface roughness from the AFM measurement. As it is summarized in Table 5.1, the RMS for the perovskite was measured to be 3.90 nm, while the SE measurement was 2.32 nm. High RMS in AFM measurement could be affected by the particle and/or impurities that were detected during the measurement, as observed in the AFM image in Figure 5.2. Besides the roughness, the thickness comparison also was performed by comparing the thickness from ellipsometry and profilometry. The thickness from ellipsometry is 141 nm, while the thickness from the profilometry is ~150 nm. The slight difference between these two measurements is probably due to the unsimilarity of the sample uniformity. Even though both samples were from the same batch of fabrication, the position inside the chamber was still different. As has been discussed in Chapter 4, the place inside the chamber will also determine the thickness uniformity.

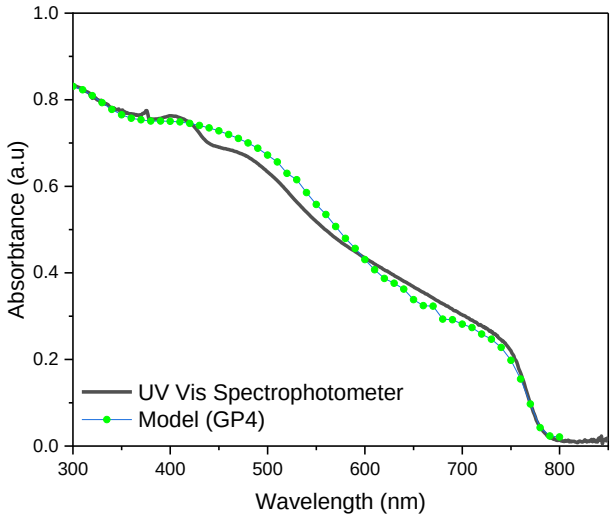


*Figure 5.10 Absorptance figure from UV VIS spectrophotometry measurement and from modeling.*

The next validation was performed by comparing the optical absorbance and bandgap calculation for the perovskite material. With the help of GenPro4 optical simulation, the absorbance of the perovskite layer was determined using the extracted optical constants (n and k). Figure 5.10 shows the comparison of absorptance from UV-Vis spectrophotometry and the n and k data extracted from ellipsometry. Both curves indicate a similar position of absorption onset at 785 nm. In the visible spectra, particularly at 420 to 600 nm, the green dot line from the model is slightly higher than spectrophotometry measurement, indicating higher photon absorptance. It is widely reported that SE measurement is surface-sensitive (sensitivity ~0.1 Å) [41], [73], while spectrophotometry is robust to roughness and can not precisely measure the contribution of the roughness even with a 10 nm roughness layer [42]. Thus, in spectrophotometry, the extra light collection due to surface roughness is sometimes underestimated when the roughness is too low.

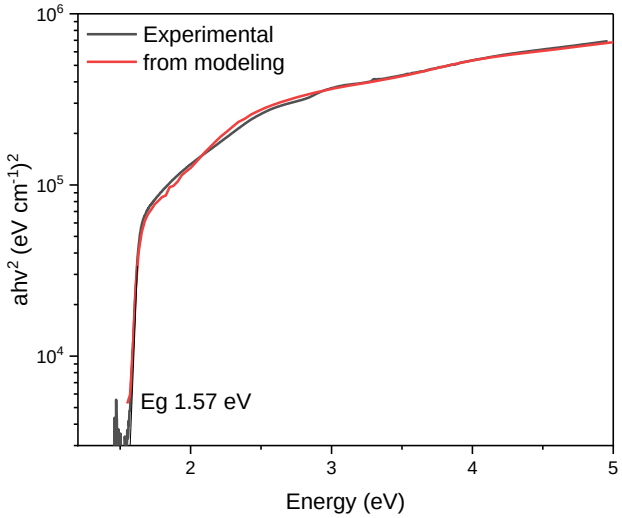


*Figure 5.11 Bandgap calculation from UV Vis spectrophotometry (black line) measurement and modeling from SE measurement (red line).*

Figure 5.11 represents the bandgap calculation and compares the experimental and modeling bandgap plotted in $\alpha hv^2$ as a function of energy. Please note that the absorption

coefficient ($\alpha$) from SE was calculated according to $\alpha = 4\pi k/\lambda$, with $\lambda$ being the wavelength, and the absorption coefficient from spectrophotometry was directly measured. The two spectra are in excellent agreement over the entire spectral range of interest. From both measurements, the bandgap was calculated to be ~1.57 eV.

### 5.2.2 **Comparison to the existing literature**

The second step of validation was to compare the obtained optical constant with the existing literature. Figure 5.12 exhibits the n and k from this study compared to the optical constant from Manzoor et al. with the different Cs and Br ratios [109].

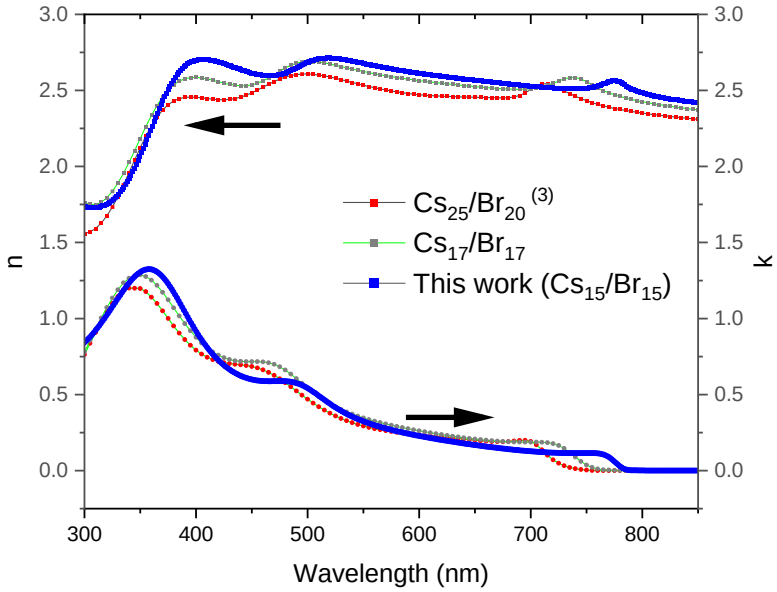


*Figure 5.12 Comparison of determining optical constant with those available in the literature for $Cs_xFA_{1-x}PbI_{1-x-Br_x)_3}$ perovskite* [109]

For simplification, we refer $Cs_xFA_{1-x}PbI(_{1-x}Br_x)_3$ perovskite by the Cs and Br content. For example, $Cs_{0.25}FA_{0.75}Pb(I_{0.8}Br_{0.2})_3$ is referred to Cs25/Br20 [109]. In relation to $Cs_{25}/Br_{20}$ and $Cs_{17}/Br_{17}$, the oscillator position for our work is red-shifted, with the highest shift occurring near the bandgap and a modest shift at high energies. This observation might be explained by the addition of Cs and Br that leads to an increase in the bandgap [46], [105], [110], [113]. Thus lesser CsBr compositions will obtain lower bandgap energy and shift the curve to the long-wavelength. Besides the CsBr composition, these two studies' discrepancies can also be explained by the fit methods and fit quality. In Manzoor et al. study, the MSE is relatively high (11.83) with only three oscillators, while our work has shown that the fitting quality is better with the MSE of 4.05 (four oscillators). In addition, our study also has a low surface roughness (2.32 nm) and a thinner layer (~140 nm). On the other hand, the study from Manzoor et al. used thicker layer thickness (~591.34 nm) and higher surface roughness (15.05 nm) of perovskite thin film, processed in a solution-based method [109]. These differences in surface roughness, layer thickness, and fabrication method, can significantly contribute to the deviations for the two studies [74].

Finally, the observation on changes in the crystallinity phase was performed by comparing the XRD pattern before and after the SE measurement. This step is crucial to determine whether the perovskite layer was not degraded during or after the SE measurement. Note that even though the sample was sealed inside the zipper bag and protected by aluminum foil during the transport, still the SE measurement was performed for roughly 20 - 30 minutes

in the air. Thus it is important to identify the changes of the perovskite phase after this exposure time. Figure 5.13 shows the XRD pattern of the PVK layer before and after ellipsometry measurement.

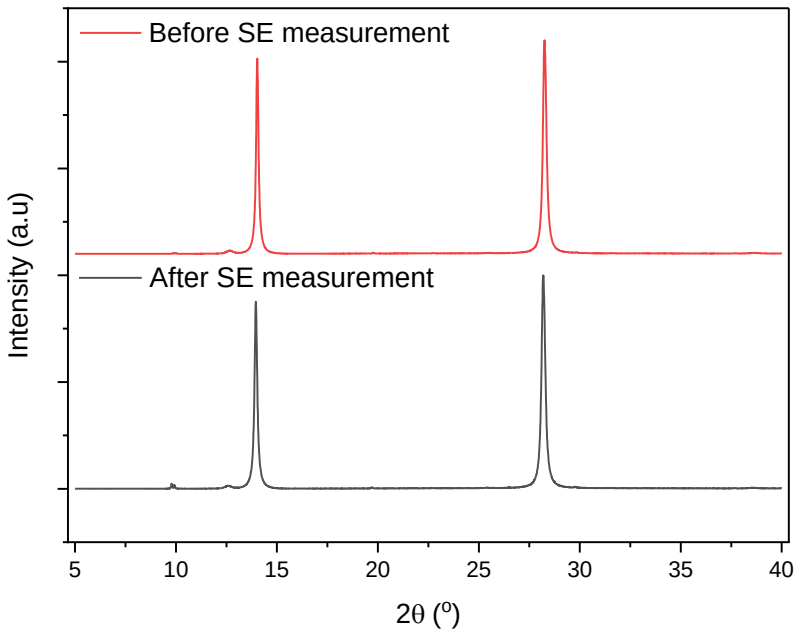


*Figure 5.13 X-ray diffraction pattern before (red line) and after (black line) spectroscopic ellipsometry*

It reveals that no significant changes in the crystallinity phase of the perovskite. The strongest perovskite peaks are indicated at 2θ of 14.03 and 28.19 degrees, where both measurements exhibit similar intensity and peaks position. This XRD result demonstrates that the perovskite crystal structure was still present, stable, and had no significant change during the SE measurement and even after the SE measurement. Therefore, the optical property extracted are not affected by degradation and are reliable in that respect.

## 5.3 Summary

To sum up this chapter, we have successfully established a procedure to extract and determine the optical constant for the $Cs_{0.15}FA_{0.85}PbI_{2.85}Br_{0.15}$. Besides filling the knowledge gaps on optical constant determination, this study can also benefit our group, particularly for the optical modeling purpose where no optical constants have been extracted in-house so far for perovskite films. In addition, this project also successfully combines the b-spline and TL models approach to arrive at a physics-based oscillator that follows the Kramers-Kronig relation. This study suggests that more than three TL oscillators are necessary to capture both the sub-bandgap absorption and high energy region, thus obtaining the lowest possible MSE ~4.05.

Furthermore, the obtained surface roughness and thickness from SE are 2.34 nm and 141 nm, respectively. It shows good agreement with the AFM measurement (3.4 nm) and the thickness calculation from profilometry (155 nm). Although AFM can provide high-precision data, they are generally difficult to operate, expensive, and time-consuming. In contrast, SE can give information on not only the optical properties of the material but also the thickness and surface morphology with a faster and easier process. Besides confirming the validity of the model, our study shows that SE can be a very powerful tool to get not only optical constant, but also surface roughness and layer thickness.

# 6
# Optical Simulations

As the perovskite solar cell is comprised of many layers such as TCO, HTL, perovskite, ETL, and metal contact, the analysis of the device structure as an optical stack is essential for optimizing the light-harvesting of the perovskite absorber layer and maximizing the photocurrent generation. In the previous chapter, we have extensively studied and obtained the optical constant for $C_{60}$ ETL and perovskite using a combination of the b-spline model and the Tauc-Lorentz dispersion model. Moreover, the optical constant for quartz and $MoO_x$ was measured using the Cauchy and b-spline and Tauc-Lorentz models, respectively. The resulting optical constant and detail of the measurements are provided in Appendix A.4. Note that the optical constant for ITO was measured previously by another member in our group [114], and metal contact (Ag) was taken from the literature [115]. The details of each layer and optical model for extracting the optical constant are presented in Table 6.1.

*Table 6.1 Summary of dispersion models used for each layer comprised the perovskite solar cells*

| | **Dispersion model** |
|---|---|
| **Quartz** | Cauchy |
| **ITO** | Cody-Lorentz and Drude |
| **MoOx** | B-spline + 1 TL oscillator |
| **Perovskite ($Cs_{0.15}FA_{0.85}PbI_{2.85}Br_{0.15}$)** | B-spline + 4 TL oscillators |
| **$C_{60}$** | B-spline + 5 TL oscillators |
| **Ag** | Drude model [115] |

Therefore, this chapter will investigate the contribution of each layer on optical losses of perovskite solar cells via optical GenPro4 simulation at a device level where the optical constants (n and k) are the inputs. The simulation is performed by assuming that each layer with optically flat interfaces where a basic ray-optics model based on the Fresnel equations for reflectance and Snell's law for refraction angles are used. A complete working principle of the GenPro4 software can be found in ref. [88]. First optical modeling will be performed on a single junction PSCs with a p-i-n architecture (see Figure 1.3b). Specifically, the implied photocurrent density ($J_{ph}$) of perovskite solar cells with different deposition rates and thicknesses of $C_{60}$ and contributions of other supporting layers in parasitic absorption will be identified. Further investigation on semi-transparent perovskite solar cells (ST-PSCs) is also conducted to emphasize the potential of our perovskite solar cells as a top cell in perovskite/Si tandem devices.

## 6.1 Single junction perovskite with inverted p-i-n architecture

### 6.1.1 Identification of optical losses

Figure 6.1 illustrates the structure of inverted p-i-n perovskite solar cells with their corresponding thickness before the optimization. In p-i-n architecture, the incident light illuminates the quartz substrate from the HTL side. We carry out the simulation to investigate the contribution of each layer in parasitic absorption. For the first simulation, the perovskite thickness was kept fixed at 400 nm. This thickness was adopted from the investigation of optimum thickness for $CH_3NH_3PbI_3$ perovskite reported by Shirayama and co-workers based on the internal absorptance spectra calculation [111]. They reported ~ 20 mA/cm$^2$ of $J_{sc}$.

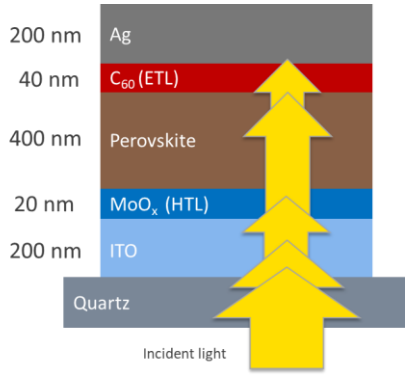


*Figure 6.1 Schematic representation of perovskite p-i-n planar architecture and corresponding thicknesses*

Figure 6.2 shows the breakdown of optical losses in the perovskite p-i-n structure with the quartz/$MoO_x$/perovskite/ETL/Ag layer stacks (see Figure 6.1) in the spectral wavelength range of 300 – 800 nm. We found that front-surface reflection contributes to the main optical loss indicated by white color area, accounting for 4.62 mA/cm$^2$. Besides reflection, Figure 6.2 also shows that other main optical losses, usually indicated as parasitic absorption, are from ITO and $MoO_x$ layers, contributing ~1 mA/cm$^2$ and 0.42 mA/cm$^2$, respectively.

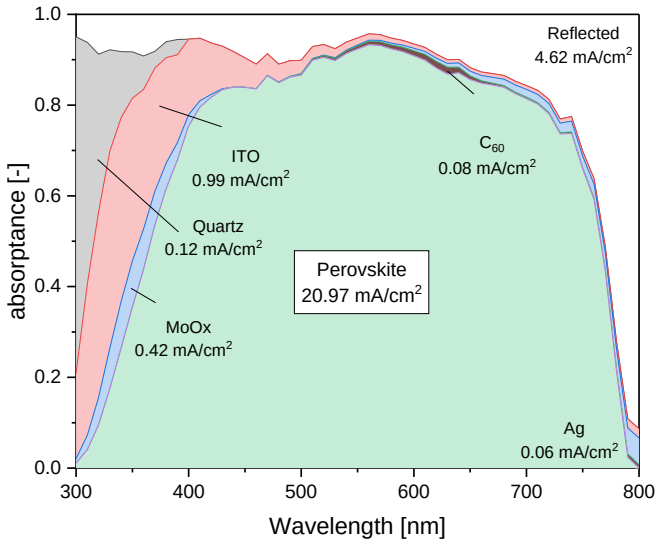


*Figure 6.2 GenPro4 simulation of the perovskite solar cells with p-i-n structure using n,k data extracted from 40–nm-thick of $C_{60}$ layer deposited at 0.5 Å/s deposition rate*

The reflectance loss can be overcome by using an anti-reflective coating on the front side (from the incident light) of perovskite solar cells [116]. The interference effect of anti-reflective coatings leads to wave reflected from the top surface being out of phase with wave reflected from semiconductor [60], [117]. These out-of-phase reflected waves enable destructive interference. Some of the anti-reflective coatings that have been introduced in literature, such as magnesium fluoride ($MgF_2$), lithium fluoride (LiF), silicon dioxide ($SiO_2$), and aluminum dioxide ($Al_2O_3$) [117]. Another way is by textured surfaces, allowing to minimize the reflection by increasing the chances of reflected light bouncing back onto the surface, rather than out to the surrounding air [60].

*Table 6.2 Summary of simulated optical losses of perovskite solar cells with different $C_{60}$ thicknesses and deposition rates.*

| | **1 Å/s, 40 nm** | **0.5 Å/s, 40 nm** | **0.3 Å/s, 40 nm** | **0.5 Å/s, 30 nm** | **0.5 Å/s, 20 nm** |
|---|---|---|---|---|---|
| | [mA/cm$^2$] | [mA/cm$^2$] | [mA/cm$^2$] | [mA/cm$^2$] | [mA/cm$^2$] |
| **Reflected** | 4.62 | 4.62 | 4.62 | 4.62 | 4.62 |
| **Quartz** | 0.12 | 0.12 | 0.12 | 0.12 | 0.12 |
| **ITO** | 1.00 | 1.00 | 1.00 | 1.00 | 1.00 |
| **MoOx** | 0.42 | 0.42 | 0.42 | 0.42 | 0.42 |
| **Perovskite** | 20.97 | 20.97 | 20.97 | 20.99 | 21.01 |
| **$C_{60}$** | 0.08 | 0.08 | 0.08 | 0.05 | 0.03 |
| **Ag** | 0.06 | 0.06 | 0.06 | 0.06 | 0.07 |

The effect of thickness and deposition rate of $C_{60}$ is summarized in Table 6.2. The detail of this GenPro4 simulation is provided in Appendix A.3. It can be seen that the variation of the $C_{60}$ deposition rate (from 1 to 0.3 Å/s) shows no significant effect on the $J_{ph}$ of the perovskite absorber layer. Since all of the layers have a similar thickness and are located in the perovskite's backside, most of the photons are already absorbed by the layers on top of $C_{60}$. Moreover, it can also be seen in the n and k data in Figure 4.20, where varying the deposition rate has a more negligible effect on the optical constant, particularly in the visible range wavelength. On the other hand, changing the thickness from 40 to 20 nm slightly increases the $J_{ph}$ from 20.97 to 21.01 mA/cm$^2$. As has been illustrated in Figure 3.7a, the incident photons can bounce back between the interface. Thus the contribution of the rear reflection from the Ag electrode can be largely absorbed by $C_{60}$ when a thicker $C_{60}$ layer is applied.

### 6.1.2 **Thickness optimization**

The implied photocurrent of perovskite solar cells from this inverted p-i-n structure could be improved by adjusting the thickness of the layers above the perovskite absorber layer ($MoO_x$ and ITO layer). We perform numerous simulation to obtain the optimized thickness with the highest $J_{ph.}$ Figure 6.3 shows that the 2D contour plot of $J_{ph}$ perovskite solar cells as a function of different $MoO_x$ and ITO thicknesses. It shows that the maximum point (red color) for single-junction perovskite is achieved by reducing the thickness of $MoO_x$ and ITO to 10

and 40 nm, respectively. Note that the thickness variation from $MoO_x$ is limited from 5 to 40 nm in this optimization, where the ITO is from 20 to 200 nm.

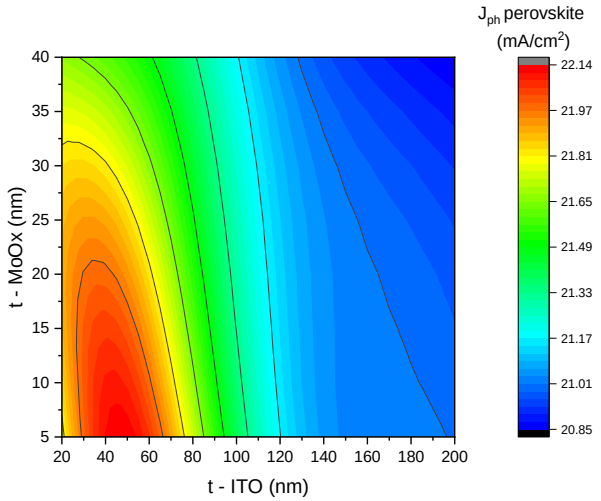


*Figure 6.3 Thickness optimization of $MoO_x$ and ITO with regard to implied photocurrent of perovskite solar cells.*

As observed in Figure 6.3, increasing the thickness for both layers will decrease the $J_{ph}$ of perovskite, i.e., increase the parasitic absorption of $MoO_x$ and ITO. On the other hand, even though a thinner layer could optically reduce the parasitic absorption, but there are some limits due to sheet resistance. Moreover, a thinner layer can provide non-conformal coverage for the layer underneath [117].

Furthermore, Figure 6.4 shows the implied photocurrent of the perovskite solar cell as a function of its thickness. As it can be seen, a thicker perovskite absorber layer absorbs more light and gives rise to a higher implied photocurrent. In contrast, a thin perovskite layer yields low photocurrent due to lower photon absorption. It is worth noticing that increasing the thickness leads to poor charge collection efficiency due to an increase in series resistance and recombination within the perovskite layer [118]. In conclusion, in our final simulation, the thickness of the perovskite absorber layer is kept fixed at 500 nm with a $J_{ph}$ of 20.70 $mA/cm^2$. This 500 nm thickness is in good agreement with the one reported by Fakhri et al. [119]; they found that when the layer's thickness was less or more than 500 nm, the efficiency of the PSCs decreased, specifically in inverter p-i-n architecture.

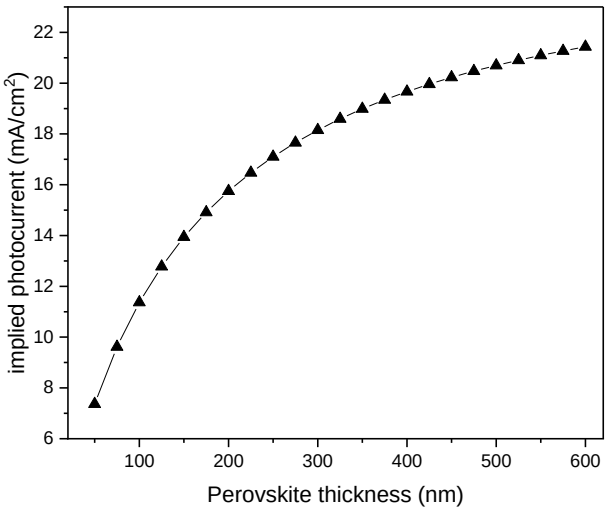


*Figure 6.4 effect of perovskite thickness on the implied photocurrent density of the perovskite solar cells.*

## 6.2 Semi-transparent PSCs as a top cell candidate in perovskite/Si tandem device

One of the key parameters for enhancing the efficiency of perovskite/silicon tandem devices is the use of semi-transparent perovskite solar cells (ST-PSCs), which require transparency and conductivity of top electrodes [117], [120], [121]. Therefore, the inverted p-i-n structure in Section 6.1 needs to be adjusted by changing the Ag top electrode with a transparent electrode. The deposition sequence is still the same follows ITO/HTL /perovskite/ETL/transparent electrode stacks, but the illuminated light comes from the top layer since the bottom cell is filled by silicon solar cells (illustrated in Figure 6.5). Several different types of transparent electrodes have been introduced in the literature, such as ITO, FTO, graphene-based transparent electrodes, carbon nanotube, silver nanowires [121], [122]. This study focuses on ITO electrodes because of their high transparency (>80% T) in the visible range, good conductivity and has been successfully applied in different types of solar cells [117]. ITO is usually deposited by magnetron sputtering, which not only requires high pressure and temperature but also generates damage to the underlying organic transport layer and perovskite absorber layer. Thus, an additional $SnO_2$ buffer layer is placed to protect the layer beneath during the sputtering process [123], [124].
The optical simulation of ST-PSCs is done using GenPro4 [88] to indicate the optical losses in the 300 – 800 nm wavelength region. The initial ST-PSCs configuration and layers thicknesses used in this work are presented in Figure 6.5a. For the first simulation of ST-PSCs, the thickness of the top ITO is kept at 170 nm, following the results reported previously by Zhang et al. They obtained high transmittance and low parasitic absorption of ITO [125]. In addition, the bottom ITO also is kept at 30 nm, following the best result from the ref. [114]

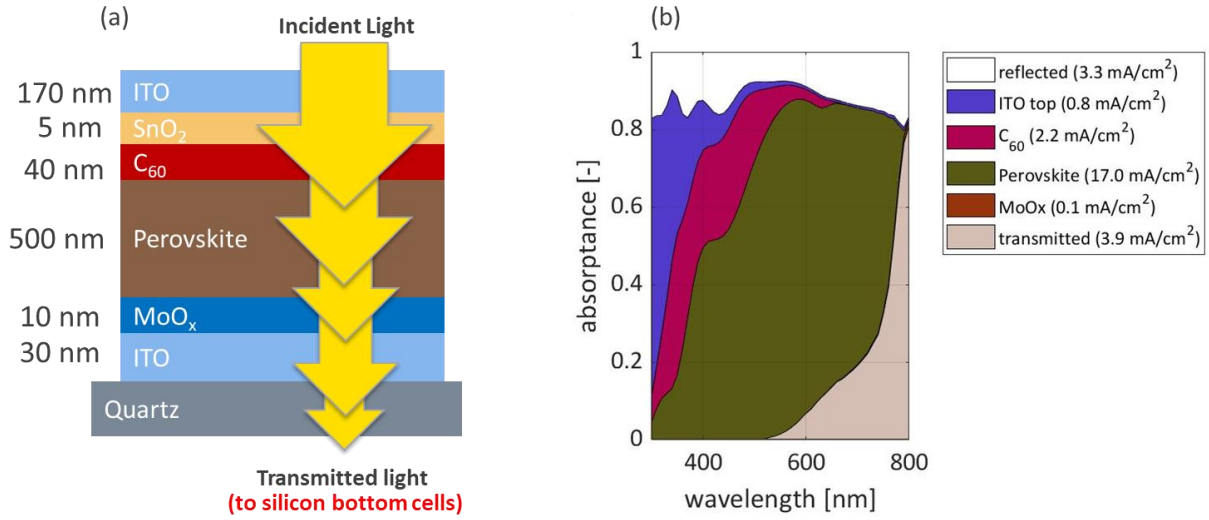


*Figure 6.5 Semi-transparent perovskite solar cells before optimization with (a) layers stacks and corresponding thicknesses and (b) the breakdown of supporting layer optical loss simulated via GenPro4 software.*

Moreover, Figure 6.5b shows the breakdown of optical losses with a 40 nm thickness of $C_{60}$. The main portion of optical losses is shown by the reflected light (3.3 mA/cm$^2$), ITO top layer (0.8 mA/cm$^2$), and the $C_{60}$ transport layer (2.2 mA/cm$^2$). To reduce the reflection loss, we performed the simulation again by applying an anti-reflective coating of $MgF_2$ (150 nm) at the ITO/air interfaces, as indicated in Figure 6.6a. The choice of 150 nm thick $MgF_2$ is also suggested by Zhang et al. for optimum reduction of reflection loss in the ST-PSCs. [125]. After placing the 150 nm thick of $MgF_2$, the total reflected light is reduced from 3.3 mA/cm$^2$ to 1.7 mA/cm$^2$ (Figure 6.6b). However, the optical losses from ITO and $MoO_x$ layers are still there. These optical losses are because both ITO and $MoO_x$ show absorption in the wavelength range of 750 to 800 nm, i.e., non-zero extinction coefficient "k" value (see Appendix A.4). At the same time, perovskite has no absorption since it already passes the absorption edge (bandgap).

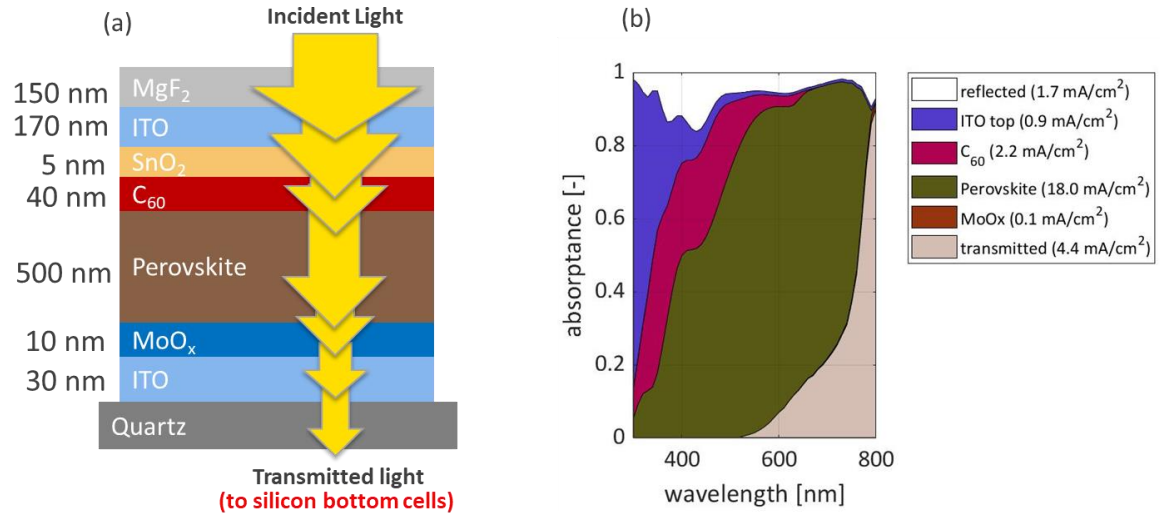


*Figure 6.6 Semitransparent perovskite solar cells (a) with an additional 150 nm of $MgF_2$ and (b) the breakdown of each layer optical response simulated via GenPro4.*

Further investigation is performed to identify the effect of $C_{60}$ towards the resulting implied photocurrent density in ST-PSCs, where we vary the thickness from 5 to 40 nm.

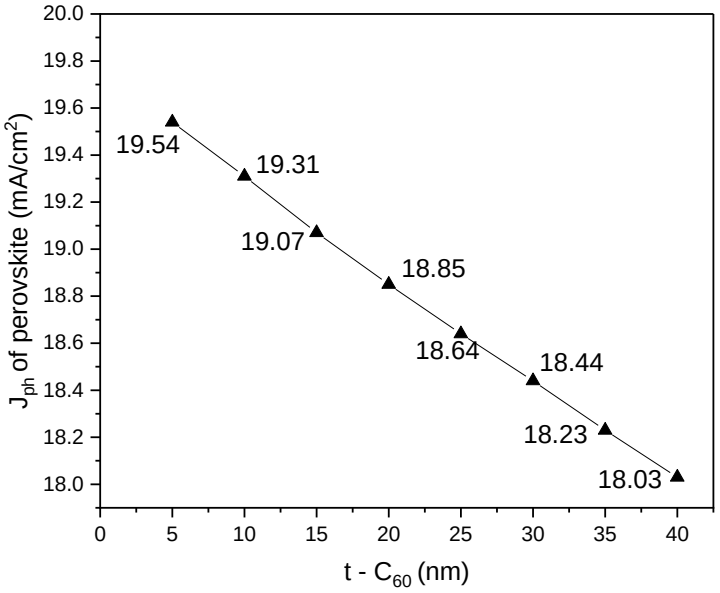


*Figure 6.7 Effect of $C_{60}$ layer thickness on the implied photocurrent of perovskite.*

Figure 6.7 shows that increasing the $C_{60}$ thickness will decrease the amount of photocurrent that perovskite can absorb. Since $C_{60}$ is located on the front side of illuminated light, the optimization program will always suggest the thinnest $C_{60}$ layer within the investigation wavelength range. Yoon et al. experimentally investigated the effect of $C_{60}$ layer thickness (10 – 40 nm) on the perovskite solar cell's performance. A 35 nm thickness of the $C_{60}$ layer shows homogenously and conformal film coverage with improved electron extraction, resulting in eliminating photocurrent hysteresis and showing the best efficiency of 19.1%. Although the light absorption increases and potentially contributes to parasitic losses, it highly enhances the carrier transport and improves PSCs performance [28]. Another study by Lee et al. reported that less than 10 nm-thick thermally evaporated $C_{60}$ film in regular-type perovskite solar cells resulted in a power conversion efficiency of less than 9% due to a small fill factor as the effect of small coverage of $C_{60}$. In conclusion, according to this optical simulation and combined with literature, a 10 nm of $C_{60}$ should be acceptable to bring the balance between optical properties and PSCs performance. However, since this simulation is purely optical, an electrical measurement on the layer and device lever is required to further justify this selection, particularly for inverted p-i-n structures.

### 6.2.1 **Optical losses and transmittance in NIR wavelength region**

As the two subcells in tandem are optically coupled, the perovskite top cells need to have high transparency in the range of near-infrared (NIR) wavelength to allow the photon to reach silicon bottom cells. Several studies have pointed out that free carrier absorption of the transport layer and ITO can induce significant losses and reduce the NIR transmission of perovskite solar cells [117], [125]. In this study, we carried out an optical analysis in the 800 - 1200 nm wavelength range to investigate these losses. Please remember that when all the photons in this wavelength range (800 – 1200 nm) can be converted to carriers and be collected, the maximum current density is 19.21 mA/cm$^2$ [125].

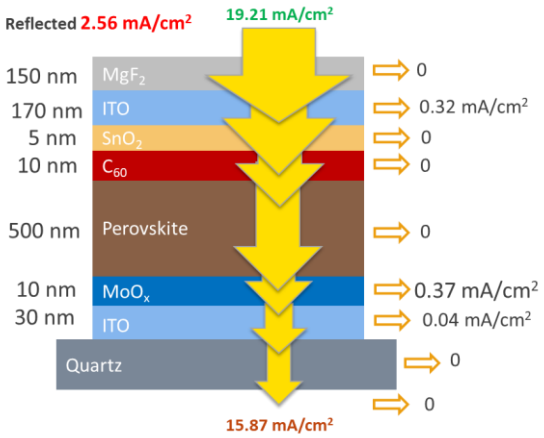


*Figure 6.8 Detailed optical loss analysis of ST-PSCs in the NIR (800 -1200 nm) wavelength range.*

The detailed optical losses caused by each layer are illustrated in Figure 6.8. The resulting figures from the GenPro4 simulation can be seen in Appendix A.5. From the investigation of optical losses in the NIR wavelength range, the reflected light contributes 2.56 mA/cm$^2$ of optical loss, top and bottom ITOs give 0.32 and 0.04 mA/cm$^2$, respectively, and $MoO_x$ gives 0.37 mA/cm$^2$. From the total of 19.21 mA/cm$^2$ of photocurrent density, 15.87 mA/cm$^2$ can be transmitted through the cells. Lal et al. in 2017 provided an overview of transmittance of ST-PSCs published by different authors, indicating that the NIR transmission was limited to about 80% [126]. In 2018, Duong et al. reported 84% of transmitted photocurrent in the NIR wavelength range [127].

### 6.2.2 Optimization of ITO and $MgF_2$ thicknesses

From the analysis of optical losses in Figure 6.8, the photocurrent of transmitted light ($J_T$) can be further increased by optimizing the thickness of $MgF_2$ and top ITO layers (also known as double-layer anti-reflection coating, DLARC). By varying the thickness from 20 to 200 nm for both layers, multiple simulations were conducted to achieve less reflected light and low parasitic absorption of ITO. The results of these simulations are presented in Figure 6.9, where the implied photocurrent of the perovskite solar cells transmission in the NIR wavelength range is plotted as a function of the thickness.

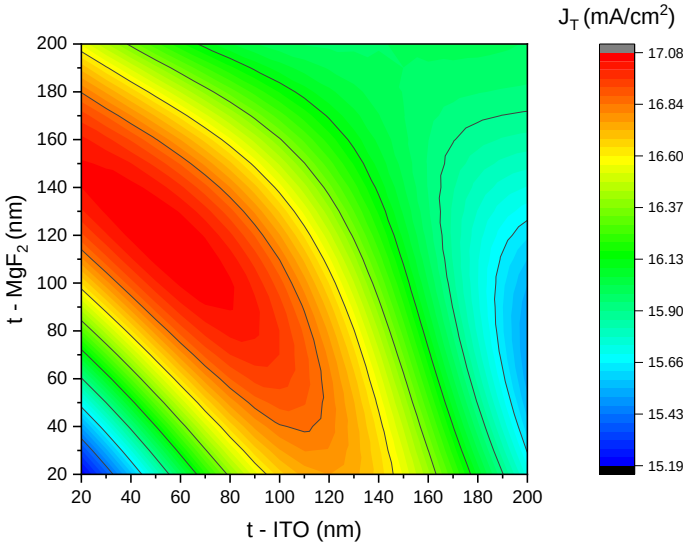


*Figure 6.9 GenPro simulation of the transmitted photocurrent ($J_T$) from different thicknesses of top ITO and $MgF_2$ varied from 20 to 200 nm.*

The optimum thickness of the top ITO and $MgF_2$ is 50 and 120 nm, indicated by the center of the red area in Figure 6.9. However, note that 50 nm of ITO is maybe too thin to fulfill the electrical requirements, as its sheet resistance will increase with a thinner layer [128]. Therefore it is useful to determine how thick the ITO can be deposited without compromising the obtaining of a high photocurrent transmission. We can see from the red circled area in Figure 6.9, it is possible to set 110 nm thick ITO with a combination of $MgF_2$ from 60 to 140 nm thick, without reducing the transmitted photocurrent too much and if the desired value of the implied photocurrent is set to be higher than 16.84 mA/cm2.

The result of optimized $MgF_2$ (120 nm) and top ITO layer (50 nm) then being analyzed with GenPro4, where the detailed optical loss analysis is provided in Figure 6.10.

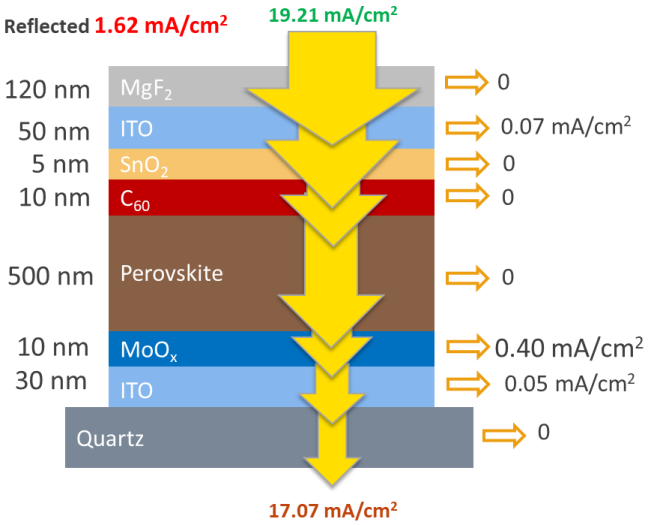


*Figure 6.10 Detailed optical loss analysis after $MgF_2$ and top ITO layer thickness optimization.*

The reflection loss is reduced to 1.62 mA/cm$^2$ (previously 2.56 mA/cm$^2$), and parasitic absorption from top ITO is reduced from 0.32 to 0.07 mA/cm$^2$. Consequently, with respect to transmission, $J_T$ increases to 17.07 (previously was 15.87 mA/cm$^2$). Figure 6.11 demonstrates the light transmittance from wavelength region 300 – 1200 nm after optimizing the thickness of $MgF_2$ and ITO.

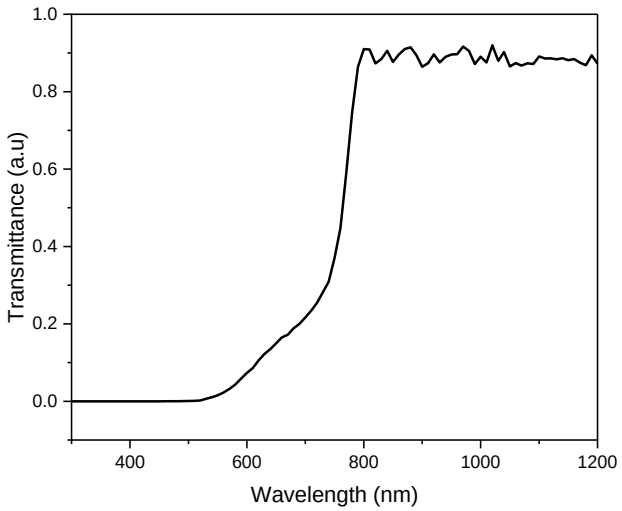


*Figure 6.11 Transmittance spectrum of the ST-PSCs with optimum ITO and $MgF_2$ thickness.*

These results represent that almost 88% of the photon is transmitted through the ST-PSCs and can be utilized by bottom cells. It is also worth noticing that high transmitted photocurrent is because of the absorption onset of our perovskite located at 785 nm of wavelength, which enables more light in the visible region to pass through the perovskite film and be absorbed by silicon bottom cells. Thus, it emphasizes that our perovskite could be beneficial for application as a top cell to improve the performance of perovskite/silicon tandem devices. The ST-PSCs are particularly needed for 4 terminal perovskite/silicon tandem devices, where the top and bottom cells are mechanically stacked with each other. In contrast, further investigation is required in 2 terminal perovskite/silicon tandem to check the current matching between the top perovskite solar cells and silicon bottom cells.

## 6.3 Summary

This chapter investigates the optical losses from the perovskite solar cells and provides some guidance for maximizing light absorption of the perovskite absorber layer by reducing the reflectance loss and optimizing the thickness of the supporting layers. The simulation was performed in two different configurations, where the results are summarized below:

The p-i-n perovskite solar cells

- The main optical losses in the p-i-n structure are from the incidence light's reflection and parasitic absorption from layers above the perovskite absorber layer. After optimizing the thickness of ITO and $MoO_x$, we found that 40 mn of ITO and 10 nm of $MoO_x$ is an ideal thickness to deliver high implied photocurrent of PSCs (22.14 mA/cm$^2$). Moreover, the variation of $C_{60}$ fabricated via three different deposition rates shows no significant influence on photocurrent density in p-i-n perovskite solar cells. By varying the thickness from 40 to 20 nm, it slightly increases the implied photocurrent of perovskite from 20.97 to 21.01 mA/cm$^2$ even though $C_{60}$ is placed on the rear side of illuminated light. The additional extra photocurrent collection is due to back reflection from the silver electrode.

Semi-transparent perovskite solar cells (ST-PSCs)

- In semi-transparent perovskite solar cells, the optical losses are investigated. In the wavelength range 300 - 800 nm, the main optical losses are due to light reflection, absorption in the $C_{60}$ layer, as well as ITO and $MoO_x$ layers absorption. The loss is reduced by applying 150 nm of anti-reflective coating $MgF_2$ and varying the thickness from 40 to 5 nm thick of $C_{60}$. In order to keep the balance between optical and electrical performance of PSCs, a 10 nm thick of $C_{60}$ is recommended; it can deliver low parasitic absorption in this optical simulation and can compromise the electrical properties. Furthermore, in the NIR wavelength region, the optical loss is mainly affected by both top and bottom ITO, $MoO_x$ layer and, reflected light. After optimizing ITO and $MgF_2$ thickness to 50 and 120 nm, respectively, we obtain 17.07 mA/cm$^2$ of transmission photocurrent through the cells. The transmittance above 800 nm indicates that almost 88 % of implied photocurrent can be utilized for silicon bottom cells.

# 7
# Conclusions and Outlooks

A comprehensive study has been performed to develop the $C_{60}$ transport layer fabricate via the thermal evaporation method and optical analysis of perovskite absorber material. During the study, three main objectives are investigated: (i) develop $C_{60}$ electron transport layers via thermal evaporation to optimize the deposition processes, uniformity, and the effect on optical properties. (ii) Investigate the optical constant of the perovskite absorber layer and transport layer through optical modeling, and (iii) identify the layer's contribution toward the optical loss on inverted pin structure and ST-PSCs for perovskite/silicon tandem devices.
This chapter will summarize the main findings based on the research questions in Section 1.6. Furthermore, based on understanding the whole process and acquired practical experiences, several suggestions are proposed for further investigation.

## 7.1 Conclusions

### *Optimizing the $C_{60}$ ETL film quality fabricated via thermal evaporation method*

The processing recipe has successfully been established to get a reproducible homogenous film by a thermal evaporation method. In addition to that, this project has successfully investigated some deposition parameters that can contribute to the resulted thin-film quality, including the deposition rate and layer thickness. By varying the deposition rate and thickness, the quality of each film was examined by means of layer crystallinity, surface and thickness uniformity, as well as optical properties. The resulting SEM morphology analysis and surface roughness analysis indicate that 40 nm thickness with 0.3 Å/s of deposition rate represents the best characteristic with a smooth surface (RMS 1.33 nm), pinhole-free, and uniform morphology. From the XRD observation, it is found that the diffraction peaks and miller indices of the $C_{60}$ thin-film are associated with the FCC crystal structure. The XRD pattern of $C_{60}$ for all deposition rates and thicknesses shows that the strongest peak is indicated by the (111) plane. This strong peak is caused by the shorter $C_{60}$-$C_{60}$ distance in the (111) plane, i.e., closed packed in FCC, allowing stronger van der Waals interactions and a greater growth rate in (111) orientation. Increasing the deposition rate to 1 Å/s induces a planar defect on the crystal structure due to particle aggregation and non-uniform morphology. Moreover, 20 nm thick $C_{60}$ shows that peak (220) in the XRD pattern is missing. The missing peak indicates that 20 nm of $C_{60}$ crystal growth might be too thin to accommodate the crystal growth and $C_{60}$-$C_{60}$ interaction in that orientation.

### *Optical constant of transport layer and perovskite absorber material*

Investigation of optical constant for both transport layer and perovskite absorber material has been extensively discussed. This study used spectroscopy ellipsometry and proposed a combined method to measure the optical constant for both layers. The b-spline method, which is a purely mathematic approach, can serve as a stepping stone to more physical models such as Tauc-Lorentz. The combination of two can make sure the result follows the Kramers-Kronig relation. The comparison of our results with the existing literature shows excellent agreement. In addition, the resulting optical properties were validated, demonstrating that the models work very well and are in line with the resulted thickness from profilometry, roughness from AFM, and layer absorbance from UV Vis spectrophotometry.

Taken together, this study suggests that using a combination of b-spline and Tauc-Lorentz model could generate the lowest possible mean-squared error (MSE) for extracting the optical constant of transport layer $C_{60}$ and perovskite $Cs_{0.15}FA_{0.85}PbI_{2.85}Br_{0.15}$.

### *Optical losses and contribution of supporting layers on parasitic absorption of PSCs and ST-PSCs*

Based on the optical GenPro4 simulation, the main optical losses in the p-i-n PSCs and ST-PSCs are identified. In p-i-n structure, the layers on top of perovskite from the illumination side (ITO and $MoO_x$) contribute to the high portion of optical loss. The optimization of ITO and $MoO_x$ thickness suggests that 40 mn thick ITO and 10 nm thick $MoO_x$ are ideal for delivering high implied photocurrent (22.14 mA/cm$^2$). Moreover, the back-reflection from the silver electrode could also contribute to the small amount of extra photocurrent collection in $J_{ph}$ of perovskite solar cells.

Furthermore, the optical losses in semi-transparent perovskite solar cells have also been indicated to exhibit the potential of PSCs as a top cell in perovskite/silicon solar cells. In the wavelength range 300 - 800 nm, the main optical losses are due to light reflection, absorption in the $C_{60}$ layer, as well as a small portion from ITO and $MoO_x$ layers. The loss is reduced by (i) applying 120 nm $MgF_2$ that acts as an anti-reflective coating and (ii) decreasing $C_{60}$ thickness to 10 nm. Moreover, in the NIR wavelength region (800 – 1200 nm), the optical loss is mainly affected by both top and bottom ITO, $MoO_x$ layer and, reflected light. These losses are attributed to the non-zero absorption coefficient of both ITO and $MoO_x$ in the long-wavelength range. After optimizing ITO and $MgF_2$ thickness to 50 and 120 nm, respectively, we managed to get 17.07 mA/cm$^2$ (previously was 15.87 mA/cm$^2$) of implied photocurrent transmitted through the cell, indicating ~ 88 % of photocurrent that can be utilized for silicon bottom cells.

## 7.2 Outlooks

### *$C_{60}$ ETL electrical properties and interface studies*

One of the requirements for a good ETL material is its ability to deliver the charge and extract an electron from absorber material. Thus, understanding the electrical properties of $C_{60}$ thin film is necessary to further justify the selected layer thickness in this study. We tried to measure the conductivity (see Appendix A.2) of the $C_{60}$ by means of dark conductivity measurement. However, due to the low conductivity of $C_{60}$ (less than $10^{-7}$ S/cm$^2$) combined with the limitation of the measurement setup, we were unable to get a reliable conductivity value at room temperature. It is essential to increase the thickness, measure in a vacuum condition, and increase temperature annealing to above 200 $^o$C for getting a clear indication of how the temperature can affect the stability of the fcc and hcp phase and its relation toward the conductivity [129]. Another approach to obtain the electrical properties of $C_{60}$ is by using time-resolved microwave conductivity (TRMC). This measurement, however, is not performed due to time constraints. The TRMC working principle is based on the interaction between photoexcited charge carriers and microwave electric fields [130]. TRMC can be used to measure the charge carrier mobility and carrier lifetime of perovskite/$C_{60}$. Since the interface can play an important role in the charge collection pathway, the presence of “defect” at the interface can impede the charge carrier transport and induce the recombination, which further limits the performance of PSCs. Furthermore, to improve the quality of the $C_{60}$ interface, it is also important to reduce the nonradiative recombination at the $C_{60}$/metal contact interface by adding for instance, a bathocuproine (BCP) layer. BCP is a wide-bandgap material and has a high electron affinity. By embedding the BCP layer in PSCs, prohibits the exciton diffusion process towards the metal contact (exciton-blocking barrier) and establishes an ohmic contact between the $C_{60}$ film and electrode [131].

### *Alternative HTL material*

Investigation of optical constant from $MoO_x$ indicates that there is still small absorption of $MoO_x$ in the long-wavelength region. It can be seen from the n and k data attached in Appendix A.4. This non-zero extinction coefficient contributes to the parasitic absorption, particularly in the NIR wavelength range (as indicated in Figure 6.8). It is also reported by Kahn et al. that using $MoO_3$ as an HTL can lead to even more pronounced band bending in the $MAPbI_3$ film and showed that chemical reaction ($MoO_3 \rightarrow MoO_2$) occurred when $MoO_3$ directly contacts with perovskite, which further leads to an increase in interface recombination [132], [133]. A study by Wang et al. reported that $MoO_3$ alone could not be used as an effective HTL for PSCs; it needs an interface modification by inserting organic layers such as NPB and VNPB [133]. Thus, a study on alternative HTL material is also needed. One of the alternatives, such as $NiO_x$, could also be fabricated in many different methods has been widely used to improve the performance of solar cells [133]. It has high transparency in the visible range, superior chemical stability, and easy fabrication methods. Kahn et al. also investigate the electronic properties of between $NiO_x$/perovskite interface. The alignment between the valence band of $NiO_x$ and the valence band of $MAPbI_3$ provides barrier-free hole extraction, a high electron blocking barrier (1.2 eV), and only a small loss in hole potential energy. Thus such interfaces make $NiO_x$ a good electron blocker for the perovskite and eliminate the detrimental electron transport and recombination at the interface [134]. Solution-based and sputtering methods are usually employed to fabricate the NiOx layer. However, we also need to consider that the post-deposition requires high-temperature annealing to tune the work function of NiOx as such promotes an alignment with the work function of perovskite. Imran et al. reported that 300$^{o}$C of annealing temperature is needed to obtain the high PSCs efficiency (15.5%) in inverted p-i-n structure [135]. Nevertheless, the NiOx layer can also be fabricated via atomic layer deposition.

### *Composition for $Cs_xFA_{1-x}Pb(I_{1-x}Br_x)_3$ for a wide bandgap and stable perovskite (application in perovskite/silicon tandem devices)*

Wide bandgap and stable perovskites are needed for the top cell in perovskite/silicon tandem devices. According to the literature, the ideal value of the top cell is ~1.75 eV [122]. This value allows a definite wavelength to pass through perovskite and be absorbed by silicon underneath [122]. One way to further achieve the wide bandgap is by tuning the iodide (I) and bromide (Br) ratio in $Cs_xFA_{1-x}Pb(I_{1-x}Br_x)_3$ perovskite [106]. Moreover, it is also explained previously in Chapter 2 that adding cesium (Cs) could reduce the Br required to achieve a wide bandgap and leads to greater photostability. Thus, it is important to adjust the stochiometry by varying the composition of Cs and Br to get not only stability but also desired bandgap, particularly for top cells in perovskite/silicon tandem devices application. Manzoor et al. reported that by changing the Cs and Br composition from Cs17/Br17 to Cs25/Br20 in $Cs_xFA_{1-x}Pb(I_{1-x}Br_x)_3$ perovskite, they managed to increase the bandgap value from 1.62 to 1.67 eV, respectively [109]. Moreover, Tejada et al. suggested that x = 0.33 in $FA_{0.83}Cs_{0.17}Pb(I_xBr_x)_3$ perovskite could yield the ideal bandgap of 1.75 eV [43].

# Acknowledgments

This chapter is devoted to those who have supported my study at TU Delft and my master thesis.
Firstly, I want to express my sincere and deep appreciation toward the whole photovoltaic materials and devices (PVMD) group and optoelectronic material (OM) group, which gave me the chance to conduct my master thesis project in the best research groups in the TU Delft, particularly in the field of solar energy research and perovskite solar cells. The opportunity to work with various students in a multidisciplinary background and do my lab work in different research lab environments with cutting-edge facilities was a fascinating and unforgettable memory. These experiences have led me to improve my ability to work collaboratively, systematically, and open-mindedly.

I would also especially thank the Indonesia Endowment Fund for Education (LPDP RI), which has fully funded my master's study and approved my request to extend my study for another three months. I hope I can contribute my knowledge to the development of my beloved country Indonesia.

Next, I would like to express my gratitude to all my supervisors. First, I want to thank Dr. Amarante Bottger for understanding my situation and always being supportive, providing a recommendation to extend my study, and providing some valuable input on my thesis project and report. My sincere gratitude also to Dr. Tom Savenije and Prof. dr. Olindo Isabella for their precious suggestions, inspirational ideas, and fundamental questions during my progress report presentation. It has motivated me to keep learning and always be curious.
A special thanks goes to my daily supervisor Dr. Luana Mazzarella, especially for her support, time, patience, as well as precious scientific discussions. She always helped me to find the right solution for the problems that I encountered during this project. Therefore, without her help, this thesis could not be completed. She has inspired me a lot, and I am grateful to have her as my daily supervisor.

Jin Yan and Jasmeen Nespoli deserve special thanks for providing the perovskite samples used for this thesis's optical characterization. I enjoy having fruitful discussions with them and mutual support for each other, particularly when we have difficulties during the project.

I also would like to thank Martijn Tijssen and Yifeng Zhao for their support and help with mask design, fabrication, and metal contact deposition. Moreover, Ruud Hendrikx at the Department of Materials Science and Engineering of the Delft University of Technology is acknowledged for his help on X-ray measurement and useful discussions.

In my personal life, many people have supported me throughout the year. The 2-years of studying abroad has been very challenging for me, especially with the COVID-19 pandemic. However, I manage to survive due to my parents and family's endless love and support in Indonesia. Also, I would like to express my gratitude to my fellow housemates Andrian, Hanif, and Om Roy for accompanying me on this adventure. Thank you for being my second family here in Delft with all the silly jokes and stress-relieved conversations. Also, my thanks goes to Xinrui Zhang, who had helped me with the Matlab code and some inputs on my reports as well as supported me when I was stressed and tired.

Last but not least, I hope that this thesis could contribute academically, specifically to our group, and open new research lines in the perovskite and transport layer field.

# Bibliography


[1] R. Perez and M. Perez, “A Fundamental Look At Supply Side Energy Reser ves For The Planet,” *Int. Energy Agency SHC Program. Sol. Updat.*, vol. 50, no. April 2009, pp. 2–3, 2009.

[2] IEA, “World Energy Outlook 2019,” 2019. [Online]. Available: https://www.iea.org/reports/world-energy-outlook-2019.

[3] J. G. J. Olivier and J. A. H. W. Peters, “TRENDS IN GLOBAL CO2 AND TOTAL GREENHOUSE GAS: 2020 Report,” 2020.

[4] UNFCCC, “The Paris Agreement,” 2016. https://unfccc.int/process-and-meetings/the-paris-agreement/the-paris-agreement (accessed Sep. 26, 2021).

[5] REN21, *Renewables 2019: Global Status Report 2019*. 2019.

[6] International Renewable Energy Agency - IRENA, *Future of solar photovoltaic:Deployment, investment, technology, grid integration and socio-economic aspects*. 2019.

[7] NREL, “NREL Efficiency Chart.” [Online]. Available: https://www.nrel.gov/pv/cell-efficiency.html.

[8] J. F. Geisz *et al.*, “Six-junction III–V solar cells with 47.1% conversion efficiency under 143 Suns concentration,” *Nat. Energy*, vol. 5, no. 4, pp. 326–335, 2020, doi: 10.1038/s41560-020-0598-5.

[9] T. Takamoto, H. Washio, and H. Huso, “Application of InGaP / GaAs / InGaAs Triple Junction Solar cells to :,” *Proc. 40 th IEEE PVSC*, pp. 5–9, 2014.

[10] W. C. Sinke, A. Polman, M. W. Knight, E. C. Garnett, and B. Ehrler, “Photovoltaic materials: present efficiencies and future challenges: LK - https://tudelft.on.worldcat.org/oclc/1105643148.” Petten: ECN, 2016, [Online]. Available: http://resolver.tudelft.nl/uuid:6319b8c4-64d2-4803-b8df-d9f2a3955a4e.

[11] K. Jäger, L. Korte, B. Rech, and S. Albrecht, “Numerical optical optimization of monolithic planar perovskite-silicon tandem solar cells with regular and inverted device architectures,” *Opt. Express*, vol. 25, no. 12, p. A473, 2017, doi: 10.1364/oe.25.00a473.

[12] M. H. Futscher and B. Ehrler, “Efficiency Limit of Perovskite/Si Tandem Solar Cells,” *ACS Energy Lett.*, vol. 1, no. 4, pp. 863–868, 2016, doi: 10.1021/acsenergylett.6b00405.

[13] P. Roy, N. Kumar Sinha, S. Tiwari, and A. Khare, “A review on perovskite solar cells: Evolution of architecture, fabrication techniques, commercialization issues and status,” *Sol. Energy*, vol. 198, no. January, pp. 665–688, 2020, doi: 10.1016/j.solener.2020.01.080.

[14] A. Kojima, K. Teshima, Y. Shirai, and T. Miyasaka, “Organometal halide perovskites as visible-light sensitizers for photovoltaic cells,” *J. Am. Chem. Soc.*, vol. 131, no. 17, pp. 6050–6051, 2009, doi: 10.1021/ja809598r.

[15] P. Roy, N. Kumar Sinha, S. Tiwari, and A. Khare, “A review on perovskite solar cells: Evolution of architecture, fabrication techniques, commercialization issues and status,” *Sol. Energy*, vol. 198, no. December 2019, pp. 665–688, 2020, doi: 10.1016/j.solener.2020.01.080.

[16] A. Miyata *et al.*, “Direct measurement of the exciton binding energy and effective masses for charge carriers in organic–inorganic tri-halide perovskites,” *Nat. Phys.*, vol. 11, no. 7, pp. 582–587, 2015, doi: 10.1038/nphys3357.

[17] G. Grancini *et al.*, “One-Year stable perovskite solar cells by 2D/3D interface engineering,” *Nat. Commun.*, vol. 8, pp. 1–8, 2017, doi: 10.1038/ncomms15684.

[18] S. Mazumdar, Y. Zhao, and X. Zhang, “Stability of Perovskite Solar Cells: Degradation Mechanisms and Remedies,” *Front. Electron.*, vol. 2, no. August, pp. 1–34, 2021, doi: 10.3389/felec.2021.712785.

[19] G. Xing *et al.*, “Long-range balanced electron- and hole-transport lengths in organic-inorganic CH3NH3PbI3.,” *Sci. (New York, N.Y.) TA - TT* -, vol. 342, no. 6156, pp. 344–347, 2013, doi: 10.1126/science.1243167 LK - https://tudelft.on.worldcat.org/oclc/5534259331.

[20] V. Manjunath, R. Krishna, S. Maniarasu, E. Ramasamy, S. Shanmugasundaram, and G. Veerappan, “Chapter 4 - Perovskite Solar Cell Architectures,” in *Perovskite Photovoltaics*, S. Thomas and A. Thankappan, Eds. Academic Press, 2018, pp. 89–121.

[21] S. C. Watthage, Z. Song, A. B. Phillips, and M. J. Heben, “Chapter 3 - Evolution of Perovskite Solar Cells,” in *Perovskite Photovoltaics*, S. Thomas and A. Thankappan, Eds. Academic Press, 2018, pp. 43–88.

[22] N. G. Park, M. Gratzel, and T. Miyasaka, *Organic-Inorganic Halide Perovskite Photovoltaics: From Fundamental to Device Architecture*. 2016.

[23] Z. Zhao *et al.*, “Inverted planar perovskite solar cells with e ffi cient and stability via optimized cathode-interfacial layer,” *Sol. Energy*, vol. 207, no. July, pp. 1165–1171, 2020, doi: 10.1016/j.solener.2020.07.050.
[24] “Perovskite and Perovskite Solar Cells: An Introduction,” *ossila.com*. https://www.ossila.com/pages/perovskites-and-perovskite-solar-cells-an-introduction (accessed Sep. 26, 2021).
[25] B. Gopal Krishna, G. S. Rathore, N. Shukla, and S. Tiwari, *Perovskite solar cells: A review of architecture, processing methods, and future prospects*. Elsevier Ltd., 2021.
[26] L. Calió, S. Kazim, M. Grätzel, and S. Ahmad, “Hole-Transport Materials for Perovskite Solar Cells,” *Angew. Chemie - Int. Ed.*, vol. 55, no. 47, pp. 14522–14545, 2016, doi: 10.1002/anie.201601757.
[27] X. Yin, Z. Song, Z. Li, and W. Tang, “Toward ideal hole transport materials: a review on recent progress in dopant-free hole transport materials for fabricating efficient and stable perovskite solar cells,” *Energy {\&} Environ. Sci.*, vol. 13, no. 11, pp. 4057–4086, 2020, doi: 10.1039/d0ee02337j.
[28] H. Yoon, S. M. Kang, J. K. Lee, and M. Choi, “Hysteresis-free low-temperature-processed planar perovskite solar cells with 19.1% efficiency,” *Energy Environ. Sci.*, vol. 9, no. 7, pp. 2262–2266, 2016, doi: 10.1039/c6ee01037g.
[29] H. W. Kroto, J. R. Heath, S. C. O’Brien, R. F. Curl, and R. E. Smalley, “C60: Buckminsterfullerene,” *Nature*, vol. 318, no. 6042, pp. 162–163, 1985, doi: 10.1038/318162a0.
[30] T. E. Saraswati, U. H. Setiawan, M. R. Ihsan, I. Isnaeni, and Y. Herbani, “The Study of the Optical Properties of C60 Fullerene in Different Organic Solvents,” *Open Chem.*, vol. 17, no. 1, pp. 1198–1212, 2019, doi: 10.1515/chem-2019-0117.
[31] X. L. Yang, J. X. Deng, T. Li, Y. Qin, and L. Kong, “Preparation of C60 thin film and investigation of its optical properties,” *Adv. Mater. Res.*, vol. 194–196, no. 100, pp. 2317–2321, 2011, doi: 10.4028/www.scientific.net/AMR.194-196.2317.
[32] T. Golubev, D. Liu, R. Lunt, and P. Duxbury, “Understanding the impact of C60 at the interface of perovskite solar cells via drift-diffusion modeling,” *AIP Adv.*, vol. 9, no. 3, 2019, doi: 10.1063/1.5068690.
[33] L. Fagiolari and F. Bella, “Carbon-based materials for stable, cheaper and large-scale processable perovskite solar cells,” *Energy Environ. Sci.*, vol. 12, no. 12, pp. 3437–3472, 2019, doi: 10.1039/c9ee02115a.
[34] X. Liu *et al.*, “Novel efficient C60-based inverted perovskite solar cells with negligible hysteresis,” *Electrochim. Acta*, vol. 288, pp. 115–125, 2018, doi: 10.1016/j.electacta.2018.09.004.
[35] K. M. Lee *et al.*, “Thickness effects of thermally evaporated C60 thin films on regular-type CH3NH3PbI3 based solar cells,” *Sol. Energy Mater. Sol. Cells*, vol. 164, no. February, pp. 13–18, 2017, doi: 10.1016/j.solmat.2017.02.003.
[36] T. Kim, J. Lim, and S. Song, “Recent progress and challenges of electron transport layers in organic⇓inorganic perovskite solar cells,” *Energies*, vol. 13, no. 21, pp. 1–16, 2020, doi: 10.3390/en13215572.
[37] W. E. I. Sha, X. Ren, L. Chen, and W. C. H. Choy, “The efficiency limit of CH3NH3PbI3 perovskite solar cells,” *Appl. Phys. Lett.*, vol. 106, no. 22, 2015, doi: 10.1063/1.4922150.
[38] C. G. Bailey, G. M. Piana, and P. G. Lagoudakis, “High-Energy Optical Transitions and Optical Constants of,” 2019, doi: 10.1021/acs.jpcc.9b08903.
[39] S. Albrecht *et al.*, “Environmental Science tandem solar cells processed at low temperature †,” pp. 81–88, 2016, doi: 10.1039/c5ee02965a.
[40] P. Löper *et al.*, “Complex refractive index spectra of CH3NH3PbI3 perovskite thin films determined by spectroscopic ellipsometry and spectrophotometry,” *J. Phys. Chem. Lett.*, vol. 6, no. 1, pp. 66–71, 2015, doi: 10.1021/jz502471h.
[41] H. Li *et al.*, “A review of characterization of perovskite film in solar cells by spectroscopic ellipsometry,” *Sol. Energy*, vol. 212, no. December, pp. 48–61, 2020, doi: 10.1016/j.solener.2020.10.066.
[42] J. A. Guerra *et al.*, “Determination of the complex refractive index and optical bandgap of CH3NH3PbI3 thin films,” *J. Appl. Phys.*, vol. 173104, no. May 2017, 2018, doi: 10.1063/1.4982894.
[43] A. Tejada, S. Braunger, L. Korte, S. Albrecht, B. Rech, and J. A. Guerra, “Optical characterization and bandgap engineering of flat and wrinkle-textured FA0.83Cs0.17Pb(I1-xBrx)3 perovskite thin films,” *J. Appl. Phys.*, vol. 123, no. 17, pp. 0–7, 2018, doi: 10.1063/1.5025728.

[44] D. B. Mitzi, K. Chondroudis, and C. R. Kagan, “Organic-inorganic electronics,” *IBM J. Res. Dev.*, vol. 45, no. 1, pp. 29–45, 2001, doi: 10.1147/rd.451.0029.
[45] H. S. Kim, S. H. Im, and N. G. Park, “Organolead halide perovskite: New horizons in solar cell research,” *J. Phys. Chem. C*, vol. 118, no. 11, pp. 5615–5625, 2014, doi: 10.1021/jp409025w.
[46] M. Anaya, G. Lozano, M. E. Calvo, and H. Míguez, “ABX3 Perovskites for Tandem Solar Cells,” *Joule*, vol. 1, no. 4, pp. 769–793, 2017, doi: 10.1016/j.joule.2017.09.017.
[47] C. Li, X. Lu, W. Ding, L. Feng, Y. Gao, and Z. Guo, “Formability of ABX3 (X= F, Cl, Br, I) halide perovskites,” *Acta Crystallogr. Sect. B*, vol. 64, no. 6, pp. 702–707, Dec. 2008, doi: 10.1107/S0108768108032734.
[48] D. B. Mitzi, M. T. Prikas, and K. Chondroudis, “Thin film deposition of organic-inorganic hybrid materials using a single source thermal ablation technique,” *Chem. Mater.*, vol. 11, no. 3, pp. 542–544, 1999, doi: 10.1021/cm9811139.
[49] C. Li, K. C. K. Soh, and P. Wu, “Formability of ABO3 perovskites,” *J. Alloys Compd.*, vol. 372, no. 1, pp. 40–48, 2004, doi: https://doi.org/10.1016/j.jallcom.2003.10.017.
[50] G. E. Eperon, S. D. Stranks, C. Menelaou, M. B. Johnston, L. M. Herz, and H. J. Snaith, “Formamidinium lead trihalide: A broadly tunable perovskite for efficient planar heterojunction solar cells,” *Energy Environ. Sci.*, vol. 7, no. 3, pp. 982–988, 2014, doi: 10.1039/c3ee43822h.
[51] Y. Xue *et al.*, “Localized incorporation of cesium ions to improve formamidinium lead iodide layers in perovskite solar cells,” *RSC Adv.*, vol. 8, no. 45, pp. 25645–25652, 2018, doi: 10.1039/c8ra04742a.
[52] N. Phung and A. Abate, “The Impact of Nano- and Microstructure on the Stability of Perovskite Solar Cells,” *Small*, vol. 14, no. 46, pp. 1–11, 2018, doi: 10.1002/smll.201802573.
[53] A. Smets, K. Jäger, O. Isabella, R. van Swaaij, and M. Zeman, *Solar Energy : The physics and engineering of photovoltaic conversion, technologies and systems*. Cambridge, UNITED KINGDOM: UIT Cambridge Ltd., 2016.
[54] Y. Tamai, H. Ohkita, H. Benten, and S. Ito, “Exciton Diffusion in Conjugated Polymers: From Fundamental Understanding to Improvement in Photovoltaic Conversion Efficiency,” *J. Phys. Chem. Lett.*, vol. 6, no. 17, pp. 3417–3428, 2015, doi: 10.1021/acs.jpclett.5b01147.
[55] V. D’Innocenzo *et al.*, “Excitons versus free charges in organo-lead tri-halide perovskites,” *Nat. Commun.*, vol. 5, pp. 1–6, 2014, doi: 10.1038/ncomms4586.
[56] S. M. I. Hossain, “Performance and stability of perovskite solar cells,” 2018.
[57] M. Ashby, T. Davies, and S. Gorsse, “The CES EduPack DB for Bulk Functional Materials,” 2015.
[58] S. De Wolf *et al.*, “Organometallic Halide Perovskites: Sharp Optical Absorption Edge and Its Relation to Photovoltaic Performance,” *J. Phys. Chem. Lett.*, vol. 5, no. 6, pp. 1035–1039, Mar. 2014, doi: 10.1021/jz500279b.
[59] X. Ziang *et al.*, “Refractive index and extinction coefficient of CH{_}3NH{_}3PbI{_}3 studied by spectroscopic ellipsometry,” *Opt. Mater. Express*, vol. 5, no. 1, p. 29, 2015, doi: 10.1364/ome.5.000029.
[60] C. Honsberg and S. Bowden, “Photovoltaics Education Website.” 2019, [Online]. Available: https://www.pveducation.org/.
[61] C. Wehrenfennig, G. E. Eperon, M. B. Johnston, H. J. Snaith, and L. M. Herz, “High charge carrier mobilities and lifetimes in organolead trihalide perovskites,” *Adv. Mater.*, vol. 26, no. 10, pp. 1584–1589, 2014, doi: 10.1002/adma.201305172.
[62] T. S. Sherkar, C. Momblona, L. Gil-Escrig, H. J. Bolink, and L. J. A. Koster, “Improving Perovskite Solar Cells: Insights From a Validated Device Model,” *Adv. Energy Mater.*, vol. 7, no. 13, 2017, doi: 10.1002/aenm.201602432.
[63] D. Luo, R. Su, W. Zhang, Q. Gong, and R. Zhu, “Minimizing non-radiative recombination losses in perovskite solar cells,” *Nat. Rev. Mater.*, vol. 5, no. 1, pp. 44–60, 2020, doi: 10.1038/s41578-019-0151-y.
[64] M. B. Johnston and L. M. Herz, “Hybrid Perovskites for Photovoltaics: Charge-Carrier Recombination, Diffusion, and Radiative Efficiencies,” *Acc. Chem. Res.*, vol. 49, no. 1, pp. 146–154, 2016, doi: 10.1021/acs.accounts.5b00411.
[65] L. Contreras-Bernal *et al.*, “Origin and Whereabouts of Recombination in Perovskite Solar Cells,” *J. Phys. Chem. C*, vol. 121, no. 18, pp. 9705–9713, 2017, doi: 10.1021/acs.jpcc.7b01206.
[66] W. Tress, “Perovskite Solar Cells on the Way to Their Radiative Efficiency Limit – Insights Into a Success Story of High Open-Circuit Voltage and Low Recombination,” *Adv. Energy Mater.*, vol. 7, no. 14, 2017, doi: 10.1002/aenm.201602358.
[67] R. Brakkee and R. M. Williams, “Minimizing defect states in lead halide perovskite solar cell

materials," *Appl. Sci.*, vol. 10, no. 9, 2020, doi: 10.3390/app10093061.
[68] S. Nazerdeylami, "Dominant recombination mechanism in perovskite solar cells: A theoretical study," *Sol. Energy*, vol. 206, no. March, pp. 27–34, 2020, doi: 10.1016/j.solener.2020.05.095.
[69] Z. Xiao *et al.*, "Giant switchable photovoltaic effect in organometal trihalide perovskite devices," *Nat. Mater.*, vol. 14, no. 2, pp. 193–197, 2015, doi: 10.1038/nmat4150.
[70] A. Gomez, S. Sanchez, M. Campoy-Quiles, and A. Abate, "Topological distribution of reversible and non-reversible degradation in perovskite solar cells," *Nano Energy*, vol. 45, no. December 2017, pp. 94–100, 2018, doi: 10.1016/j.nanoen.2017.12.040.
[71] H. J. Snaith *et al.*, "Anomalous hysteresis in perovskite solar cells," *J. Phys. Chem. Lett.*, vol. 5, no. 9, pp. 1511–1515, 2014, doi: 10.1021/jz500113x.
[72] Y. Shao, Z. Xiao, C. Bi, Y. Yuan, and J. Huang, "Origin and elimination of photocurrent hysteresis by fullerene passivation in CH3NH3PbI3 planar heterojunction solar cells," *Nat. Commun.*, vol. 5, pp. 1–7, 2014, doi: 10.1038/ncomms6784.
[73] H. Fujiwara, *Spectroscopic Ellipsometry: Principle and Applications*. John Wiley {\&} Sons, Ltd : Chichester, UK, 2007.
[74] H. Fujiwara and R. W. Collins, *Spectroscopic Ellipsometry for Photovoltaics Volume 1: Fundamental Principles and Solar Cell Characterization*, vol. 2. 2018.
[75] J. P. Piel, "Introduction to ellipsometry," *J. Chem. Inf. Model.*, vol. 53, no. 9, pp. 1689–1699, 2013.
[76] D. Datta and S. Kumar, "Growth and ellipsometric studies on C60 thin films for solar cell applications," *J. Appl. Phys.*, vol. 106, no. 7, 2009, doi: 10.1063/1.3239853.
[77] J. W. Weber, T. A. R. Hansen, M. C. M. Van De Sanden, and R. Engeln, "B-spline parametrization of the dielectric function applied to spectroscopic ellipsometry on amorphous carbon," *J. Appl. Phys.*, vol. 106, no. 12, 2009, doi: 10.1063/1.3257237.
[78] H. Scientific, "An Ellipsometric Study of the Optical Constants of C60 & C70 Thin Films," pp. 70–72.
[79] "Tauc-Lorentz Dispersion Formula," pp. 2–4, 1996.
[80] H. Scientific, "What is Cauchy dispersion model?" https://www.horiba.com/en_en/spectroscopic-ellipsometry-cauchy-dispersion-module/.
[81] D. Choi *et al.*, "Thermally-evaporated C 60 / Ag / C 60 multilayer electrodes for semi-transparent perovskite photovoltaics and thin film heaters," *Sci. Technol. Adv. Mater.*, vol. 21, no. 1, pp. 435–449, 2020, doi: 10.1080/14686996.2020.1780472.
[82] "Quartz Crystal Microbalance (QCM)," *nano science instrument*. https://www.nanoscience.com/techniques/quartz-crystal-microbalance/ (accessed Jul. 19, 2021).
[83] myscope.training, "Myscope Microscopy Training." [Online]. Available: https://myscope.training/#.
[84] C. G. Pope, "X-ray diffraction and the bragg equation," *J. Chem. Educ.*, vol. 74, no. 1, pp. 129–131, 1997, doi: 10.1021/ed074p129.
[85] M. Wong-Stringer, "Optimisation of Fabrication Processes for Stable and Scalable Perovskite Solar Cells," *Thesis*, no. September, 2018.
[86] S. A. Phadke, "Exploring the Synthesis and Optoelectronic Properties of Cs 2 AgSb."
[87] R. Santbergen, "Manual for solar cell optical simulation software : GenPro4," no. February, 2016.
[88] R. Santbergen, T. Meguro, T. Suezaki, G. Koizumi, K. Yamamoto, and M. Zeman, "GenPro4 Optical Model for Solar Cell Simulation and Its Application to Multijunction Solar Cells," *IEEE J. Photovoltaics*, vol. 7, no. 3, pp. 919–926, 2017, doi: 10.1109/JPHOTOV.2017.2669640.
[89] L. Eckertová, "Thin Film Thickness and Deposition Rate," *Phys. thin Film.*, 1977.
[90] M. Ohlídal, I. Ohlídal, P. Klapetek, D. Neas, and A. Majumdar, "Measurement of the thickness distribution and optical constants of non-uniform thin films," *Meas. Sci. Technol.*, vol. 22, no. 8, 2011, doi: 10.1088/0957-0233/22/8/085104.
[91] B. Wang *et al.*, "Simulation and optimization of film thickness uniformity in physical vapor deposition," *Coatings*, vol. 8, no. 9, 2018, doi: 10.3390/COATINGS8090325.
[92] H. Zhang *et al.*, "Structural, morphological and optical properties of C60 cluster thin films produced by thermal evaporation under argon gas," *J. Phys. Condens. Matter*, vol. 13, no. 13, pp. 2883–2889, 2001, doi: 10.1088/0953-8984/13/13/303.
[93] A. Huttner, T. Breuer, and G. Witte, "Controlling Interface Morphology and Layer Crystallinity in Organic Heterostructures: Microscopic View on C60 Island Formation on Pentacene Buffer Layers," *ACS Appl. Mater. Interfaces*, vol. 11, no. 38, pp. 35177–35184, 2019, doi: 10.1021/acsami.9b09369.

[94] J. T. Dull *et al.*, “Thermal Properties, Molecular Structure, and Thin-Film Organic Semiconductor Crystallization,” *J. Phys. Chem. C*, vol. 124, no. 49, pp. 27213–27221, 2020, doi: 10.1021/acs.jpcc.0c09408.
[95] T. B. Singh, N. S. Sariciftci, H. Yang, L. Yang, B. Plochberger, and H. Sitter, “Correlation of crystalline and structural properties of C60 thin films grown at various temperature with charge carrier mobility,” *Appl. Phys. Lett.*, vol. 90, no. 21, 2007, doi: 10.1063/1.2743386.
[96] G. Cappuccio and M. L. Terranova, “Thin Film Characterization by Advanced X-ray diffraction techniques,” pp. 331–362, 2018.
[97] R. F. Xiao, W. C. Ho, L. Y. Chow, K. K. Fung, and J. Zheng, “Physical vapor deposition of highly oriented fullerene C60 films on amorphous substrates,” *J. Appl. Phys.*, vol. 77, no. 7, pp. 3572–3574, 1995, doi: 10.1063/1.358592.
[98] E. A. Katz, D. Faiman, S. Shtutina, and A. Isakina, “Deposition and structural characterization of high quality textured C60 thin films,” *Thin Solid Films*, vol. 368, no. 1, pp. 49–54, 2000, doi: 10.1016/S0040-6090(00)00927-5.
[99] S. L. Ren *et al.*, “Ellipsometric determination of the optical constants of C60 (Buckminsterfullerene) films,” *Appl. Phys. Lett.*, vol. 59, no. 21, pp. 2678–2680, 1991, doi: 10.1063/1.105907.
[100] D. Koruga, *Fullerene C60 : history, physics, nanobiology, nanotechnology LK - https://tudelft.on.worldcat.org/oclc/905471026*. Amsterdam SE - XVI, 381 p. : ill. ; 25 cm: Elsevier, 1993.
[101] H. Fujiwara *et al.*, “Determination and interpretation of the optical constants for solar cell materials,” *Appl. Surf. Sci.*, vol. 421, pp. 276–282, 2017, doi: 10.1016/j.apsusc.2016.09.113.
[102] D. J. Borah, A. T. T. Mostako, P. K. Saikia, and P. Dutta, “Effect of thickness and post deposition annealing temperature on the structural and optical properties of thermally evaporated molybdenum oxide films,” *Mater. Sci. Semicond. Process.*, vol. 93, no. November 2018, pp. 111–122, 2019, doi: 10.1016/j.mssp.2018.12.038.
[103] A. A. Akl and S. A. Mahmoud, “Effect of growth temperatures on the surface morphology, optical analysis, dielectric constants, electric susceptibility, Urbach and bandgap energy of sprayed NiO thin films,” *Optik (Stuttg).*, vol. 172, no. April, pp. 783–793, 2018, doi: 10.1016/j.ijleo.2018.07.092.
[104] J. Werner *et al.*, “Complex Refractive Indices of Cesium-Formamidinium-Based Mixed-Halide Perovskites with Optical Band Gaps from 1.5 to 1.8 eV,” *ACS Energy Lett.*, vol. 3, no. 3, pp. 742–747, 2018, doi: 10.1021/acsenergylett.8b00089.
[105] Y. H. Chiang, M. Anaya, and S. D. Stranks, “Multisource Vacuum Deposition of Methylammonium-Free Perovskite Solar Cells,” *ACS Energy Lett.*, vol. 5, no. 8, pp. 2498–2504, 2020, doi: 10.1021/acsenergylett.0c00839.
[106] R. Ji *et al.*, “Thermally evaporated methylammonium-free perovskite solar cells,” *J. Mater. Chem. C*, vol. 8, no. 23, pp. 7725–7733, 2020, doi: 10.1039/d0tc01550d.
[107] L. Q. Xie *et al.*, “Understanding the Cubic Phase Stabilization and Crystallization Kinetics in Mixed Cations and Halides Perovskite Single Crystals,” *J. Am. Chem. Soc.*, vol. 139, no. 9, pp. 3320–3323, 2017, doi: 10.1021/jacs.6b12432.
[108] T. J. Jacobsson *et al.*, “Unreacted PbI2 as a Double-Edged Sword for Enhancing the Performance of Perovskite Solar Cells,” *J. Am. Chem. Soc.*, vol. 138, no. 32, pp. 10331–10343, 2016, doi: 10.1021/jacs.6b06320.
[109] S. Manzoor *et al.*, “Optical modeling of wide-bandgap perovskite and perovskite/silicon tandem solar cells using complex refractive indices for arbitrary-bandgap perovskite absorbers,” *Opt. Express*, vol. 26, no. 21, p. 27441, 2018, doi: 10.1364/oe.26.027441.
[110] B. Subedi *et al.*, “Formamidinium + cesium lead triiodide perovskites: Discrepancies between thin film optical absorption and solar cell efficiency,” *Sol. Energy Mater. Sol. Cells*, vol. 188, no. April, pp. 228–233, 2018, doi: 10.1016/j.solmat.2018.09.002.
[111] M. Shirayama *et al.*, “Degradation mechanism of CH3NH3PbI3 perovskite materials upon exposure to humid air,” *J. Appl. Phys.*, vol. 119, no. 11, 2016, doi: 10.1063/1.4943638.
[112] E. Aspnes, “Optical properties of thin films,” *Electron. Opt.*, vol. 89, no. 1, pp. 249–262, 1982, doi: 10.1016/S0925-3467(98)00055-X.
[113] S. Tang, S. Huang, G. J. Wilson, and A. Ho-baillie, “Progress and Opportunities for Cs Incorporated Perovskite Photovoltaics,” *Trends Chem.*, vol. 2, no. 7, pp. 638–653, 2006, doi: 10.1016/j.trechm.2020.04.002.
[114] G. Paggiaro, “Optimizations of high-efficiency silicon heterojunction solar cells for tandem applications.”
[115] P. B. Johnson and R. W. Christy, “Optical Constant of the Nobel Metals,” *Phys. Rev. B*, vol. 6,

no. 12, pp. 4370–4379, 1972.
[116] Y. Wang *et al.*, “Bilayer broadband antireflective coating to achieve planar heterojunction perovskite solar cells with 23.9% efficiency,” *Sci. China Mater.*, vol. 64, no. 4, pp. 789–797, 2021, doi: 10.1007/s40843-020-1478-5.
[117] S. Akhil *et al.*, “Review on perovskite silicon tandem solar cells: Status and prospects 2T, 3T and 4T for real world conditions,” *Mater. Des.*, vol. 211, p. 110138, 2021, doi: 10.1016/j.matdes.2021.110138.
[118] A. Bag, R. Radhakrishnan, R. Nekovei, and R. Jeyakumar, “Effect of absorber layer, hole transport layer thicknesses, and its doping density on the performance of perovskite solar cells by device simulation,” *Sol. Energy*, vol. 196, no. December 2019, pp. 177–182, 2020, doi: 10.1016/j.solener.2019.12.014.
[119] N. Fakhri, M. S. Naderi, S. G. Farkoush, S. S. Nahaei, S. N. Park, and S. B. Rhee, “Simulation of perovskite solar cells optimized by the inverse planar method in silvaco: 3d electrical and optical models,” *Energies*, vol. 14, no. 18, 2021, doi: 10.3390/en14185944.
[120] S. Rahmany and L. Etgar, “Semitransparent Perovskite Solar Cells,” *ACS Energy Lett.*, vol. 5, no. 5, pp. 1519–1531, 2020, doi: 10.1021/acsenergylett.0c00417.
[121] D. Yang *et al.*, “28.3%-Efficiency Perovskite/Silicon Tandem Solar Cell By Optimal Transparent Electrode for High Efficient Semitransparent Top Cell,” *Nano Energy*, vol. 84, no. February, p. 105934, 2021, doi: 10.1016/j.nanoen.2021.105934.
[122] M. Mujahid, C. Chen, J. Zhang, C. Li, and Y. Duan, “Recent advances in semitransparent perovskite solar cells,” *InfoMat*, vol. 3, no. 1, pp. 101–124, 2021, doi: 10.1002/inf2.12154.
[123] L. Kavan, L. Steier, and M. Gratzel, “Ultrathin buffer layers of SnO2 by atomic layer deposition: Perfect blocking function and thermal stability,” *J. Phys. Chem. C*, vol. 121, no. 1, pp. 342–350, 2017, doi: 10.1021/acs.jpcc.6b09965.
[124] K. M. Yeom, S. U. Kim, M. Y. Woo, J. H. Noh, and S. H. Im, “Recent Progress in Metal Halide Perovskite-Based Tandem Solar Cells,” *Adv. Mater.*, vol. 32, no. 51, pp. 1–24, 2020, doi: 10.1002/adma.202002228.
[125] D. Zhang *et al.*, “High efficiency 4-terminal perovskite/c-Si tandem cells,” *Sol. Energy Mater. Sol. Cells*, vol. 188, no. March, pp. 1–5, 2018, doi: 10.1016/j.solmat.2018.07.032.
[126] N. N. Lal, Y. Dkhissi, W. Li, Q. Hou, Y. B. Cheng, and U. Bach, “Perovskite Tandem Solar Cells,” *Adv. Energy Mater.*, vol. 7, no. 18, pp. 1–18, 2017, doi: 10.1002/aenm.201602761.
[127] T. Duong *et al.*, “Rubidium Multication Perovskite with Optimized Bandgap for Perovskite-Silicon Tandem with over 26% Efficiency,” *Adv. Energy Mater.*, vol. 7, no. 14, 2017, doi: 10.1002/aenm.201700228.
[128] M. Mazur, R. Pastuszek, D. Wojcieszak, D. Kaczmarek, A. Obstarczyk, and A. Lubanska, “Effect of thickness on optoelectronic properties of ITO thin fi lms,” no. September 2020, 2022, doi: 10.1108/CW-11-2019-0170.
[129] J. Gong, F. Zhang, Y. Li, G. Ma, and G. Chen, “Effects of annealing on the electrical conductivity of C60 films,” *Thin Solid Films*, vol. 261, no. 1–2, pp. 266–270, 1995, doi: 10.1016/S0040-6090(95)06542-3.
[130] V. M. Caselli, Z. Wei, M. M. Ackermans, E. M. Hutter, B. Ehrler, and T. J. Savenije, “Charge Carrier Dynamics upon Sub-bandgap Excitation in Methylammonium Lead Iodide Thin Films: Effects of Urbach Tail, Deep Defects, and Two-Photon Absorption,” *ACS Energy Lett.*, vol. 5, no. 12, pp. 3821–3827, 2020, doi: 10.1021/acsenergylett.0c02067.
[131] M. Vogel, S. Doka, C. Breyer, M. C. Lux-Steiner, and K. Fostiropoulos, “On the function of a bathocuproine buffer layer in organic photovoltaic cells,” *Appl. Phys. Lett.*, vol. 89, no. 16, pp. 1–4, 2006, doi: 10.1063/1.2362624.
[132] P. Schulz *et al.*, “High-work-function molybdenum oxide hole extraction contacts in hybrid organic-inorganic perovskite solar cells,” *ACS Appl. Mater. Interfaces*, vol. 8, no. 46, pp. 31491–31499, 2016, doi: 10.1021/acsami.6b10898.
[133] S. Wang, T. Sakurai, W. Wen, and Y. Qi, “Energy Level Alignment at Interfaces in Metal Halide Perovskite Solar Cells,” *Adv. Mater. Interfaces*, vol. 5, no. 22, 2018, doi: 10.1002/admi.201800260.
[134] P. Schulz, L. L. Whittaker-Brooks, B. A. Macleod, D. C. Olson, Y. L. Loo, and A. Kahn, “Electronic Level Alignment in Inverted Organometal Perovskite Solar Cells,” *Adv. Mater. Interfaces*, vol. 2, no. 7, 2015, doi: 10.1002/admi.201400532.
[135] M. Imran, H. Coskun, N. A. Khan, and J. Ouyang, “Role of annealing temperature of nickel oxide (NiOx) as hole transport layer in work function alignment with perovskite,” *Appl. Phys. A Mater. Sci. Process.*, vol. 127, no. 2, 2021, doi: 10.1007/s00339-021-04283-5.

# Appendix

## A.1 Masks design and fabrication

The masks were designed using L-Edit software v16.3 from Tanner EDA Mentor Graphics. Fabrication was done using a laser cutting process to ensure precision.

*TCO mask* *PVK, ETL, HTL* *Metal electrode mask*

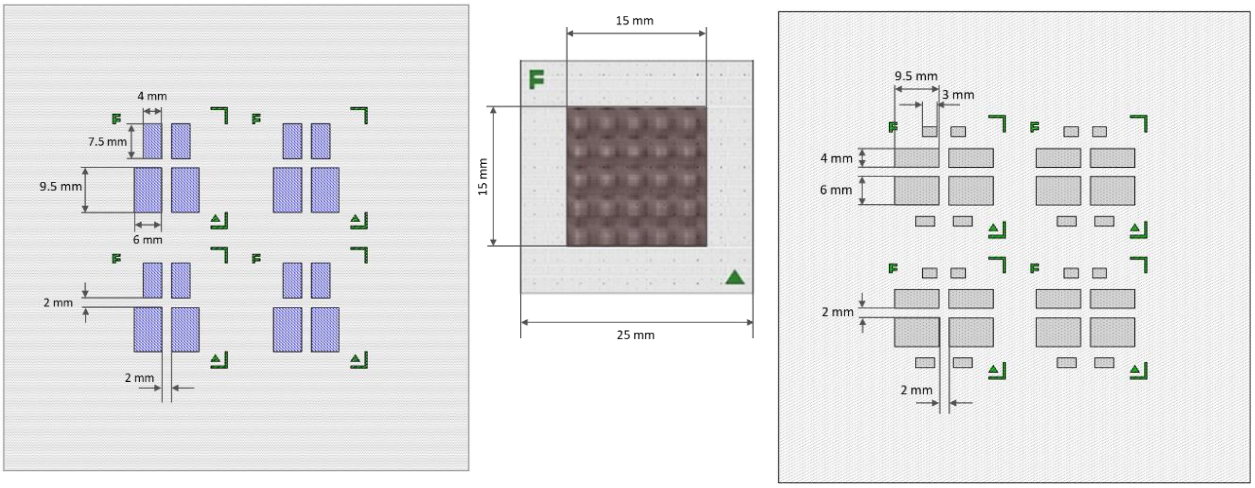


*Figure A. 1 Dimension of the designed masks for a) TCO, b) Perovskite and transport layer, and c) metal contact and frame.*

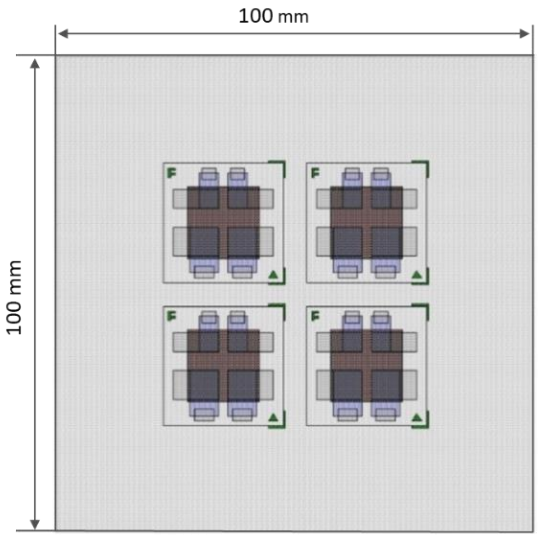


*Figure A. 2 The complete stack of the mask representing the total active area of four substrates*

| | |
|---|---|
| # active area (total) | 16 active areas (4 active areas on each substrate) |
| Active area size | - 4 mm x 4 mm<br>- 6 mm x 6 mm |
| Thickness | 1.1 mm |
| Size (total outline) | 100 mm x 100 mm |
| Substrate capacity | 4 substrates |
| Material | Stainless steel |

## A.2 Conductivity measurement

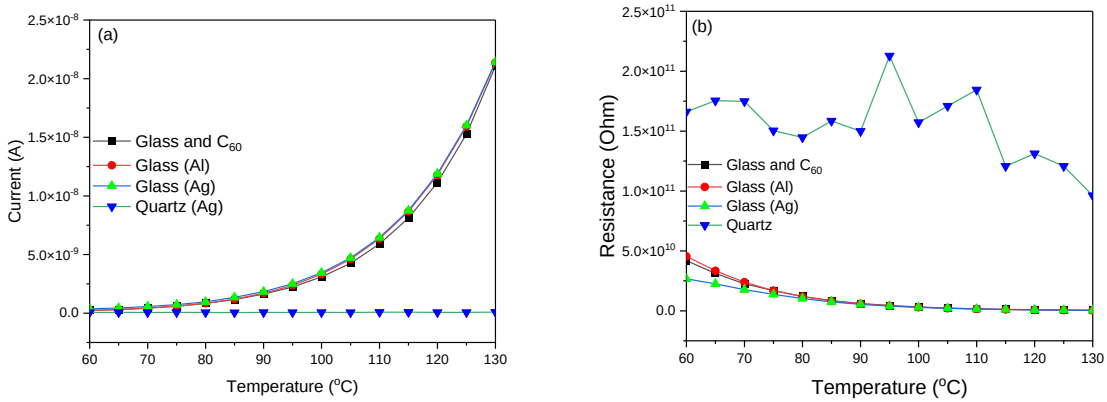


*Figure A. 3 (a) Current flow and (b) resistance with different substrate and metal electrodes at temperature 130 to 60 °C*

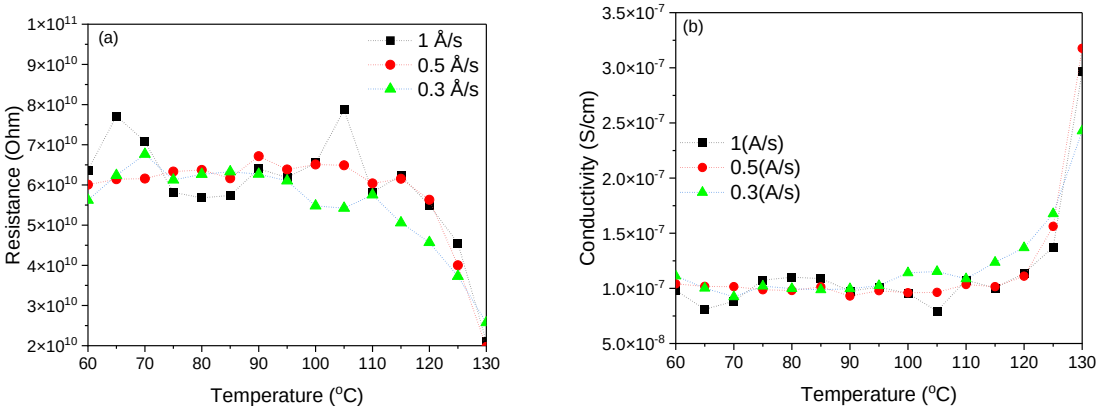


*Figure A. 4 (a) Resistance and b) conductivity of C60 thin film with different temperatures.*

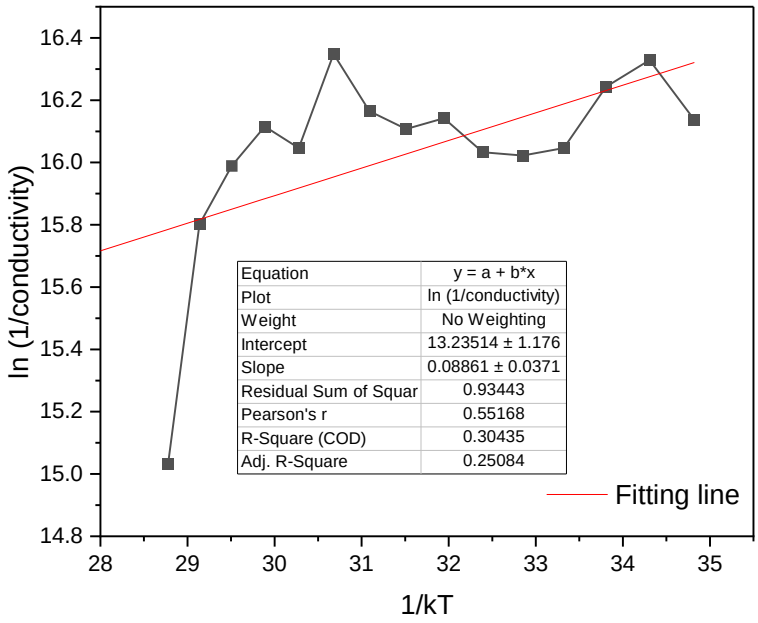


*Figure A. 5 The temperature dependence of the $C_{60}$ film conductivity with 40 nm thickness and 1 Å/s of deposition rate*

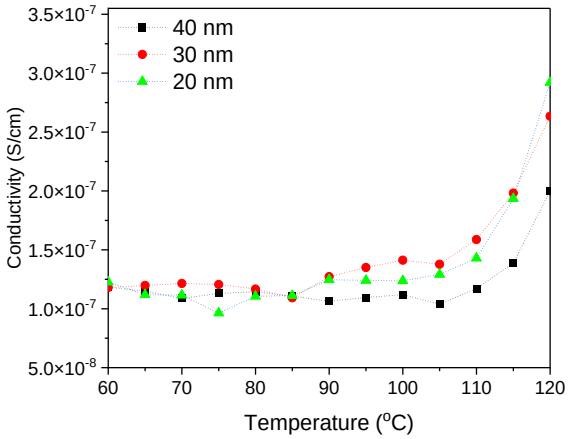


*Figure A. 6 Conductivity of $C_{60}$ thin film with different thickness*

## A.3 Optical loss with different $C_{60}$ thickness and deposition rate

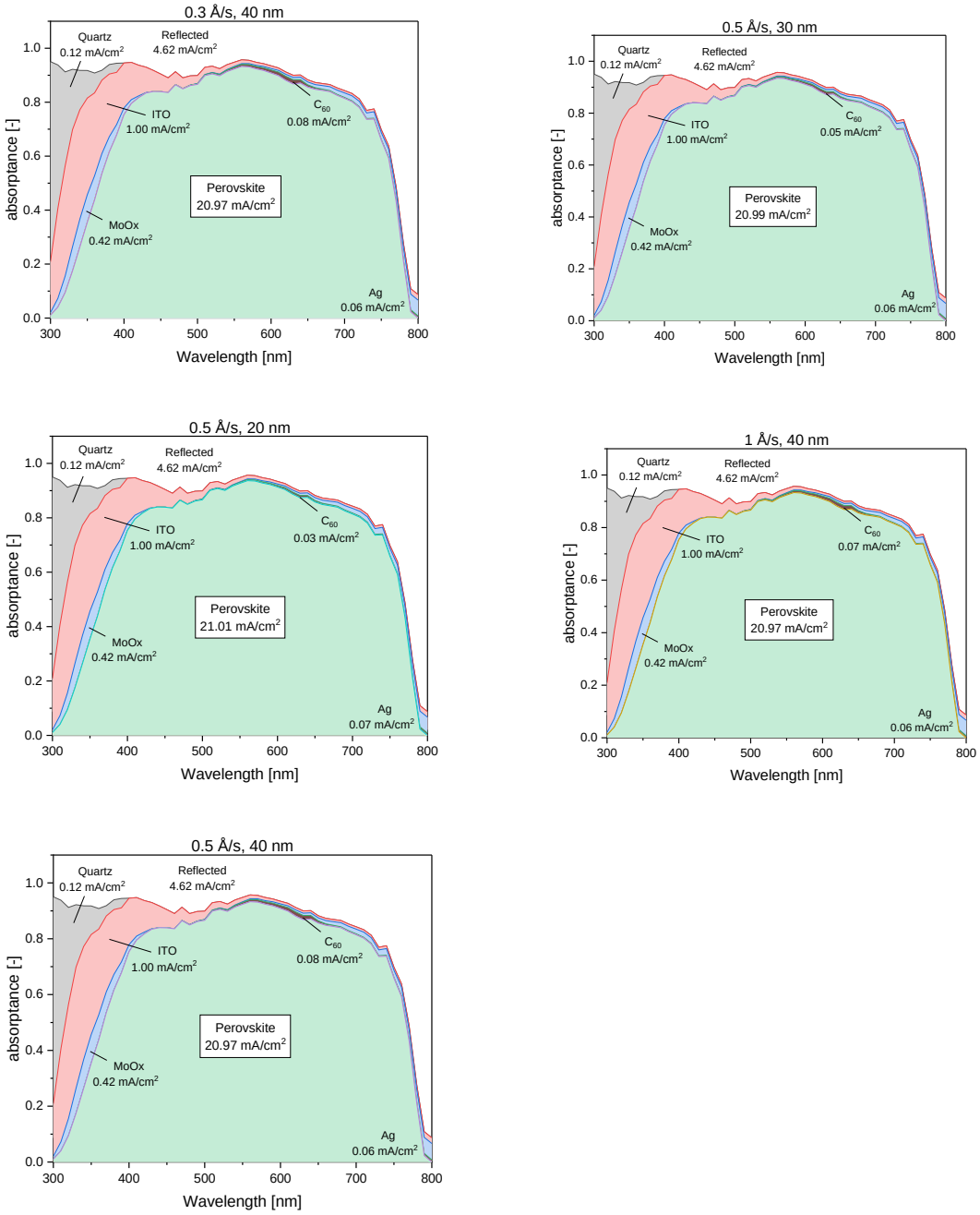


*Figure A. 7 GenPro4 simulation of the perovskite solar cells p-i-n structure with different thickness and deposition rate of $C_{60}$*

## A.4 Optical constant for quartz, ITO and $MoO_x$

### *A.4.1 Quartz substrate*

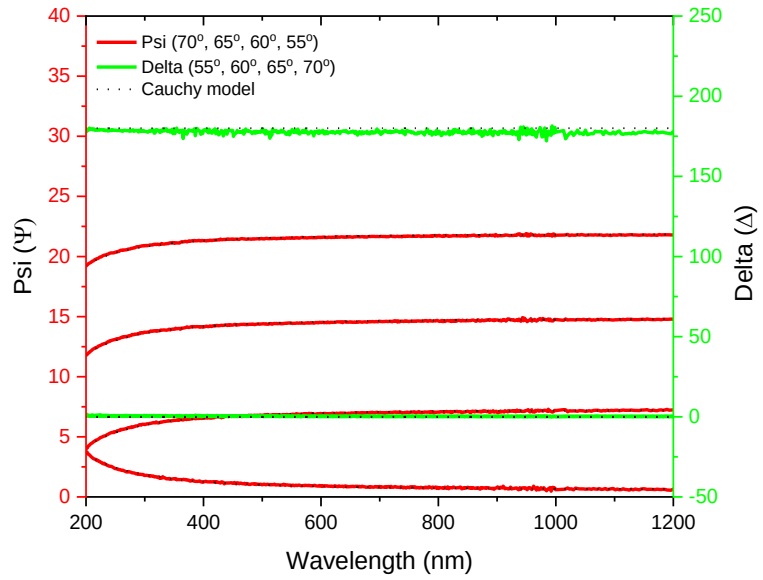


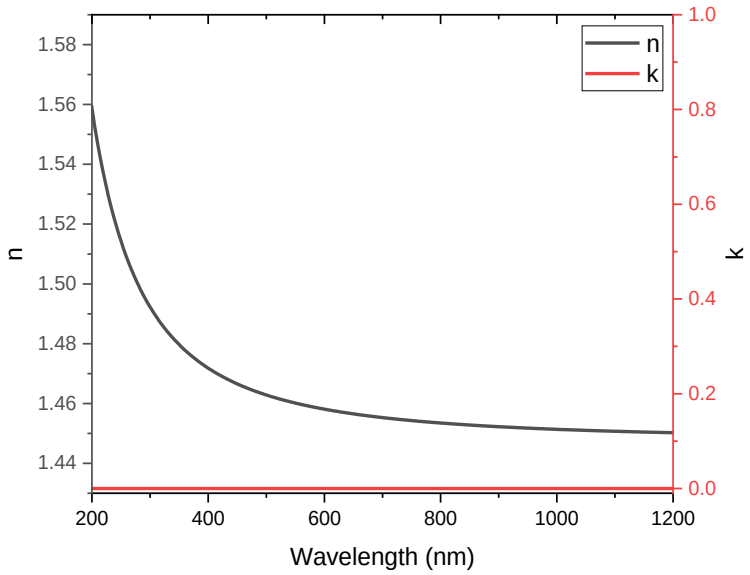

## A.4.2 $MoO_x$

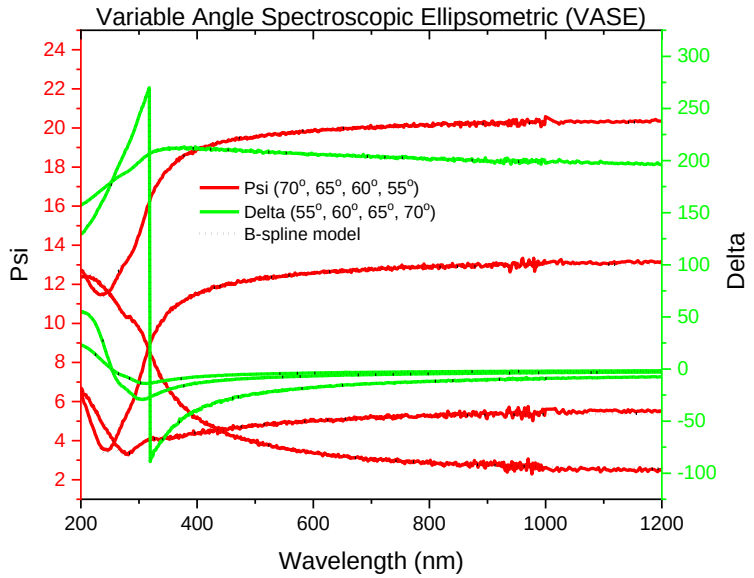


*Figure A. 8 Measured (solid line) and simulated (dashed line) psi and delta of MoOx*

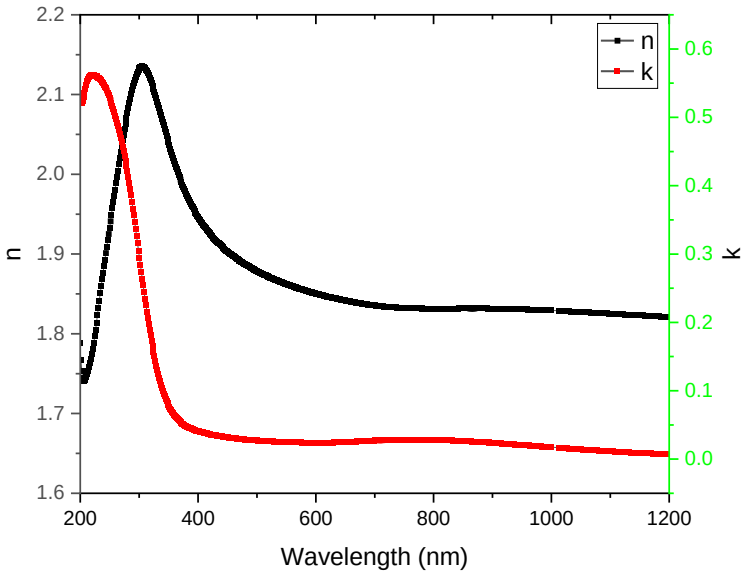


*Figure A. 9 Optical constant of $MoO_x$*

### *A.4.3 ITO*

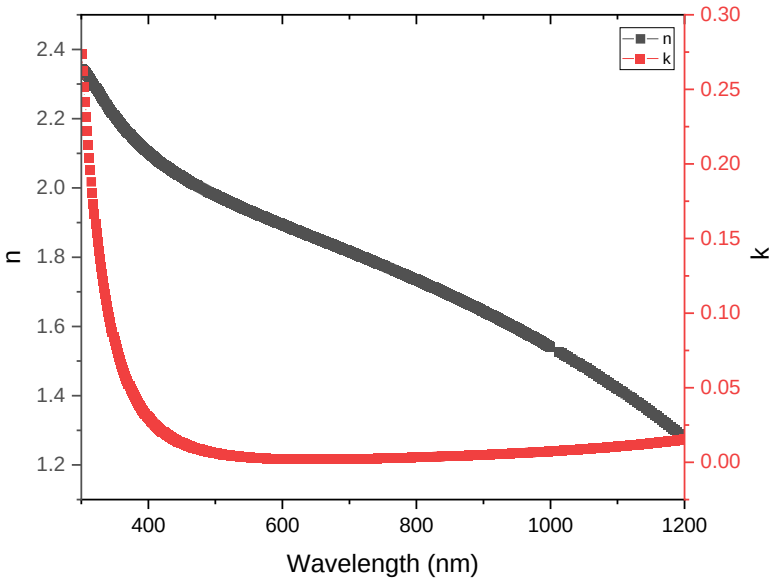


*Figure A. 10 Optical constant of ITO*

## A.5 Optical loss of ST-PSCs simulated via GenPro4 simulation

*Optical loss of ST-PSCs BEFORE optimization of ITO and $MgF_2$ thickness*

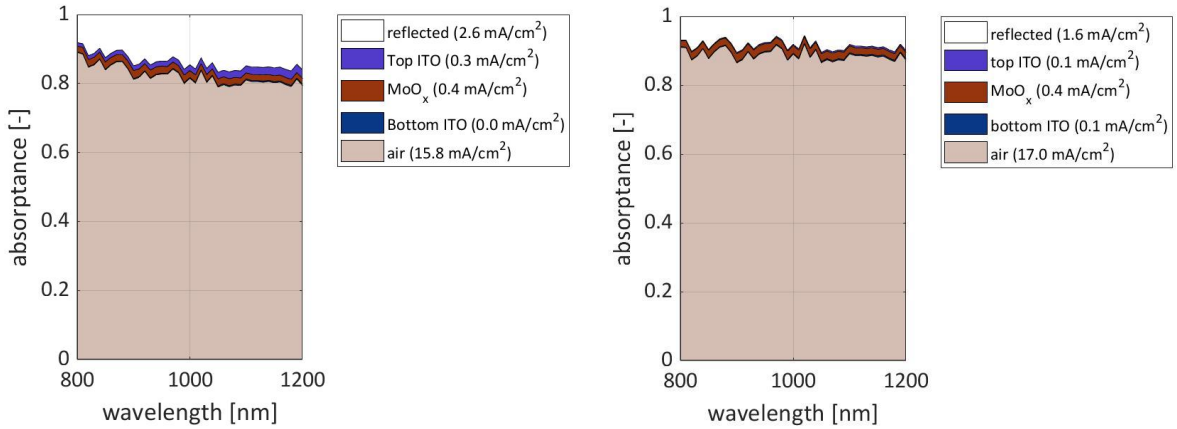


*Figure A. 11 Optical loss of ST-PSCs AFTER optimization of ITO and $MgF_2$ thickness*

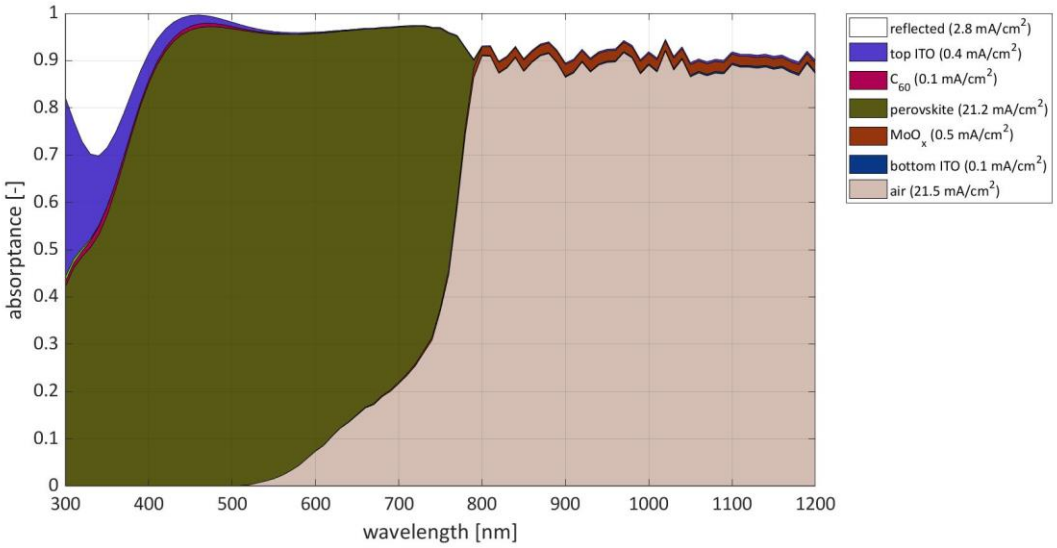


*Figure A. 12 Optical loss of ST-PSCs in the wavelength range 300 – 1200 nm, with ITO and $MgF_2$ thickness optimization*